IEEE Open Journal of the
Industrial Electronics Society

Received 15 November 2023; revised 22 January 2024; accepted 5 February 2024. Date of publication 14 February 2024; date of current version 15 April 2024. The review of this article was arranged by Associate Editor Xing Zhao.

Digital Object Identifier 10.1109/OJIES.2024.3366082

Virtual Synchronous Machine Control for Doubly Fed Induction Machine-Based Wind Energy Conversion Systems

ANDRE THOMMESSEN (Member, IEEE) AND CHRISTOPH MICHAEL HACKL (Senior Member, IEEE)

Laboratory for Mechatronic and Renewable Energy Systems (LMRES), Hochschule München (HM) University of Applied Sciences, 80335 Munich, Germany

CORRESPONDING AUTHOR: CHRISTOPH M. HACKL (e-mail: christoph.hackl@hm.edu)

This work was financially supported by the Munich University of Applied Sciences HM and the Deutsche Forschungsgemeinschaft (DFG, German Research Foundation) under Grant 512819356 and was supported by the Federal Ministry for Economic Affairs and Climate Action of Germany under Grant 03EI6020B.

ABSTRACT Renewable inverter-based resources (IBRs), such as wind energy conversion systems (WSs), replace directly grid-connected synchronous machines (SMs). Standard grid-following (GFL) control of IBRs decreases the power system inertia. This article proposes virtual synchronous machine (VSM)-based grid-forming (GFM) control for doubly fed induction machine (DFIM)-based WSs with the following extensions: feedforward torque control (FTC) for maximum power point tracking (MPPT), MPPT compensation for accurate inertia emulation, reference power point tracking to provide energy reserves, dynamic droop saturation control to mitigate power overloading, and grid voltage control utilizing DFIM stator and rotor-side back-to-back inverter reactive power. The WSs are integrated into the IEEE 9-bus test system. Comprehensive simulation results give insights into (V)SM-based power system dynamics. Compared with existing VSM control without FTC, the proposed FTC increases the wind energy yield, i.e., typical MPPT performance is achieved, similar to GFL control. For high power penetration of IBRs, the proposed VSM control enables stable operation due to its GFM capability, whereas GFL control tends to instability. The VSM provides higher power system damping than a real SM due to adaptable internal damping. If wind power reserves are available, the fast VSM droop control provides additional damping by adapting the virtual turbine power without the dominant delays of real turbine dynamics.

INDEX TERMS Doubly fed induction machine (DFIM), grid-following (GFL), grid-forming (GFM), synchronization stability, power system dynamics, reserves, virtual synchronous machine (VSM), wind energy.

NOMENCLATURE

Applying the Clarke and Park transformation with Park angle ϕ_p to three-phase signal vectors $\boldsymbol{x}^{abc}$ yields (orthogonal) two-phase signal vectors [1, Sec. 14.2.4]

$$\boldsymbol{x}^{\alpha\beta} := \boldsymbol{T}_\mathrm{c}\boldsymbol{x}^{abc}, \quad \boldsymbol{x}^{dq} := \boldsymbol{T}_\mathrm{p}(\phi_\mathrm{p})^{-1}\boldsymbol{x}^{\alpha\beta} = \boldsymbol{T}_\mathrm{p}(-\phi_\mathrm{p})\boldsymbol{x}^{\alpha\beta} \quad (1)$$

with $\boldsymbol{T}_\mathrm{c}$ and $\boldsymbol{T}_\mathrm{p}$, as given in the Nomenclature. Small bold symbols denote vectors, e.g., $\boldsymbol{i}_\mathrm{s}^{dq} := (i_\mathrm{s}^d, i_\mathrm{s}^q)^\top$ is the stator current vector in the dq-reference frame, and capital bold symbols denote either matrices or normalized vectors, e.g., $\boldsymbol{I}_\mathrm{s}^{dq} := (I_\mathrm{s}^d, I_\mathrm{s}^q)^\top := (\frac{i_\mathrm{s}^d}{\widehat{\imath}_\mathrm{s,R}}, \frac{i_\mathrm{s}^q}{\widehat{\imath}_\mathrm{s,R}})^\top$ with rated stator current amplitude $\widehat{\imath}_\mathrm{s,R}$. The function $\arg\max f(x)$ returns the argument $x^\star$, which maximizes the function $f(\cdot)$, i.e., $f(x^\star) = \max f(x)$. For $b > a$, the saturation function is defined as

$$\mathrm{sat}_a^b(x) := \begin{cases} a, & \text{if } x < a, \\ b, & \text{if } x > b, \\ x, & \text{otherwise.} \end{cases} \quad (2)$$

TABLE 1. Definition of symbols (for more details, see Table I–III in [2]).

$\mathbb{N}$, $\mathbb{R}$, $:=$, $^\top$	natural, real numbers, "is defined as," "transposed."
$\boldsymbol{x}$	$:= (x_1, \ldots, x_n)^\top \in \mathbb{R}^n$, column vector with $n \in \mathbb{N}$.
$\boldsymbol{0}_n$	$:= (0, \quad \ldots, \quad 0)^\top \in \mathbb{R}^n$, column vector with zeros.
$\boldsymbol{I}_n$	$:= \mathrm{diag}(1, \ldots, 1) \in \mathbb{R}^{n\times n}$, identity matrix.
$\dot{x}$	$:= \frac{\mathrm{d}}{\mathrm{d}t}x$, time derivative.
$\widehat{\boldsymbol{x}}$	$:= \|\boldsymbol{x}\| := \sqrt{\boldsymbol{x}^\top\boldsymbol{x}}$, amplitude or Euclidean norm.
$\boldsymbol{T}_\mathrm{c}$	$:= \kappa \begin{bmatrix} 1 & -\frac{1}{2} & -\frac{1}{2} \\ 0 & \frac{\sqrt{3}}{2} & -\frac{\sqrt{3}}{2} \end{bmatrix}$, Clarke transformation matrix.
$\kappa \in \left\{\frac{2}{3}, \sqrt{\frac{2}{3}}\right\}$	scaling factor for amplitude or power invariance.
$\boldsymbol{T}_\mathrm{p}(\phi)$	$:= \begin{bmatrix} \cos(\phi) & -\sin(\phi) \\ \sin(\phi) & \cos(\phi) \end{bmatrix}$, Park transformation matrix
$\boldsymbol{J}$	$:= \begin{bmatrix} 0 & -1 \\ 1 & 0 \end{bmatrix} = \boldsymbol{T}_\mathrm{p}(\frac{\pi}{2})$, matrix for rotation by $\frac{\pi}{2}$.

I. INTRODUCTION

Facing the climate crisis, renewable inverter-based resources (IBRs), such as wind energy conversion systems (WSs), replace directly grid-connected synchronous machines (SMs). SMs inherently form the grid voltage and provide power system inertia, whereas standard grid-following (GFL) control of IBRs leads to decreasing inertia of the future power system with low SM generation [3]. At the same time, the installation of additional transmission capacities, such as HVDC systems, leads to potentially higher imbalances between power generation (including import) and power demand (including export) during grid faults [4]. Both, the decreasing power system inertia and the increasing worst-case power imbalance, are major challenges for future grid stability [3], [4].

The current focus of research and development is on grid-forming (GFM) control for IBRs, with GFM referring to the SM-like or voltage-source-like capability to form the grid's voltage amplitude and frequency [5]. In contrast, GFL control refers to the standard current-source-like capability of IBRs to follow the grid frequency, using fast synchronization, e.g., based on a phase-locked loop (PLL) [6] or frequency-locked loop [7], [8], and injecting a (quasi-) constant current or power [9]. For GFL control of renewables, the power reference is usually given by some maximum power point tracking (MPPT) strategy [9]. The GFL control may be extended to provide fast frequency response or "synthetic" inertia, but only GFM control allows for an instantaneous response or "synchronous" inertia emulation similar to SMs [10], [11]. Latter kind of inertia is crucial to limit the initial rate of change of frequency (RoCoF) after a sudden power imbalance, e.g., during system split events [3]. Besides, as also shown in this article, GFM control achieves power oscillation damping, whereas GFL control tends to instability in grids with low SM generation [5]. However, for GFM-controlled inverters, current limitation while ensuring synchronization stability is one of the major challenges [9], [12].

This article considers GFM control for type 3 WSs, which use doubly fed induction machines (DFIMs) with grid-connected stator. The rotor is connected to a back-to-back inverter, which consists of the rotor-side inverter (RSI) and the grid-side inverter (GSI), which share the same dc-link, see Fig. 1. This is a common configuration used worldwide [13]. In [12], different GFM controls for inverters are considered, e.g., droop control, virtual synchronous machine (VSM) control, and matching control. The latter is based on the observation that the dc-link voltage—similar to the SM speed—indicates power imbalances. The unleashed power during the inertial response of matching control depends on the dc-link capacity. However, for the considered DFIM-based WS, the energy stored in the dc-link capacity is negligible in comparison to the kinetic energy reserves of DFIM and wind turbine (WT), see (R.2) and also [14]. Moreover, only a fraction of the DFIM power flows via the dc-link [15]. Thus, matching control is not considered in this article. Anyway, GFM control methods based on ac voltage measurements, such as VSM control, further improve the grid frequency support compared with matching control based on dc-link voltage measurement [12].

The VSM damping in [12] and [16] is a function of the VSM speed only, which is *not* analogous to SMs, since the currents in the SM damper windings depend on the SM slip, and thus, also on the grid frequency. This kind of VSM damping rather corresponds to droop control but without the significant governor time delay introduced by a real SM or, more precisely, by the comparably slow dynamics of a real SM's turbine system including its actuators. Actually, this kind of VSM control reduces to droop control, if the VSM inertia is negligible in comparison to the VSM damping [12]. For clarity, the VSM damping terminology is avoided in this context or replaced by the VSM droop (gain) in the following. The VSM droop dampens the torque response to reference changes during normal operation [16] and provides power system damping during RoCoF events if power reserves are available [17]. However, in addition to the VSM droop, a VSM damping analogous to the SM damper windings is crucial to stay grid-synchronized and to avoid power oscillations during RoCoF events, taking into account that the power reserves for the VSM droop may be limited [18], [19], [20].

The overload capability of IBRs is small in comparison to SMs due to the small thermal time constants of power electronics compared with, e.g., windings of electrical machines. Hence, SMs are capable of providing 3 to 5 times their rated currents during faults, whereas IBRs only allow for an overloading of 1 to 1.5 times their rated currents [9]. However, in addition to the VSM inertial response, the VSM droop may lead to power overloading of IBRs during faults, as also shown in this article. Thus, Du and Lasseter [21] proposed an overload mitigation control but only for inverters and only for pure droop control without VSM. This article proposes a dynamic saturation control of the VSM droop to mitigate power overloading of DFIM-based WSs during RoCoF events.

Despite the research trend toward VSM control for inverters [12] or for type 4 WSs, based on full-scale back-to-back inverters [18], [22], [23], the public research on VSM control for DFIMs or type 3 WSs is limited. There exist a few VSM control methods for DFIMs [16], [20], [24], [25], [26], [27], [28], [29] with similar grid synchronization or outer torque control loops, but their inner electromagnetic DFIM control loops differ as follows:

(i) *no* inner current or magnetic flux control loop [24], [25], [26], i.e., applying the VSM voltage amplitude and angle directly to the RSI;
(ii) inner current control loop [20], [27], [28];
(iii) inner magnetic rotor flux control loop [16];
(iv) outer magnetic stator flux and inner stator current control loop [29].

For instance, the inner magnetic rotor flux control in [16] sets the active power by changing the angle between rotor and

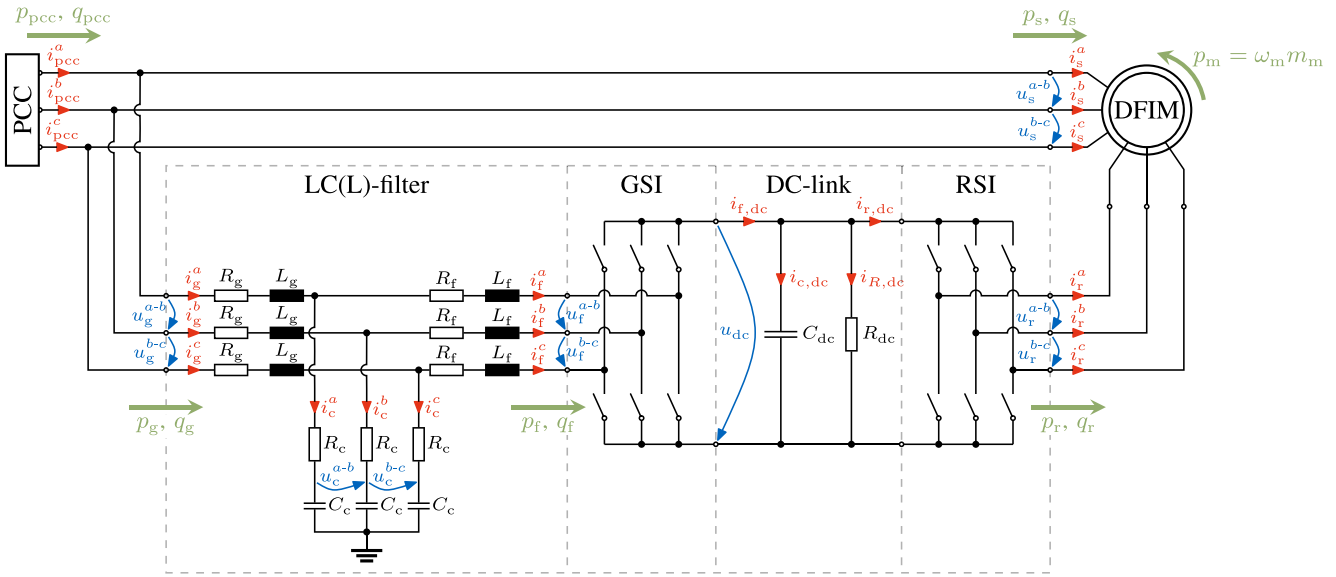

FIGURE 1. **Electrical circuit of the WU with DFIM.**

stator magnetic flux linkages and sets the reactive power by changing the magnetic rotor flux linkage amplitude, whereas this article uses the inner rotor current control with the reference vector angle depending on the VSM rotor position based on [28]. This is motivated by the fact that the excitation or rotor current vector of an SM is inherently fixed to its rotor position as well.

The VSM control leads to decreased performance of MPPT or reference power point tracking (RPPT) for type 3 and type 4 WSs [11], [22], [27]. More precisely, the VSM inertia delays the torque reference tracking. For instance, considering a sudden wind change from below to above rated wind speed, more pitch actuation is required to limit the WT speed due to the delayed DFIM torque response. Thus, the WT may face higher mechanical stress, and, for MPPT, the higher mismatch between wind input power and electrical output power leads to decreased efficiency [27]. Thus, a compromise between grid support and MPPT performance has to be found. Lately, Thommessen and Hackl [28] combined VSM control with feedforward torque control (FTC) for fast MPPT, i.e., they achieved decoupling of the inertial response to RoCoF events and the MPPT during normal operation. However, Thommessen and Hackl [28] only considered ideal RoCoF events, i.e., neglected the interaction with the grid, whereas Tayyebi et al. [12] considered the interactions of (V)SMs but only for VSM-controlled inverters, i.e., not for VSM-controlled DFIMs. Moreover, Thommessen and Hackl [28] only considered MPPT, but also RPPT or wind energy reserves are desirable for grid support [23].

This article summarizes the long version [2] and extends the VSM control with FTC for DFIM-based WSs in [28] by the following contributions:

(i) RPPT based on the maximum rotation strategy [23] to maximize the kinetic energy reserves;
(ii) dynamic droop power saturation to mitigate power overloading;
(iii) improved MPPT compensation for accurate inertia emulation during severe RoCoF events;
(iv) WS modeling, including not only the DFIM with RSI but also the RSI power supply via the dc-link, the GSI, and the *LC*(*L*)-filter;
(v) WS control, including not only the DFIM power control but also the dc-link voltage and grid voltage control;
(vi) simulations, including the grid connection to take interactions with the transmission system or other generation units (GUs) into account, which may lead to power oscillations.

In this regard, it is important to note that both, the DFIM stator and the GSI, may provide reactive power for grid voltage support. Thus, the grid voltage control, proposed in this article, uses this degree of freedom to maximize the VSM or DFIM load angle stability margin, while taking the operating limits (such as current and voltage limits) into account. To the best of the authors' knowledge, there is no publication proposing the combination or considering the interaction of VSM control for DFIMs with FTC, MPPT, RPPT, and droop control as this article. In conclusion, this article proposes modeling and control of DFIM-based WSs and of their interactions with future power systems to pave the way toward 100% renewable power generation. The proposed approach may also be adapted to other types of WSs.

The rest of this article is organized as follows. Section II introduces the modeling of the DFIM-based WS, before Section III proposes its control system. Then, Section IV discusses numerous simulation scenarios and results regarding the WS and the power system performance during normal operation and grid faults. Finally, Section V concludes this

article by summarizing its achievements and by discussing future research foci.

II. MODELING

In this article, a WS consists of several wind units (WUs), connected in parallel at the point of common coupling (PCC), with number of WUs or WS scaling factor n_{wu}. Fig. 1 shows the electrical system of a DFIM-based WU. The DFIM stator, directly connected to the PCC, generates most of the PCC active power $p_{\mathrm{pcc}} = p_{\mathrm{g}} + p_{\mathrm{s}} < 0$. The RSI, connected to the DFIM rotor, and the GSI, connected to the PCC via the $LC(L)$-filter, share a common dc-link voltage u_{dc}. The GSI may provide reactive power in addition to the DFIM stator, i.e., $q_{\mathrm{pcc}} = q_{\mathrm{g}} + q_{\mathrm{s}}$. Note that grid-side filter power p_{g}, GSI-side filter power p_{f}, and rotor power p_{r} may be positive or negative depending on the DFIM's slip (see [15] for a detailed power flow analysis). The PCC currents are the sum of stator and grid-side filter currents, i.e., $\boldsymbol{i}_{\mathrm{pcc}}^{abc} := (i_{\mathrm{pcc}}^{a}, i_{\mathrm{pcc}}^{b}, i_{\mathrm{pcc}}^{c})^{\top} = \boldsymbol{i}_{\mathrm{g}}^{abc} + \boldsymbol{i}_{\mathrm{s}}^{abc}$. The stator and grid-side filter voltages $\boldsymbol{u}_{\mathrm{s}}^{a\text{-}b\text{-}c} = \boldsymbol{u}_{\mathrm{g}}^{a\text{-}b\text{-}c} := (u_{\mathrm{g}}^{a\text{-}b}, u_{\mathrm{g}}^{b\text{-}c}, u_{\mathrm{g}}^{c\text{-}a})^{\top}$ equal the line-to-line PCC voltages. GSI and RSI apply the line-to-line voltages $\boldsymbol{u}_{\mathrm{f}}^{a\text{-}b\text{-}c} := (u_{\mathrm{f}}^{a\text{-}b}, u_{\mathrm{f}}^{b\text{-}c}, u_{\mathrm{f}}^{c\text{-}a})^{\top}$ and $\boldsymbol{u}_{\mathrm{r}}^{a\text{-}b\text{-}c} := (u_{\mathrm{r}}^{a\text{-}b}, u_{\mathrm{r}}^{b\text{-}c}, u_{\mathrm{r}}^{c\text{-}a})^{\top}$ to the $LC(L)$ filter and the DFIM rotor, respectively. The DFIM power $p_{\mathrm{m}} := \omega_{\mathrm{m}} m_{\mathrm{m}}$ depends on WT or DFIM angular velocity ω_{m} and DFIM torque m_{m}.

The following sections discuss the modeling of DFIM-based WSs in more detail. In addition, the next section approximates the RoCoF for (V)SM-based power systems.

A. MECHANICAL SYSTEM AND (V)SM-BASED ROCOF

For turbine torque m_{t} and total moment of inertia Θ, the one-mass model in motor sign convention is given by[1] [28]

$$\underbrace{\tfrac{\mathrm{d}}{\mathrm{d}t}\omega_{\mathrm{m}}}_{=:\dot{\omega}_{\mathrm{m}}} = \frac{1}{\Theta}(m_{\mathrm{m}} - m_{\mathrm{t}}) \Rightarrow \omega_{\mathrm{m}}\Theta\tfrac{\mathrm{d}}{\mathrm{d}t}\omega_{\mathrm{m}} = \underbrace{\omega_{\mathrm{m}} m_{\mathrm{m}}}_{=:p_{\mathrm{m}}} - \underbrace{\omega_{\mathrm{m}} m_{\mathrm{t}}}_{=:p_{\mathrm{t}}}$$

$$\Rightarrow \dot{\Omega}_{\mathrm{m}} = \frac{M_{\mathrm{t}} - M_{\mathrm{m}}}{2H}, \quad \Omega_{\mathrm{m}} := \frac{\omega_{\mathrm{m}}}{\omega_{\mathrm{m,R}}}, \; M_{\mathrm{m/t}} := \frac{m_{\mathrm{m/t}}}{m_{\mathrm{m,R}}} \tag{3}$$

$$H := -\frac{E_{\mathrm{kin}}}{p_{\mathrm{m,R}}} := -\frac{\frac{1}{2}\Theta\omega_{\mathrm{m,R}}^2}{p_{\mathrm{m,R}}} > 0 \tag{4}$$

with normalization based on ratings in generator operating mode, i.e., $\omega_{\mathrm{m,R}} > 0$, $m_{\mathrm{m,R}} < 0$, and $p_{\mathrm{m,R}} < 0$. The inertia constant H in (4) is proportional to the kinetic energy E_{kin} stored in the WS's rotating masses, such as WT and DFIM.

For a (V)SM, assuming approximately rated grid frequency, i.e., $\Omega_{\mathrm{g}} := \omega_{\mathrm{g}}/\omega_{\mathrm{g,R}} \approx 1$, and grid synchronization, i.e., $\dot{\Omega}_{\mathrm{m}} = \dot{\Omega}_{\mathrm{g}}$, $\Omega_{\mathrm{m}} \approx \Omega_{\mathrm{g}} = 1$ in (3), it follows that:

$$\overset{(3)}{\Rightarrow} \quad \dot{\Omega}_{\mathrm{g}} = \frac{1}{2H}\Big(\underbrace{\Omega_{\mathrm{m}} M_{\mathrm{t}}}_{=:P_{\mathrm{t}}} - \underbrace{\Omega_{\mathrm{m}} M_{\mathrm{m}}}_{=:P_{\mathrm{m}}}\Big). \tag{5}$$

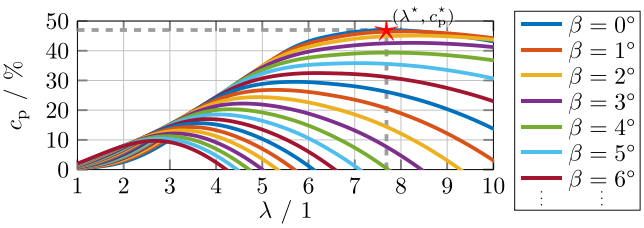

FIGURE 2. Power coefficient over tip speed ratio for different blade pitch angles with maximum coefficient $c_{\mathrm{p}}^\star := c_{\mathrm{p}}(\lambda^\star, \beta^\star = 0)$ at the MPP ★ from [28] and [31].

Aggregating all grid-connected SMs analogously to (5), the RoCoF depends on the power imbalance ΔP_{sys} [30], i.e.,[2]

$$\overset{(5)}{\Rightarrow} \dot{\Omega}_{\mathrm{sys}} = \frac{\Delta P_{\mathrm{sys}}}{2H_{\mathrm{sys}}} := \frac{P_{\mathrm{t,sys}} - P_{\mathrm{m,sys}}}{2H_{\mathrm{sys}}}, \; P_{\mathrm{m/t,sys}} := \frac{\sum p_{\mathrm{m/t},i}}{p_{\mathrm{sys,R}}}$$

$$H_{\mathrm{sys}} := -\frac{E_{\mathrm{kin,sys}}}{p_{\mathrm{sys,R}}} := -\frac{\sum E_{\mathrm{kin},i}}{p_{\mathrm{sys,R}}} := \frac{\sum H_i p_{\mathrm{m,R},i}}{p_{\mathrm{sys,R}}} > 0 \tag{6}$$

with machine/turbine power $p_{\mathrm{m/t},i}$ of the ith SM and overall system power $p_{\mathrm{sys,R}} := \sum p_{\mathrm{m},i}(t_0) < 0$ before an event at t_0. The system inertia constant H_{sys} is proportional to the system kinetic energy $E_{\mathrm{kin,sys}}$. Clearly, with decreasing H_{sys} in (6), the future RoCoF increases, especially for high ΔP_{sys}, leading to grid frequency instability or black-outs in the worst case [3], [4]. Thus, this article proposes inertia emulation based on the extraction of the WS's kinetic energy reserves or, if available, the WS's wind energy reserves.

Remark (R.1): *Considering a fault, e.g., with loss of SMs (or system split), the rated system power $p_{sys,\mathrm{R}} := \sum p_{\mathrm{m,R},i}$ is defined for postfault conditions, i.e., the aggregation only includes SMs that stay grid-connected. Similarly, the system inertia $H_{sys}(t)$ and the machine/turbine power $P_{\mathrm{m/t},sys}(t)$ are time-dependent, i.e., the aggregation only includes those SMs that stay grid-connected at that point in time t.*

B. AERODYNAMICS

The WT power and tip speed ratio are given by [28]

$$p_{\mathrm{t}} = p_{\mathrm{w}} c_{\mathrm{p}} := -\tfrac{1}{2}\rho\pi r_{\mathrm{t}}^2 v_{\mathrm{w}}^3 c_{\mathrm{p}}(\lambda, \beta), \; \lambda := \frac{\omega_{\mathrm{t}} r_{\mathrm{t}}}{v_{\mathrm{w}}} := \frac{\omega_{\mathrm{m}} r_{\mathrm{t}}}{n_{\mathrm{g}} v_{\mathrm{w}}} \tag{7}$$

respectively, with wind power p_{w}, air density ρ, turbine radius r_{t}, wind speed v_{w}, power coefficient c_{p}, blade pitch angle β, turbine angular velocity ω_{t}, and gearbox ratio n_{g}. Below cut-in wind speed $v_{\mathrm{w,cut\text{-}in}}$, the WS does not generate power, see region I in Fig. 5. For WT speeds above transition region I-II, the WT operates at its maximum power point (MPP) in region II, i.e., $(\lambda^\star, \beta^\star) := \arg\max c_{\mathrm{p}}(\lambda, \beta)$, see Fig. 2. Above rated and below cut-out wind speed, i.e., for $v_{\mathrm{w,R}} < v_{\mathrm{w}} \leq v_{\mathrm{w,cut\text{-}out}}$ in region III, β increases the limit ω_{m} to $\omega_{\mathrm{m,R}}$. For

[1] All quantities are transformed to the machine side or high-speed shaft.

[2] Extending (6) for IBRs or VSMs is discussed later, see Remark (R.9).

$v_\mathrm{w} > v_\mathrm{w,cut\text{-}out}$ in region IV, the WT is shut down. This article does not consider regions I and IV.

C. BLADE PITCH ANGLE CONTROL SYSTEM

The controlled pitch dynamics are approximated by [14]

$$\tfrac{\mathrm{d}}{\mathrm{d}t}\beta_\diamond := \mathrm{sat}_{-\dot\beta_\mathrm{max}}^{\dot\beta_\mathrm{max}}\left(\frac{1}{T_\beta}\left(\beta_\mathrm{ref}-\beta\right)\right), \quad \beta = \mathrm{sat}_{\beta_\mathrm{min}}^{\beta_\mathrm{max}}(\beta_\diamond) \tag{8}$$

with (blade) pitch angle limit $\beta_\mathrm{min/max}$, pitch angle rate limit $\dot\beta_\mathrm{max}$, pitch angle reference β_ref, auxiliary state $\beta_\diamond$, and pitch control system time constant T_β.

D. DOUBLY FED INDUCTION MACHINE

The electromagnetic DFIM dynamics are given by [15], [28]

$$\begin{pmatrix}\boldsymbol{u}_\mathrm{s}^{dq}\\ \boldsymbol{u}_\mathrm{r}^{dq}\end{pmatrix} = \begin{pmatrix}R_\mathrm{s}\boldsymbol{i}_\mathrm{s}^{dq}\\ R_\mathrm{r}\boldsymbol{i}_\mathrm{r}^{dq}\end{pmatrix} - \begin{pmatrix}\omega_\mathrm{s}^{dq}\boldsymbol{J}\boldsymbol{\psi}_\mathrm{s}^{dq}\\ \omega_\mathrm{r}^{dq}\boldsymbol{J}\boldsymbol{\psi}_\mathrm{r}^{dq}\end{pmatrix} + \tfrac{\mathrm{d}}{\mathrm{d}t}\begin{pmatrix}\boldsymbol{\psi}_\mathrm{s}^{dq}\\ \boldsymbol{\psi}_\mathrm{r}^{dq}\end{pmatrix} \tag{9}$$

with voltage $\boldsymbol{u}_\mathrm{s}^{dq} := (u_\mathrm{s}^d, u_\mathrm{s}^q)^\top$, $\boldsymbol{u}_\mathrm{r}^{dq} := (u_\mathrm{r}^d, u_\mathrm{r}^q)^\top$, current $\boldsymbol{i}_\mathrm{s}^{dq} := (i_\mathrm{s}^d, i_\mathrm{s}^q)^\top$, $\boldsymbol{i}_\mathrm{r}^{dq} := (i_\mathrm{r}^d, i_\mathrm{r}^q)^\top$, and magnetic flux linkage $\boldsymbol{\psi}_\mathrm{s}^{dq} := (\psi_\mathrm{s}^d, \psi_\mathrm{s}^q)^\top$, $\boldsymbol{\psi}_\mathrm{r}^{dq} := (\psi_\mathrm{r}^d, \psi_\mathrm{r}^q)^\top$ for stator and rotor dq-vectors, respectively, and with electrical angular velocities $\omega_\mathrm{s}^{dq} := -\omega_\mathrm{p}$, $\omega_\mathrm{r}^{dq} := n_\mathrm{p}\omega_\mathrm{m} - \omega_\mathrm{p}$, resistances R_s and R_r, for stator and rotor, respectively, with Park angular velocity $\omega_\mathrm{p} := \frac{\mathrm{d}}{\mathrm{d}t}\phi_\mathrm{p}$ and pole pair number n_p.

Assumption (A.1): The stator resistance is negligible in comparison to the stator reactance, i.e., $R_\mathrm{s} \ll \omega_\mathrm{p}L_\mathrm{s} =: X_\mathrm{s}$.

Considering steady state with $\frac{\mathrm{d}}{\mathrm{d}t}\boldsymbol{\psi}_\mathrm{s}^{dq} = \frac{\mathrm{d}}{\mathrm{d}t}\boldsymbol{\psi}_\mathrm{r}^{dq} = \boldsymbol{0}_2$ in (9), it follows that:

$$\overset{(9)}{\Rightarrow}\ \begin{pmatrix}\boldsymbol{u}_\mathrm{s}^{dq}\\ \boldsymbol{u}_\mathrm{r}^{dq}\end{pmatrix} = \begin{pmatrix}R_\mathrm{s}\boldsymbol{i}_\mathrm{s}^{dq} - \omega_\mathrm{s}^{dq}\boldsymbol{J}\left(L_\mathrm{s}\boldsymbol{i}_\mathrm{s}^{dq} + M_\mathrm{s,r}\boldsymbol{i}_\mathrm{r}^{dq}\right)\\ R_\mathrm{r}\boldsymbol{i}_\mathrm{r}^{dq} - \omega_\mathrm{r}^{dq}\boldsymbol{J}\left(M_\mathrm{s,r}\boldsymbol{i}_\mathrm{s}^{dq} + L_\mathrm{r}\boldsymbol{i}_\mathrm{r}^{dq}\right)\end{pmatrix} \tag{10}$$

using $\boldsymbol{\psi}_\mathrm{s}^{dq} = L_\mathrm{s}\boldsymbol{i}_\mathrm{s}^{dq} + M_\mathrm{s,r}\boldsymbol{i}_\mathrm{r}^{dq}$ and $\boldsymbol{\psi}_\mathrm{r}^{dq} = M_\mathrm{s,r}\boldsymbol{i}_\mathrm{s}^{dq} + L_\mathrm{r}\boldsymbol{i}_\mathrm{r}^{dq}$ with inductances L_s, L_r, and $M_\mathrm{s,r}$ for stator, rotor, and their magnetic coupling, respectively. Solving the first row in (10) for the stator currents in view of Assumption (A.1) yields

$$\overset{(10)}{\Rightarrow}\quad \boldsymbol{i}_\mathrm{s}^{dq} = \underbrace{\left[R_\mathrm{s}\boldsymbol{I}_2 - \omega_\mathrm{s}^{dq}L_\mathrm{s}\boldsymbol{J}\right]^{-1}}_{=:\boldsymbol{Y}}\left(\boldsymbol{u}_\mathrm{s}^{dq} - \omega_\mathrm{s}^{dq}\boldsymbol{J}M_\mathrm{s,r}\boldsymbol{i}_\mathrm{r}^{dq}\right) \tag{11}$$

$$\overset{(A.1)}{\Rightarrow}\quad \boldsymbol{i}_\mathrm{s}^{dq} = -\frac{1}{X_\mathrm{s}}\left(\boldsymbol{J}\boldsymbol{u}_\mathrm{s}^{dq} + X_\mathrm{s,r}\boldsymbol{i}_\mathrm{r}^{dq}\right),\ X_\mathrm{s,r} := \omega_\mathrm{p}M_\mathrm{s,r}. \tag{12}$$

The DFIM torque depends on the load angle δ, i.e., [28]

$$m_\mathrm{m} = -\kappa_\mathrm{p}n_\mathrm{p}(\boldsymbol{i}_\mathrm{r}^{dq})^\top\boldsymbol{J}\boldsymbol{\psi}_\mathrm{r}^{dq} \tag{13}$$

$$\overset{(12)}{=} -\kappa_\mathrm{p}n_\mathrm{p}\frac{M_\mathrm{s,r}}{X_\mathrm{s}}\underbrace{\widehat{u}_\mathrm{s}\begin{pmatrix}\cos(\phi_{u_\mathrm{s}}^{dq})\\ \sin(\phi_{u_\mathrm{s}}^{dq})\end{pmatrix}^\top}_{:=(\boldsymbol{u}_\mathrm{s}^{dq})^\top}\underbrace{\widehat{i}_\mathrm{r}\begin{pmatrix}\cos(\phi_{i_\mathrm{r}}^{dq})\\ \sin(\phi_{i_\mathrm{r}}^{dq})\end{pmatrix}}_{:=\boldsymbol{i}_\mathrm{r}^{dq}} \tag{14}$$

$$= -\kappa_\mathrm{p}n_\mathrm{p}\frac{M_\mathrm{s,r}}{X_\mathrm{s}}\widehat{u}_\mathrm{s}\widehat{i}_\mathrm{r}\sin(\delta),\ \delta := \phi_{i_\mathrm{r}}^{dq} + \tfrac{\pi}{2} - \phi_{u_\mathrm{s}}^{dq} \tag{15}$$

with power factor $\kappa_\mathrm{p} := \frac{2}{3\kappa^2}$, and stator voltage angle $\phi_{u_\mathrm{s}}^{dq} = 0$ for a grid-voltage-aligned dq-reference frame, see Fig. 3(a).

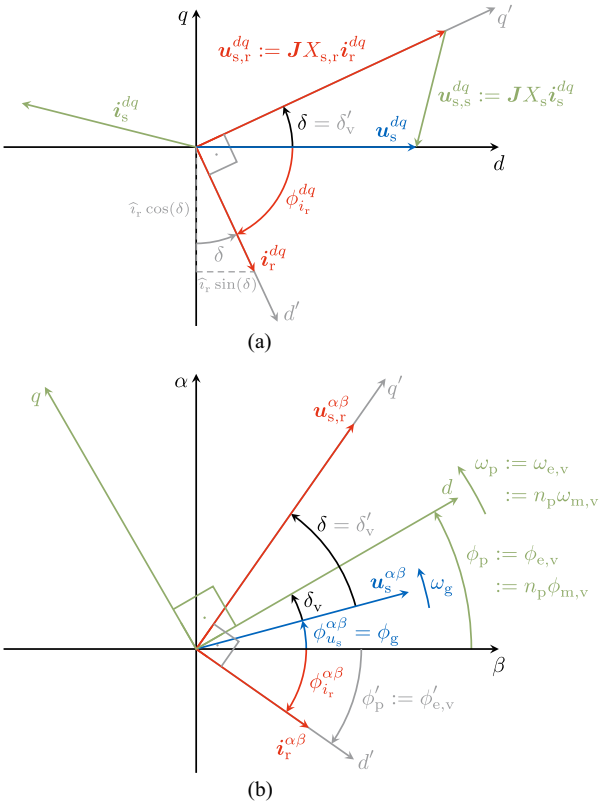

FIGURE 3. Load angle vector diagram in (12), (14), and [28], for (quasi-) steady state $\frac{\mathrm{d}}{\mathrm{d}t}\boldsymbol{i}_\mathrm{s}^{dq} = \frac{\mathrm{d}}{\mathrm{d}t}\boldsymbol{i}_\mathrm{r}^{dq} = \boldsymbol{0}_2$ and negligible stator resistance in (A.1). (a) Fault-free case with grid voltage aligned *dq*-reference frame. (b) Fault with negative RoCoF and VSM aligned *dq*-reference frame.

E. DC-LINK

The dc-link voltage dynamics are given by, see Fig. 1

$$\tfrac{\mathrm{d}}{\mathrm{d}t}u_\mathrm{dc} = \frac{i_\mathrm{c,dc}}{C_\mathrm{dc}} = \frac{1}{C_\mathrm{dc}}\left(i_\mathrm{f,dc} - i_\mathrm{r,dc} - \frac{u_\mathrm{dc}}{R_\mathrm{dc}}\right). \tag{16}$$

The GSI and RSI dc-link currents $i_\mathrm{f,dc}$ and $i_\mathrm{r,dc}$ are derived by the active power equality between ac- and dc-terminals of an ideal average inverter model, i.e., [14]

$$\begin{pmatrix}p_\mathrm{r}\\ p_\mathrm{f}\end{pmatrix} = \begin{pmatrix}\kappa_\mathrm{p}(\boldsymbol{u}_\mathrm{r}^{dq})^\top\boldsymbol{i}_\mathrm{r}^{dq}\\ \kappa_\mathrm{p}(\boldsymbol{u}_\mathrm{f}^{dq})^\top\boldsymbol{i}_\mathrm{f}^{dq}\end{pmatrix} = \begin{pmatrix}u_\mathrm{dc}i_\mathrm{r,dc}\\ u_\mathrm{dc}i_\mathrm{f,dc}\end{pmatrix} \Rightarrow i_\mathrm{r/f,dc} = \frac{p_\mathrm{r/f}}{u_\mathrm{dc}}. \tag{17}$$

Inserting (17) into (16), the dc-link voltage dynamics can be rewritten as function of the ac- or dq-currents, i.e.,

$$\overset{(16)}{\underset{(17)}{\Rightarrow}}\ \tfrac{\mathrm{d}}{\mathrm{d}t}u_\mathrm{dc} = \frac{\kappa_\mathrm{p}}{C_\mathrm{dc}u_\mathrm{dc}}\left((\boldsymbol{u}_\mathrm{f}^{dq})^\top\boldsymbol{i}_\mathrm{f}^{dq} - (\boldsymbol{u}_\mathrm{r}^{dq})^\top\boldsymbol{i}_\mathrm{r}^{dq} - \frac{u_\mathrm{dc}^2}{\kappa_\mathrm{p}R_\mathrm{dc}}\right). \tag{18}$$

Remark (R.2): *The energy stored in the dc-link capacity is negligible in comparison to the kinetic energy reserves, cf. [14], i.e., despite $|p_\mathrm{m,R}| > |p_\mathrm{f,R}|$, it follows that:*

$$H_\mathrm{dc} := -\frac{\frac{1}{2}C_\mathrm{dc}u_\mathrm{dc}^2}{p_\mathrm{f,R}} = 48\ \mathrm{ms} \ll H \overset{(4)}{:=} -\frac{\frac{1}{2}\Theta\omega_\mathrm{m,R}^2}{p_\mathrm{m,R}} = 7.816\ \mathrm{s}$$

with rated GSI or LC(L)-filter active power $p_\mathrm{f,R}$. Thus, this article considers the well-known GFL control for the GSI.

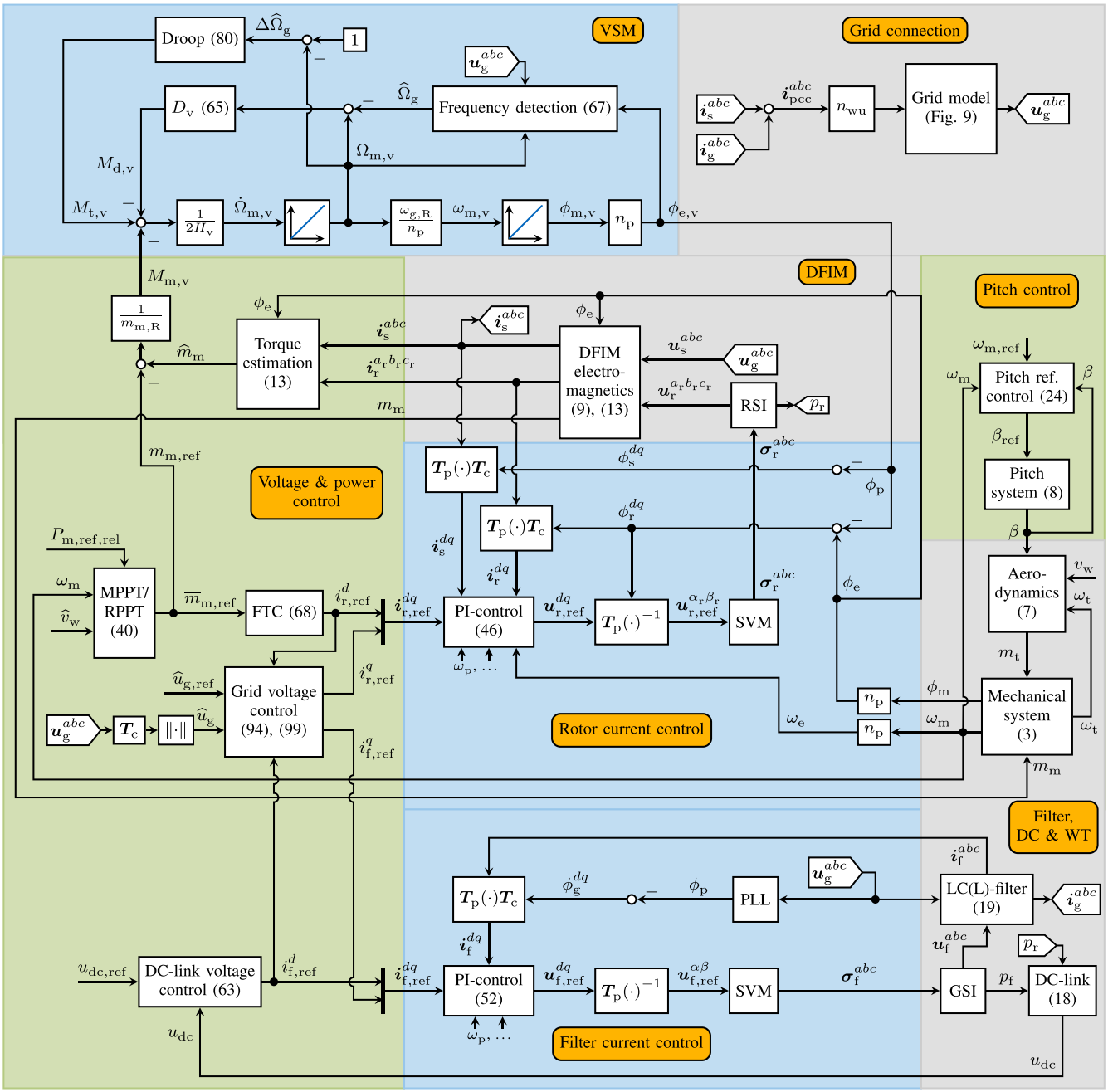

FIGURE 4. Modeling and proposed VSM control for DFIM-based WSs.

F. LC(L)-FILTER

The *LCL*-filter dynamics are given by, see Fig. 1

$$\frac{\mathrm{d}}{\mathrm{d}t}\begin{pmatrix}\boldsymbol{i}_f^{dq}\\ \boldsymbol{i}_g^{dq}\\ \boldsymbol{u}_c^{dq}\end{pmatrix} = \boldsymbol{A}_{lcl}\begin{pmatrix}\boldsymbol{i}_f^{dq}\\ \boldsymbol{i}_g^{dq}\\ \boldsymbol{u}_c^{dq}\end{pmatrix} + \begin{bmatrix}-\frac{1}{L_f}\boldsymbol{I}_2 & \boldsymbol{O}_{2\times2}\\ \boldsymbol{O}_{2\times2} & \frac{1}{L_g}\boldsymbol{I}_2\\ \boldsymbol{O}_{2\times2} & \boldsymbol{O}_{2\times2}\end{bmatrix}\begin{pmatrix}\boldsymbol{u}_f^{dq}\\ \boldsymbol{u}_g^{dq}\end{pmatrix}$$

$$\boldsymbol{A}_{lcl} := \begin{bmatrix}-\frac{R_f+R_c}{L_f}\boldsymbol{I}_2 - \omega_p\boldsymbol{J} & \frac{R_c}{L_f}\boldsymbol{I}_2 & \frac{1}{L_f}\boldsymbol{I}_2\\ \frac{R_c}{L_g}\boldsymbol{I}_2 & -\frac{R_c+R_g}{L_g}\boldsymbol{I}_2 - \omega_p\boldsymbol{J} & -\frac{1}{L_g}\boldsymbol{I}_2\\ -\frac{1}{C_c}\boldsymbol{I}_2 & \frac{1}{C_c}\boldsymbol{I}_2 & -\omega_p\boldsymbol{J}\end{bmatrix}. \tag{19}$$

This article considers an *LC*-filter with negligible grid-side inductance and resistance, i.e., $L_g, R_g \approx 0$. However, assuming small positive values, i.e., $L_g, R_g > 0$, simplifies the implementation and simulation, see [2, Remark (R.3)].

III. PROPOSED CONTROL SYSTEM

The proposed control system, see Fig. 4, consists of different (i) low-level controls [ ], such as VSM control, rotor current control, and filter current control, or (ii) high-level controls [ ], such as voltage and power control and pitch control. The modeling [ ] was discussed in the previous section, whereas the control is discussed in the following.

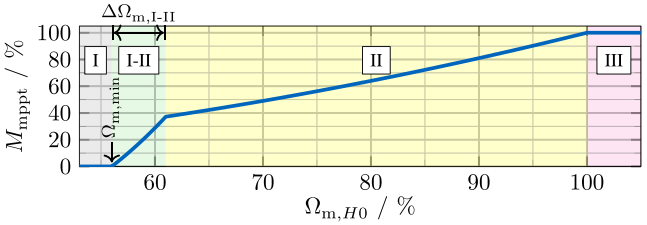

FIGURE 5. MPPT DFIM torque with $\Omega_{\mathrm{m},H0} = \Omega_{\mathrm{m}}$ during normal operation.

A. BLADE PITCH REFERENCE CONTROL

After reaching the rated DFIM torque, i.e., $m_{\mathrm{m}} = m_{\mathrm{m,R}}$, the control has to increase the blade pitch angle to limit the WT speed with increasing wind speed in region III [6], see also Fig. 5. Assuming constant DFIM speed and torque for small pitch angle changes $\Delta\beta$, i.e., $\frac{\partial\omega_{\mathrm{m}}}{\partial\beta}\Delta\beta \ll \omega_{\mathrm{m}}$ and $\frac{\partial m_{\mathrm{m}}}{\partial\beta}\Delta\beta \ll m_{\mathrm{m}}$, the DFIM power $p_{\mathrm{m}} = \omega_{\mathrm{m}} m_{\mathrm{m}}$ is constant for the control design, i.e., $\frac{\partial p_{\mathrm{m}}}{\partial\beta} = 0$. Thus, (3) simplifies to

$$\overset{(3)}{\Rightarrow}\quad \dot{\omega}_{\mathrm{m}} = \frac{1}{\Theta\omega_{\mathrm{m}}}(p_{\mathrm{m}} - p_{\mathrm{t}}) \Rightarrow \frac{\partial\dot{\omega}_{\mathrm{m}}}{\partial\beta} = \frac{-1}{\Theta\omega_{\mathrm{m}}}\frac{\partial p_{\mathrm{t}}}{\partial\beta} =: \frac{V}{T_{\mathrm{I}}}$$

$$\Rightarrow \Delta\dot{\omega}_{\mathrm{m}} = \frac{V}{T_{\mathrm{I}}}\Delta\beta,\ \ \Delta\dot{\omega}_{\mathrm{m}} := \omega_{\mathrm{m}} - \omega_{\mathrm{m}}^{*},\ \ \Delta\beta := \beta - \beta^{*} \quad (20)$$

with both, ω_{m}^{*} and $\beta^{*} := \beta^{*}(v_{\mathrm{w}})$, evaluated at the wind-dependent steady-state operating point denoted by $\bullet^{*}$. In region III, the small-signal state-space model is

$$\boldsymbol{x} = \begin{pmatrix} \Delta\beta + \beta^{*} \\ \Delta\omega_{\mathrm{m}} \\ \xi \end{pmatrix} := \begin{pmatrix} \beta \\ \omega_{\mathrm{m}} - \omega_{\mathrm{m,ref}} \\ \xi \end{pmatrix}$$

$$\underset{(20)}{\overset{(8)}{\Rightarrow}}\quad \dot{\boldsymbol{x}} = \boldsymbol{A}\boldsymbol{x} + \boldsymbol{b}u + \boldsymbol{d},\quad y = \boldsymbol{c}^{\top}\boldsymbol{x} := \begin{pmatrix} 0 & 1 & 0 \end{pmatrix}\boldsymbol{x} \quad (21)$$

$$\boldsymbol{A} := \begin{bmatrix} -\frac{1}{T_\sigma} & 0 & 0 \\ \frac{V}{T_{\mathrm{I}}} & 0 & 0 \\ 0 & 1 & 0 \end{bmatrix},\quad \boldsymbol{b} := \begin{pmatrix} \frac{1}{T_\sigma} \\ 0 \\ 0 \end{pmatrix},\quad \boldsymbol{d} := \begin{pmatrix} 0 \\ -\frac{V}{T_{\mathrm{I}}}\beta^{*} \\ 0 \end{pmatrix}$$

with reference angular velocity $\omega_{\mathrm{m,ref}} = \omega_{\mathrm{m,R}} = \omega_{\mathrm{m}}^{*}$, input $u := \beta_{\mathrm{ref}} := -\boldsymbol{k}^{\top}\boldsymbol{x} := -\begin{pmatrix} k_1 & k_2 & k_3 \end{pmatrix}\boldsymbol{x}$, and $T_\sigma = T_\beta$. Note that the disturbance $\boldsymbol{d}$ in (21) depends on v_{w} due to $\beta^{*} := \beta^{*}(v_{\mathrm{w}})$. With integral state ξ added in (21) to reach $\frac{\mathrm{d}}{\mathrm{d}t}\xi := \omega_{\mathrm{m}} - \omega_{\mathrm{m,ref}} = 0$, the steady state is given by

$$\dot{\boldsymbol{x}} \overset{!}{=} 0 \quad \overset{(21)}{\Rightarrow} \quad \boldsymbol{x} = \begin{pmatrix} \beta \\ \omega_{\mathrm{m}} - \omega_{\mathrm{m,ref}} \\ \xi \end{pmatrix} = \begin{pmatrix} \beta^{*} \\ 0 \\ -\frac{1+k_1}{k_3}\beta^{*} \end{pmatrix}. \quad (22)$$

Now, comparing the closed-loop characteristic polynomial

$$\det\left(\boldsymbol{A} - \boldsymbol{b}\boldsymbol{k}^{\top} - \lambda\boldsymbol{I}_3\right) = \lambda^3 + \lambda^2\frac{1+k_1}{T_\sigma} + \lambda\frac{Vk_2}{T_{\mathrm{I}}T_\sigma} + \frac{Vk_3}{T_{\mathrm{I}}T_\sigma}$$

with some desired third-order polynomial

$$\lambda^3 + \lambda^2\left(\tfrac{1}{T_{\mathrm{w}}} + 2\zeta\omega\right) + \lambda\left(\omega^2 + \tfrac{2\zeta\omega}{T_{\mathrm{w}}}\right) + \tfrac{\omega^2}{T_{\mathrm{w}}} \quad (23)$$

leads to the state feedback gain vector [28]

$$\boldsymbol{k}^{\top} = \left(T_\sigma\left(\tfrac{1}{T_{\mathrm{w}}} + 2\zeta\omega\right) - 1,\quad \tfrac{T_{\mathrm{I}}T_\sigma}{V}\left(\omega^2 + \tfrac{2\zeta\omega}{T_{\mathrm{w}}}\right),\quad \tfrac{\omega^2 T_{\mathrm{I}}T_\sigma}{T_{\mathrm{w}}V}\right)$$

with tuning parameters T_{w}, ω, and ζ. The latter two are chosen based on the proportional integral (PI) control design proposed in [31]. However, Jonkman et al. [31] neglected the pitch actuation delay introduced by the first-order lag system (8), i.e., Jonkman et al. [31] assumed $\beta = \beta_{\mathrm{ref}}$. Thus, the state $x_1 = \beta$ does not exist in [31] and the feedback is based on x_2 and x_3 only. Hackl et al. [14] took the pitch actuation delay into account for modeling but also solely used PI control. In contrast to those references, the proposed feedback improves the control performance by requiring less (transient) pitch actuation, see [2, Fig. 15].

Finally, the controller output and the integral state derivative are saturated based on the limits in (8), i.e.,[3]

$$u := \mathrm{sat}_{\beta_{\min}}^{\beta_{\max}}\left(-\boldsymbol{k}^{\top}\boldsymbol{x}\right),\quad \tfrac{\mathrm{d}}{\mathrm{d}t}x_3 = \tfrac{1}{k_3}\mathrm{sat}_{-\dot{\beta}_{\max}}^{\dot{\beta}_{\max}}\left(k_3 x_3\right). \quad (24)$$

B. POWER POINT TRACKING

The power point tracking modes, namely, 1) MPPT including MPPT compensation for inertia emulation or 2) RPPT, set the DFIM torque reference as discussed in the following.

1) MAXIMUM POWER POINT TRACKING

With the MPPT gain $K_{\mathrm{p}}^{\star} := -\frac{1}{2}\rho\pi\frac{r_{\mathrm{t}}^5}{(n_{\mathrm{g}}\lambda^{\star})^3}c_{\mathrm{p}}^{\star}\frac{\omega_{\mathrm{m,R}}^2}{m_{\mathrm{m,R}}}$ [28] and taking the power rating into account, i.e., $P_{\mathrm{m}} = \frac{p_{\mathrm{m}}}{p_{\mathrm{m,R}}} \overset{!}{\leq} 1$, the MPPT reference torque is defined as

$$M_{\mathrm{mppt}} := \begin{cases} f_{\mathrm{t,I\text{-}II}}(\Omega_{\mathrm{m},H0})K_{\mathrm{p}}^{\star}\Omega_{\mathrm{m},H0}^2, & \text{if } \Omega_{\mathrm{m},H0} \leq 1, \\ 1, & \text{otherwise,} \end{cases} \quad (25)$$

$$\Rightarrow\ P_{\mathrm{mppt}} := \Omega_{\mathrm{m},H0}M_{\mathrm{mppt}} \quad (26)$$

with smooth transitioning between regions I and II by

$$f_{\mathrm{t,I\text{-}II}}(\Omega_{\mathrm{m},H0}) := f_{\mathrm{t}}(-\Omega_{\mathrm{m},H0}, \Omega_{\mathrm{m,min}}, \Delta\Omega_{\mathrm{m,I\text{-}II}}) \quad (27)$$

$$f_{\mathrm{t}}(x, \widehat{a}, \Delta) := \begin{cases} 0, & \text{if } x \geq \widehat{a}, \\ \frac{\widehat{a}-x}{\Delta}, & \text{else if } x \geq \widehat{a} - \Delta, \\ 1, & \text{otherwise,} \end{cases} \quad (28)$$

with modified DFIM angular velocity $\Omega_{\mathrm{m},H0}$, defined later in (32); $\Omega_{\mathrm{m,min}}$ and $\Delta\Omega_{\mathrm{m,I\text{-}II}}$ define the start and length of the transition region I-II in (28), see Fig. 5.

2) MPPT COMPENSATION

Assuming $\Omega_{\mathrm{m},H0} = \Omega_{\mathrm{m}}$ in (25), M_{mppt} would decrease if the WT decelerates, counteracting the desired inertial response to RoCoF events [11], [32]. The MPPT compensation circumvents this. A simple MPPT compensation is to sample and

[3] The anti-windup and gain scheduling for (24) to (i) achieve a smooth transition between regions II and III (based on [14]) and to (ii) take changes of V/T_{I} in (21) due to operating point variations into account are out of scope of this article (details available at the authors).

hold M_{mppt} when detecting a RoCoF [28]. In this case, temporarily ignoring WT speed changes, the WT deviates from its MPP. Depending on RoCoF, initial operating point, WT characteristics, and wind speed, an additional WT speed protection may be required to avoid inadmissable deceleration [32], [33]. Moreover, after a RoCoF event, the decreased WS output power during the WT speed recovery process has to be taken into account to avoid a secondary frequency event [32], [33].

The MPPT compensation proposed in [32] is based on the assumption that the extracted kinetic energies of VSM and WS are equal. In contrast to [28], the MPPT compensation in [32] takes WT or wind speed changes during the RoCoF event into account, but assumes an ideal inertial response without active saturations or protection schemes, see [2, Sec. III-B2] for more details. However, this assumption is not generally valid, e.g., the overload protection proposed in [28] may limit the output power.

This article proposes a novel MPPT compensation that improves [28] and [32] regarding WT speed protection or compensation accuracy. It is based on the integration of the actual torque control error e_M, i.e.,

$$\overset{(3)}{\Rightarrow} \dot{\Omega}_{\mathrm{m}} = \frac{M_{\mathrm{t}} - M_{\mathrm{m}}}{2H} = \frac{1}{2H}\underbrace{\left(\overline{M}_{\mathrm{m,ref}} - M_{\mathrm{m}}\right)}_{=:e_M} + \underbrace{\frac{M_{\mathrm{t}} - \overline{M}_{\mathrm{m,ref}}}{2H}}_{=:\frac{\mathrm{d}}{\mathrm{d}t}\Omega_{\mathrm{m},H0}}$$

$$\Rightarrow \Omega_{\mathrm{m},H0} = \Omega_{\mathrm{m}} - \frac{1}{2H}\int_{t_0}^{t} e_M(\tau)\,\mathrm{d}\tau\,, \quad e_M(t_0) = 0 \tag{29}$$

with the saturated DFIM torque reference $\overline{M}_{\mathrm{m,ref}}$ defined later in (39). Note that, during normal operation and for ideal FTC, there is no control error, i.e., $e_M = 0$ in (29). Thus, e_M corresponds (only) to the additional torque required for inertia emulation (and droop control) during RoCoF events.

A RoCoF is detected when the time derivative of the VSM angular velocity $\dot{\Omega}_{\mathrm{m,v}}$ (VSM RoCoF) exceeds a threshold $\epsilon > 0$, which activates the MPPT compensation. Moreover, a rate limiter is added to (29) for smooth transition between active and inactive MPPT compensation, i.e., with discrete control sampling index k and sampling time T_k, and with[4]

$$\xi[k] := \begin{cases} 0, & \text{if } |\dot{\Omega}_{\mathrm{m,v}}| \le \epsilon, \\ -\frac{T_k}{2H}e_M[k] + \xi[k-1], & \text{otherwise,} \end{cases} \tag{30}$$

$$\overset{(29)}{\Rightarrow} u[k] := \Omega_{\mathrm{m}}[k] - \xi[k], \quad \xi[0] := 0 \tag{31}$$

the MPPT compensation angular velocity is given by

$$\overset{(31)}{\Rightarrow} y[k] := \begin{cases} y[k-1] + \dot{\Omega}_{\max}T_k, & \text{if } \frac{u[k]-y[k-1]}{T_k} \ge \dot{\Omega}_{\max}, \\ y[k-1] - \dot{\Omega}_{\max}T_k, & \text{if } \frac{u[k]-y[k-1]}{T_k} \le \dot{\Omega}_{\max}, \\ u[k], & \text{otherwise,} \end{cases}$$

$$\Rightarrow \Omega_{\mathrm{m},H0}[k] := y[k], \quad y[0] = 0 \tag{32}$$

with rate limit $\dot{\Omega}_{\max} := \frac{1}{2H}$.

[4]Actually, to avoid excessive toggling between active and inactive MPPT compensation, $\dot{\Omega}_{\mathrm{m,v}}$ is filtered by a first-order system lag system with time constant $T_{\mathrm{f,va}}$ before evaluating $|\dot{\Omega}_{\mathrm{m,v}}| \le \epsilon$ in (30), see [2, Table X].

3) REFERENCE POWER POINT TRACKING

To increase the energy reserves for inertia emulation or droop control, RPPT based on the maximum rotation strategy [23] is derived in the following.

At the equilibrium point, WT and DFIM power are equal, i.e., for MPPT and a given wind speed v_{w}, the steady-state operating point $(\omega_{\mathrm{m}}^*, \beta^*)$ is given by

$$e(\omega_{\mathrm{m}}, \beta) := \underbrace{p_{\mathrm{w}}(v_{\mathrm{w}})c_{\mathrm{p}}(\omega_{\mathrm{m}}, \beta, v_{\mathrm{w}})}_{=p_{\mathrm{w}}c_{\mathrm{p}}=p_{\mathrm{t}}} - \underbrace{\omega_{\mathrm{m}}m_{\mathrm{m}}(\omega_{\mathrm{m}})}_{=\omega_{\mathrm{m}}m_{\mathrm{m}}=p_{\mathrm{m}}} \overset{!}{=} 0$$

$$\Rightarrow \quad (\omega_{\mathrm{m}}^*, \beta^*) := \arg\min\{|e(\omega_{\mathrm{m}}, \beta)|\}|_{v_{\mathrm{w}}}$$

$$\text{such that} \begin{cases} \omega_{\mathrm{m,min}} \le \omega_{\mathrm{m}} \le \omega_{\mathrm{m,R}}, \\ \beta_{\min} \le \beta \le \beta_{\max}, \\ \beta_{\min} = \beta, \quad \text{if } v_{\mathrm{w}} \le v_{\mathrm{w,R}}, \\ \omega_{\mathrm{m,R}} = \omega_{\mathrm{m}}, \quad \text{if } v_{\mathrm{w}} > v_{\mathrm{w,R}}, \end{cases} \tag{33}$$

where $c_{\mathrm{p}}(\omega_{\mathrm{m}}, \beta, v_{\mathrm{w}}) := c_{\mathrm{p}}(\lambda = \frac{\omega_{\mathrm{m}}r_{\mathrm{t}}}{n_{\mathrm{g}}v_{\mathrm{w}}}, \beta)$ and $m_{\mathrm{m}}(\omega_{\mathrm{m}}) := M_{\mathrm{mppt}}(\Omega_{\mathrm{m},H0} = \frac{\omega_{\mathrm{m}}}{\omega_{\mathrm{m,R}}})m_{\mathrm{m,R}}$. Estimating the available turbine power $\overline{P}_{\mathrm{t}}^{\star}(\widehat{v}_{\mathrm{w}})$, saturated by the WS operating limits, with measured wind velocity $\widehat{v}_{\mathrm{w}}$ and defining the relative DFIM power reference $P_{\mathrm{m,ref,rel}}$ in the range 0%–100%, the DFIM power reference [in per unit (p.u.)] is given by[5]

$$P_{\mathrm{m,ref}}(\widehat{v}_{\mathrm{w}}) := \begin{cases} P_{\mathrm{m,ref,rel}}\overline{P}_{\mathrm{t}}^{\star}(\widehat{v}_{\mathrm{w}}), & \text{for } P_{\mathrm{m,ref,rel}} < 1 \\ \infty, & \text{otherwise.} \end{cases} \tag{34}$$

$$\overline{P}_{\mathrm{t}}^{\star}(v_{\mathrm{w}}) \overset{(7)}{:=} \underbrace{-\tfrac{1}{2}\rho\pi r_{\mathrm{t}}^2 v_{\mathrm{w}}^3}_{=:p_{\mathrm{w}}(v_{\mathrm{w}})} \frac{1}{p_{\mathrm{m,R}}}\overline{c}_{\mathrm{p}}^{\star}(v_{\mathrm{w}}) \tag{35}$$

$$\overline{c}_{\mathrm{p}}^{\star}(v_{\mathrm{w}}) := \lim_{t\to\infty} c_{\mathrm{p}}(t)\Big|_{\substack{v_{\mathrm{w}}(t) = v_{\mathrm{w}}, \\ P_{\mathrm{m,ref,rel}}(t) = 1}} \overset{(33)}{:=} c_{\mathrm{p}}(\omega_{\mathrm{m}}^*, \beta^*)|_{v_{\mathrm{w}}}. \tag{36}$$

Note that $P_{\mathrm{m,ref}}$ in (34) does not depend on $\widehat{v}_{\mathrm{w}}$ for MPPT with $P_{\mathrm{m,ref,rel}} = 1$, i.e., wind speed measurement is only required for $P_{\mathrm{m,ref,rel}} < 1$. Assuming constant v_{w} and $P_{\mathrm{m,ref,rel}} = 1$, the operating point reaches the equilibrium point with power coefficient $\overline{c}_{\mathrm{p}}^{\star}(v_{\mathrm{w}})$ for $t \to \infty$ in (36). Note that $\overline{c}_{\mathrm{p}}^{\star} = c_{\mathrm{p}}^{\star}$ holds in operation region II but not in I-II and III, i.e., with minimum region II wind speed $v_{\mathrm{w,II,min}}$

$$\overline{c}_{\mathrm{p}}^{\star}(v_{\mathrm{w}}) \overset{(33)}{\underset{(36)}{=}} \begin{cases} c_{\mathrm{p}}(\omega_{\mathrm{m}}^*, \beta^*)|_{v_{\mathrm{w}}}, & \text{if } v_{\mathrm{w,cut\text{-}in}} \le v_{\mathrm{w}} < v_{\mathrm{w,II,min}}, \\ c_{\mathrm{p}}^{\star} := \max c_{\mathrm{p}}, & \text{if } v_{\mathrm{w,II,min}} \le v_{\mathrm{w}} \le v_{\mathrm{w,R}}, \\ \frac{p_{\mathrm{m,R}}}{p_{\mathrm{w}}(v_{\mathrm{w}})}, & \text{if } v_{\mathrm{w,R}} < v_{\mathrm{w}} \le v_{\mathrm{w,cut\text{-}out}}, \end{cases}$$

for regions I-II, II, and III, respectively. For the transition region I-II, a numerical optimization algorithm solves the first case or (33) for different v_{w} offline (before operation) and the control approximates $\overline{c}_{\mathrm{p}}^{\star}(v_{\mathrm{w}})$ by a lookup table, which is evaluated online (during operation) at $\widehat{v}_{\mathrm{w}}$.

[5]Do not replace ∞ by 1 in (34) due to possible transients with $\omega_{\mathrm{m}} > \omega_{\mathrm{m,R}}$ or $\Omega_{\mathrm{m}} = \Omega_{\mathrm{m},H0} > 1$. In this case, the MPPT should apply the maximum torque, which is $M_{\mathrm{m,ref}} := \frac{1}{\Omega_{\mathrm{m}}}\mathrm{sat}_0^{P_{\mathrm{mppt}}(\Omega_{\mathrm{m},H0})}\infty = 1$ but not $M_{\mathrm{m,ref}} := \frac{1}{\Omega_{\mathrm{m}}}\mathrm{sat}_0^{P_{\mathrm{mppt}}(\Omega_{\mathrm{m},H0})}1 < 1$ in (37).

Taking wind speed measurement errors into account, the MPPT curve saturates the final DFIM power reference, i.e.,

$$M_{\mathrm{m,ref}} \overset{(26)}{\underset{(34)}{:=}} \frac{1}{\Omega_{\mathrm{m}}} \mathrm{sat}_0^{P_{\mathrm{mppt}}(\Omega_{\mathrm{m},H0})}\left(P_{\mathrm{m,ref}}\right) \tag{37}$$

$$\tfrac{\mathrm{d}}{\mathrm{d}t} M_{\diamond} := \mathrm{sat}_{-\dot{M}_{\mathrm{m,max}}}^{\dot{M}_{\mathrm{m,max}}}\left(M_{\mathrm{m,ref}}\right) \tag{38}$$

$$\overline{M}_{\mathrm{m,ref}} := \mathrm{sat}_0^{M_{\mathrm{m,max}}}\left(M_{\diamond}\right) \tag{39}$$

$$\Rightarrow \quad \overline{P}_{\mathrm{m,ref}} := \Omega_{\mathrm{m}} \overline{M}_{\mathrm{m,ref}}, \qquad \overline{m}_{\mathrm{m,ref}} := \overline{M}_{\mathrm{m,ref}} m_{\mathrm{m,R}} \tag{40}$$

with transient torque limit $M_{\mathrm{m,max}}$ and torque rate limit $\dot{M}_{\mathrm{m,max}}$. Note that the steady-state torque limit equals the rated torque, taken into account by the power saturation in (37), i.e., $M_{\mathrm{m,ref}} \leq 1$ during normal operation with $\Omega_{\mathrm{m},H0} = \Omega_{\mathrm{m}}$. However, for inertia emulation, $M_{\mathrm{m,ref}} > 1$ may be temporarily required to keep the power reference constant while the DFIM decelerates during active MPPT compensation with $\Omega_{\mathrm{m}} < \Omega_{\mathrm{m},H0}$ in (37). Thus, the DFIM torque reference is saturated by the above-rated or transient torque limit $M_{\mathrm{m,max}} > 1$ in (39), see [2, Table X].

C. CURRENT CONTROL

The control of the DFIM rotor and $LC(L)$-filter currents by the RSI and GSI, respectively, is derived in the following.

1) DFIM ROTOR CURRENT CONTROL

Rewriting (9) gives the rotor current dynamics as follows:

$$\overset{(9)}{\Rightarrow} L_{\mathrm{r}} \nu \tfrac{\mathrm{d}}{\mathrm{d}t} \boldsymbol{i}_{\mathrm{r}}^{dq} = \boldsymbol{u}_{\mathrm{r}}^{dq} - R_{\mathrm{r}} \boldsymbol{i}_{\mathrm{r}}^{dq} + \omega_{\mathrm{r}}^{dq} \boldsymbol{J} \boldsymbol{\psi}_{\mathrm{r}}^{dq} - \frac{M_{\mathrm{s,r}}}{L_{\mathrm{s}}} \left(\boldsymbol{u}_{\mathrm{s}}^{dq} - R_{\mathrm{s}} \boldsymbol{i}_{\mathrm{s}}^{dq} + \omega_{\mathrm{s}}^{dq} \boldsymbol{J} \boldsymbol{\psi}_{\mathrm{s}}^{dq} \right) \tag{41}$$

with $\nu := 1 - \frac{M_{\mathrm{s,r}}^2}{L_{\mathrm{s}} L_{\mathrm{r}}}$. Neglecting the inverter delay or dead time T_{dead} and inserting the RSI reference voltage

$$\boldsymbol{u}_{\mathrm{r}}^{dq} \approx \boldsymbol{u}_{\mathrm{r,ref}}^{dq} := \boldsymbol{u}_{\mathrm{r,pi}}^{dq} - \omega_{\mathrm{r}}^{dq} \boldsymbol{J} \boldsymbol{\psi}_{\mathrm{r}}^{dq} + \frac{M_{\mathrm{s,r}}}{L_{\mathrm{s}}} \left(\boldsymbol{u}_{\mathrm{s}}^{dq} - R_{\mathrm{s}} \boldsymbol{i}_{\mathrm{s}}^{dq} + \omega_{\mathrm{s}}^{dq} \boldsymbol{J} \boldsymbol{\psi}_{\mathrm{s}}^{dq} \right) \tag{42}$$

with the PI controller output voltage[6]

$$\boldsymbol{u}_{\mathrm{r,pi}}^{dq} = k_{\mathrm{p}} \left(\boldsymbol{i}_{\mathrm{r,ref}}^{dq} - \boldsymbol{i}_{\mathrm{r}}^{dq} \right) + k_{\mathrm{i}} \boldsymbol{\xi}^{dq}, \quad \tfrac{\mathrm{d}}{\mathrm{d}t} \boldsymbol{\xi}^{dq} = \boldsymbol{i}_{\mathrm{r,ref}}^{dq} - \boldsymbol{i}_{\mathrm{r}}^{dq} \tag{43}$$

into (41) yields the closed-loop rotor current dynamics

$$\overset{(41)}{\underset{(42)}{\Rightarrow}} \quad T_{\mathrm{r}} \tfrac{\mathrm{d}}{\mathrm{d}t} \boldsymbol{i}_{\mathrm{r}}^{dq} = \frac{1}{R_{\mathrm{r}}} \boldsymbol{u}_{\mathrm{r,pi}}^{dq} - \boldsymbol{i}_{\mathrm{r}}^{dq}, \quad T_{\mathrm{r}} := \frac{L_{\mathrm{r}} \nu}{R_{\mathrm{r}}} \tag{44}$$

$$\overset{(43)}{\Rightarrow} \quad \frac{i_{\mathrm{r}}^{d/q}(s)}{i_{\mathrm{r,ref}}^{d/q}(s)} = \frac{\frac{k_{\mathrm{p}}}{T_{\mathrm{r}} R_{\mathrm{r}}} s + \frac{k_{\mathrm{i}}}{T_{\mathrm{r}} R_{\mathrm{r}}}}{s^2 + \left(\frac{1}{T_{\mathrm{r}}} + \frac{k_{\mathrm{p}}}{T_{\mathrm{r}} R_{\mathrm{r}}} \right) s + \frac{k_{\mathrm{i}}}{T_{\mathrm{r}} R_{\mathrm{r}}}}. \tag{45}$$

The PI control gain tuning in (43) is based on the "magnitude optimum criterion" (see [34, Sec. 1.3.1, pp. 46–60]). Assuming a second-order lag system for the open-loop transfer function, called "PT_2" in [34], with steady-state gain $V_{\mathrm{S}} = 1/R_{\mathrm{r}}$, large time constant $T_1 = T_{\mathrm{r}}$, see (44), and small time constant $T_\sigma = T_{\mathrm{dead}}$ (see [34, Table 1.3, p. 82]), the proportional and integral control gains are given by

$$k_{\mathrm{p}} := \frac{T_{\mathrm{r}} R_{\mathrm{r}}}{2 T_{\mathrm{dead}}} = \frac{L_{\mathrm{r}} \nu}{2 T_{\mathrm{dead}}} \quad \text{and} \quad k_{\mathrm{i}} := \frac{R_{\mathrm{r}}}{2 T_{\mathrm{dead}}}. \tag{46}$$

2) LC(L)-FILTER CURRENT CONTROL

Considering a grounded LC-filter, see Fig. 1, it follows that:

$$R_{\mathrm{g}}, L_{\mathrm{g}} \approx 0 \Rightarrow \boldsymbol{u}_{\mathrm{g}}^{dq} = \boldsymbol{u}_{\mathrm{c}}^{dq} + R_{\mathrm{c}} \boldsymbol{i}_{\mathrm{c}}^{dq} = \boldsymbol{u}_{\mathrm{c}}^{dq} + R_{\mathrm{c}} \left(\boldsymbol{i}_{\mathrm{g}}^{dq} - \boldsymbol{i}_{\mathrm{f}}^{dq} \right). \tag{47}$$

Inserting (47) into (19) yields the filter current dynamics

$$\overset{(19)}{\underset{(47)}{\Rightarrow}} \quad \tfrac{\mathrm{d}}{\mathrm{d}t} \boldsymbol{i}_{\mathrm{f}}^{dq} = \frac{1}{L_{\mathrm{f}}} \left(-\boldsymbol{u}_{\mathrm{f}}^{dq} - R_{\mathrm{f}} \boldsymbol{i}_{\mathrm{f}}^{dq} - \omega_{\mathrm{p}} \boldsymbol{J} L_{\mathrm{f}} \boldsymbol{i}_{\mathrm{f}}^{dq} + \boldsymbol{u}_{\mathrm{g}}^{dq} \right). \tag{48}$$

The GSI reference voltage

$$\boldsymbol{u}_{\mathrm{f}}^{dq} \approx \boldsymbol{u}_{\mathrm{f,ref}}^{dq} := \boldsymbol{u}_{\mathrm{g}}^{dq} - \omega_{\mathrm{p}} \boldsymbol{J} L_{\mathrm{f}} \boldsymbol{i}_{\mathrm{f}}^{dq} - R_{\mathrm{f}} \boldsymbol{i}_{\mathrm{f}}^{dq} - L_{\mathrm{f}} \boldsymbol{u}_{\mathrm{f,pi}}^{dq} \tag{49}$$

with the PI controller output voltage[7]

$$\boldsymbol{u}_{\mathrm{f,pi}}^{dq} = k_{\mathrm{p}} \left(\boldsymbol{i}_{\mathrm{f,ref}}^{dq} - \boldsymbol{i}_{\mathrm{f}}^{dq} \right) + k_{\mathrm{i}} \boldsymbol{\xi}^{dq}, \quad \tfrac{\mathrm{d}}{\mathrm{d}t} \boldsymbol{\xi}^{dq} = \boldsymbol{i}_{\mathrm{f,ref}}^{dq} - \boldsymbol{i}_{\mathrm{f}}^{dq} \tag{50}$$

achieves input/output linearization (see also [35]), i.e., the closed-loop filter current dynamics are

$$\overset{(48)}{\underset{(49)}{\Rightarrow}} \quad \tfrac{\mathrm{d}}{\mathrm{d}t} \boldsymbol{i}_{\mathrm{f}}^{dq} = \boldsymbol{u}_{\mathrm{f,pi}}^{dq} \quad \overset{(50)}{\Rightarrow} \quad \frac{i_{\mathrm{f}}^{d/q}(s)}{i_{\mathrm{f,ref}}^{d/q}(s)} = \frac{k_{\mathrm{p}} s + k_{\mathrm{i}}}{s^2 + k_{\mathrm{p}} s + k_{\mathrm{i}}}. \tag{51}$$

An additional reference filter with time constant $T_{\mathrm{f}} := \frac{k_{\mathrm{p}}}{k_{\mathrm{i}}}$ eliminates the derivative term in the numerator of (51) to avoid overshooting, i.e., (51) is rewritten as

$$\frac{i_{\mathrm{f}}^{d/q}(s)}{i_{\mathrm{f,ref}}^{d/q}(s)} = \frac{1}{1 + s T_{\mathrm{f}}} \frac{k_{\mathrm{p}} s + k_{\mathrm{i}}}{s^2 + k_{\mathrm{p}} s + k_{\mathrm{i}}} = \frac{k_{\mathrm{i}}}{s^2 + k_{\mathrm{p}} s + k_{\mathrm{i}}} =: \frac{\omega^2}{s^2 + 2\zeta\omega s + \omega^2}, \text{ where } k_{\mathrm{p}} := 2\zeta\omega \text{ and } k_{\mathrm{i}} = \omega^2 \tag{52}$$

depend on the tuning parameters ω and ζ, see [2, Table X].

D. DC-LINK VOLTAGE CONTROL

The control should keep the dc-link voltage u_{dc} close to its reference or rated value $u_{\mathrm{dc,ref}} := u_{\mathrm{dc,R}}$ by balancing the energy or active power of RSI and GSI, see (17) and (18). In this article, the RSI controls the DFIM power, whereas the GSI controls u_{dc} by corresponding grid-side filter active power injection (see Fig. 4) as discussed in the following.

Solving (48) for $\boldsymbol{u}_{\mathrm{f}}^{dq}$ in the grid-voltage-aligned dq-reference frame, i.e., $\boldsymbol{u}_{\mathrm{g}}^{dq} = (\widehat{u}_{\mathrm{g}}, 0)^\top$, the GSI active and reactive power can be written as, see [6]

$$p_{\mathrm{f}} = \kappa_{\mathrm{p}} (\boldsymbol{i}_{\mathrm{f}}^{dq})^\top \boldsymbol{u}_{\mathrm{f}}^{dq}$$

[6]The implemented anti-windup and inverter dead time compensation are out of scope of this article (details available at the authors).

[7]The implemented anti-windup and inverter dead time compensation are out of scope of this article (details available at the authors).

$$\overset{(48)}{=} \kappa_\mathrm{p}\widehat{u}_\mathrm{g} i_\mathrm{f}^d - \kappa_\mathrm{p} L_\mathrm{f} (\boldsymbol{i}_\mathrm{f}^{dq})^\top \tfrac{\mathrm{d}}{\mathrm{d}t}\boldsymbol{i}_\mathrm{f}^{dq} - \kappa_\mathrm{p} R_\mathrm{f} (\widehat{\imath}_\mathrm{f})^2 \tag{53}$$

$$q_\mathrm{f} = -\kappa_\mathrm{p} (\boldsymbol{i}_\mathrm{f}^{dq})^\top \boldsymbol{J} \boldsymbol{u}_\mathrm{f}^{dq}$$

$$\overset{(48)}{=} -\kappa_\mathrm{p} \widehat{u}_\mathrm{g} i_\mathrm{f}^q - \kappa_\mathrm{p} \omega_\mathrm{p} L_\mathrm{f} (\widehat{\imath}_\mathrm{f})^2 + \kappa_\mathrm{p} L_\mathrm{f} (\boldsymbol{i}_\mathrm{f}^{dq})^\top \boldsymbol{J} \tfrac{\mathrm{d}}{\mathrm{d}t}\boldsymbol{i}_\mathrm{f}^{dq}. \tag{54}$$

Inserting (53) into (18), the dc-link voltage dynamics are

$$\overset{(18)}{\underset{(53)}{\Rightarrow}} \tfrac{\mathrm{d}}{\mathrm{d}t} u_\mathrm{dc} = \frac{1}{C_\mathrm{dc} u_\mathrm{dc}} \Big(\kappa_\mathrm{p} \widehat{u}_\mathrm{g} i_\mathrm{f}^d - \kappa_\mathrm{p} L_\mathrm{f} (\boldsymbol{i}_\mathrm{f}^{dq})^\top \tfrac{\mathrm{d}}{\mathrm{d}t}\boldsymbol{i}_\mathrm{f}^{dq} - \kappa_\mathrm{p} R_\mathrm{f} (\widehat{\imath}_\mathrm{f})^2 - p_\mathrm{r} - u_\mathrm{dc}^2 / R_\mathrm{dc} \Big). \tag{55}$$

Inserting the approximated controlled filter current dynamics

$$1/\omega^2 \approx 0 \quad \overset{(52)}{\Rightarrow} \quad \tfrac{\mathrm{d}}{\mathrm{d}t}\boldsymbol{i}_\mathrm{f}^{dq} = \frac{1}{T_\mathrm{f}} \left(\boldsymbol{i}_{\mathrm{f,ref}}^{dq} - \boldsymbol{i}_\mathrm{f}^{dq} \right) \tag{56}$$

into (55) yields

$$\overset{(55)}{\underset{(56)}{\Rightarrow}} \quad \tfrac{\mathrm{d}}{\mathrm{d}t} u_\mathrm{dc} = \frac{1}{C_\mathrm{dc} u_\mathrm{dc}} \Big(\kappa_\mathrm{p} \widehat{u}_\mathrm{g} i_\mathrm{f}^d - \kappa_\mathrm{p} \frac{L_\mathrm{f}}{T_\mathrm{f}} (\boldsymbol{i}_\mathrm{f}^{dq})^\top \boldsymbol{i}_{\mathrm{f,ref}}^{dq} + \kappa_\mathrm{p} \left(\frac{L_\mathrm{f}}{T_\mathrm{f}} - R_\mathrm{f} \right) (\widehat{\imath}_\mathrm{f})^2 - p_\mathrm{r} \Big) - \frac{u_\mathrm{dc}}{R_\mathrm{dc} C_\mathrm{dc}}. \tag{57}$$

The required steady-state reference filter d-current to fulfill $\frac{\mathrm{d}}{\mathrm{d}t} u_\mathrm{dc} = 0$ in (57), $\frac{\mathrm{d}}{\mathrm{d}t}\boldsymbol{i}_\mathrm{f}^{dq} = \boldsymbol{0}_2$ in (56), and $u_\mathrm{dc} \overset{!}{=} u_{\mathrm{dc,ref}}$ can be derived and defined as feedforward control term, see [2, Sec. III-D]

$$i_{\mathrm{f,FF}}^d := \frac{\|\widehat{\boldsymbol{u}}_\mathrm{g}^{dq}\|}{2R_\mathrm{f}} - \sqrt{\frac{1}{\kappa_\mathrm{p} R_\mathrm{f}} \left(\kappa_\mathrm{p} \frac{\|\widehat{\boldsymbol{u}}_\mathrm{g}^{dq}\|^2}{4R_\mathrm{f}} - \frac{u_{\mathrm{dc,ref}}^2}{R_\mathrm{dc}} - \widehat{p}_\mathrm{r} \right)} \tag{58}$$

based on measured grid voltage and estimated rotor power

$$\tfrac{\mathrm{d}}{\mathrm{d}t} \|\widehat{\boldsymbol{u}}_\mathrm{g}^{dq}\| := \frac{\|\boldsymbol{u}_\mathrm{g}^{dq}\| - \|\widehat{\boldsymbol{u}}_\mathrm{g}^{dq}\|}{T_\mathrm{FF}}, \quad \tfrac{\mathrm{d}}{\mathrm{d}t} \widehat{p}_\mathrm{r} := \frac{\kappa_\mathrm{p} (\boldsymbol{u}_{\mathrm{r,ref}}^{dq})^\top \boldsymbol{i}_{\mathrm{r,ref}}^{dq} - \widehat{p}_\mathrm{r}}{T_\mathrm{FF}}$$

with feedforward filter time constant T_FF.

Defining the state vector $\boldsymbol{x}^\top := (\boldsymbol{i}_\mathrm{f}^{dq}, u_\mathrm{dc}, \xi)^\top$ with integral state ξ, the input $u := i_{\mathrm{f,ref}}^d$, the disturbance vector $\boldsymbol{v}^\top := (i_{\mathrm{f,ref}}^q, p_\mathrm{r}, \widehat{u}_\mathrm{g})^\top$, and the (small-signal) state feedback

$$\Delta u := \Delta i_{\mathrm{f,ref}}^d := -\boldsymbol{k}^\top \Delta \boldsymbol{x} := - \begin{pmatrix} \boldsymbol{0}_2 \\ k_2 \\ k_3 \end{pmatrix}^\top \begin{pmatrix} \Delta \boldsymbol{i}_\mathrm{f}^{dq} \\ \Delta u_\mathrm{dc} \\ \Delta \xi \end{pmatrix} \tag{59}$$

with gain vector $\boldsymbol{k}$ and $\frac{\mathrm{d}}{\mathrm{d}t}\Delta\xi := u_\mathrm{dc} - u_{\mathrm{dc,ref}}$, the small-signal closed-loop state space model can be written as

$$\tfrac{\mathrm{d}}{\mathrm{d}t}\Delta\dot{\boldsymbol{x}} = \boldsymbol{A}\Delta\boldsymbol{x} + \boldsymbol{b}\Delta u + \boldsymbol{D}\Delta\boldsymbol{v} \overset{(59)}{=} \boldsymbol{A}_\mathrm{cl}\Delta\boldsymbol{x} + \boldsymbol{D}\Delta\boldsymbol{v} \tag{60}$$

with $\boldsymbol{A}_\mathrm{cl} := \boldsymbol{A} - \boldsymbol{b}\boldsymbol{k}^\top$, where the system matrix $\boldsymbol{A}$, the input vector $\boldsymbol{b}$, and the disturbance matrix $\boldsymbol{D}$ are linearized at the steady-state operating point with $u_\mathrm{dc} = u_{\mathrm{dc,ref}}$, see [2, Sec. III-D] for details. The characteristic polynomial

$$\overset{(60)}{\Rightarrow} \det(\lambda \boldsymbol{I} - \boldsymbol{A}_\mathrm{cl}) = \lambda^4 + \lambda^3 a_3 + \lambda^2 a_2 + \lambda a_1 + a_0 \tag{61}$$

with coefficients a_0,..., a_3, is Hurwitz (proven for the considered WS parameters from [2] using MATLAB) if the proportional and integral gains are chosen as follows:

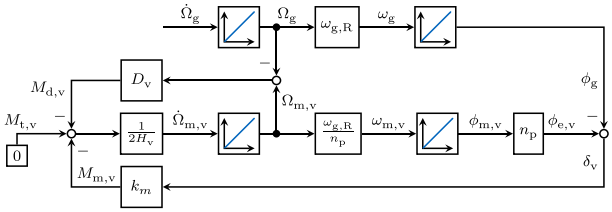

FIGURE 6. Freely spinning VSM torque synchronization loop [18], [28], in view of Assumption (A.2).

$$k_\mathrm{p} := k_2 := \frac{\widehat{\imath}_{\mathrm{f,max}}}{50\% \cdot u_{\mathrm{dc,R}}} \text{ and } k_\mathrm{i} := k_3 := \frac{\widehat{\imath}_{\mathrm{f,max}} \cdot 1\,\mathrm{s}}{0.5\% \cdot u_{\mathrm{dc,R}}}. \tag{62}$$

The nonaggressive tuning of k_p, see its relatively small value in (62), (i) avoids relatively high feedback or filter current oscillations $\Delta u = \Delta i_{\mathrm{f,ref}}^d \propto k_\mathrm{p} \Delta u_\mathrm{dc}$ for relatively small u_dc oscillations (e.g., induced by $\boldsymbol{i}_\mathrm{r}^{dq}$ disturbances) and (ii) ensures stability in the face of the nonminimum-phase behavior, see also [6]. However, in combination with the rather large integral gain k_i in (62) and the feedforward control (58), accurate dc-link voltage tracking is achieved by the overall filter d-current reference

$$\overset{(58)}{\underset{(59)}{\Rightarrow}} \quad i_{\mathrm{f,ref}}^d := i_{\mathrm{f,FF}}^d + \Delta i_{\mathrm{f,ref}}^d. \tag{63}$$

Remark (R.3): *Note that (63) chooses $i_{\mathrm{f},ref}^d$ to control u_{dc}, since the active filter power p_f in the u_{dc} dynamics only depends on i_f^d at steady state with $\frac{\mathrm{d}}{\mathrm{d}t}\boldsymbol{i}_\mathrm{f}^{dq} = \boldsymbol{0}_2$, assuming constant $\widehat{u}_\mathrm{g}$ and negligible R_f, see (53) and (55). Later on, $i_{\mathrm{f},ref}^q$ controls the reactive power or grid voltage, since q_f also depends on i_f^q at steady state, see (54).*

E. VIRTUAL SYNCHRONOUS MACHINE

For the discussion of the proposed VSM control method, the following assumption is imposed in this subsection.

Assumption (A.2): For a freely spinning VSM, the virtual turbine torque is zero, i.e., $M_{\mathrm{t,v}} = 0$.

The VSM mechanical dynamics are based on the one-mass model dynamics (3) and the VSM electromagnetical dynamics are based on the modeling of directly grid-connected SMs. The resulting torque synchronization loop of a freely spinning VSM aligns its electrical rotor angle $\phi_{\mathrm{e,v}}$ with the grid voltage angle ϕ_g as explained in the following based on Fig. 6. In view of Assumption (A.2), the VSM machine torque $M_{\mathrm{m,v}}$ and the VSM damper torque $M_{\mathrm{d,v}}$ are zero at steady state, i.e., $M_{\mathrm{t,v}} = M_{\mathrm{m,v}} = M_{\mathrm{d,v}} = 0$. For a RoCoF $\dot{\Omega}_\mathrm{g} \neq 0$, the synchronizing feedback $M_{\mathrm{m,v}} := k_m \delta_\mathrm{v} := k_m(\phi_{\mathrm{e,v}} - \phi_\mathrm{g})$ counteracts the deviation between VSM electrical angle $\phi_{\mathrm{e,v}}$ and grid voltage angle ϕ_g, defined as VSM load angle δ_v[8]; whereas the damping feedback $M_{\mathrm{d,v}} := D_\mathrm{v}\dot{\delta}_\mathrm{v}/\omega_{\mathrm{g,R}} :=$

[8]Physically correct (i.e., analogous to SMs) would be $\delta_\mathrm{v} := \phi_{\mathrm{e,v}} - \phi_\mathrm{g} + \frac{\pi}{2}$, but removing the offset $\frac{\pi}{2}$, i.e., $\delta_\mathrm{v} := \phi_{\mathrm{e,v}} - \phi_\mathrm{g}$, leads to the desired grid voltage alignment of the VSM rotor position (see Fig. 3).

$D_\mathrm{v}(\Omega_\mathrm{m,v}-\Omega_\mathrm{g})$ counteracts the deviation between VSM angular velocity $\Omega_\mathrm{m,v}$ and grid angular velocity Ω_g, defined as (normalized) VSM slip $\dot{\delta}_\mathrm{v}/\omega_\mathrm{g,R}$. In general, the VSM eventually achieves turbine torque and grid frequency synchronization, i.e., $M_\mathrm{m,v}=M_\mathrm{t,v}$ and $\Omega_\mathrm{m,v}=\Omega_\mathrm{g}$ for $\dot{\Omega}_\mathrm{g}=0$. In particular, the considered freely spinning VSM with $M_\mathrm{t,v}=0$ also achieves grid angle synchronization, i.e., $\phi_\mathrm{e,v}=\phi_\mathrm{g}$ in steady state. Thus, for the fault-free case with zero RoCoF, i.e., $\frac{\mathrm{d}}{\mathrm{d}t}\omega_\mathrm{g}=0\Rightarrow\delta_\mathrm{v}=0$, the VSM-aligned dq-reference frame with $\phi_\mathrm{p}:=\phi_\mathrm{e,v}=\phi_\mathrm{g}$ corresponds to the grid-voltage-aligned dq-reference frame, as shown in Fig. 3(a). However, for a fault with negative RoCoF, i.e., $\frac{\mathrm{d}}{\mathrm{d}t}\omega_\mathrm{g}<0$, the VSM load angle increases, i.e., $\delta_\mathrm{v}:=\phi_\mathrm{e,v}-\phi_\mathrm{g}>0$, as shown in Fig. 3(b). For existing VSM control without FTC, denoted by primed quantities, the dq'-reference frame is aligned with the rotor current vector $\boldsymbol{i}_\mathrm{r}^{\alpha\beta}$ and the VSM load angle is defined equal to the DFIM load angle, i.e., $\delta_\mathrm{v}':=\phi_\mathrm{e,v}'-\phi_\mathrm{g}'+\frac{\pi}{2}=\phi_{i_\mathrm{r}}^{dq'}-\phi_{u_\mathrm{s}}^{dq'}+\frac{\pi}{2}=:\delta$ with $\phi_{i_\mathrm{r}}^{dq'}=0$.

In the Laplace domain, the VSM inertial response [28]

$$\frac{M_\mathrm{m,v}}{\dot{\Omega}_\mathrm{g}}=\frac{-k_m\omega_\mathrm{g,R}}{s^2+2\zeta_\mathrm{v}\omega_\mathrm{v}s+\omega_\mathrm{v}^2}$$
$$\text{with }\zeta_\mathrm{v}:=\frac{D_\mathrm{v}}{\sqrt{8H_\mathrm{v}k_m\omega_\mathrm{g,R}}},\quad \omega_\mathrm{v}^2:=\frac{k_m\omega_\mathrm{g,R}}{2H_\mathrm{v}} \tag{64}$$

is characterized by VSM damping ratio ζ_v and natural angular velocity ω_v. Note that the final value in (64) given by $s=0\Rightarrow M_\mathrm{m,v}=-2H_\mathrm{v}\dot{\Omega}_\mathrm{g}$ is proportional to the VSM inertia constant H_v. Thus, the higher the H_v, the higher the VSM machine torque and grid frequency support, since the VSM power injection counteracts the RoCoF, see also Fig. 12. Considering the transient behavior of (64), we refer to [28, Fig. 5], which compares the VSM inertial responses for different parameter combinations $(H_\mathrm{v},D_\mathrm{v})$.

To achieve a critical damping ratio $\zeta_\mathrm{v}=1$ without torque or power overshoots, the VSM damping D_v and torque feedback gain k_m should be chosen as follows [28]:

$$\zeta_\mathrm{v}\overset{!}{=}1\overset{(64)}{\Rightarrow}D_\mathrm{v}\overset{!}{=}D_\mathrm{v,crit}:=\sqrt{8H_\mathrm{v}k_m\omega_\mathrm{g,R}} \tag{65}$$

$$k_m:=\frac{\partial M_\mathrm{m,v}}{\partial\delta_\mathrm{v}}:=\frac{\partial M_\mathrm{m}}{\partial\delta}\overset{(15)}{=}-\frac{\kappa_\mathrm{p}n_\mathrm{p}M_\mathrm{s,r}}{m_\mathrm{m,R}X_\mathrm{s}}\widehat{u_\mathrm{s}i_\mathrm{r}}\cos(\delta). \tag{66}$$

Note that a critically damped system as in (65) is neither realistic nor achievable for SMs but desirable for VSMs [18]. For more details about the differences between the inertial response of VSM-controlled DFIMs and that of SMs, see [28, Remark (R.4) and Sec. III-G]. Moreover, but out of scope of this article, an overload protection scheme may manipulate the torque synchronization loop parameters to ensure grid synchronization, see [28, Sec. III-I].

Finally, note that the VSM slip or damping torque $M_\mathrm{d,v}$ in Fig. 6 is often calculated based on the assumption $\Omega_\mathrm{g}=1$ [16], [19], [22], [25], such that D_v can be considered as active power droop gain [12]. However, in general, no power reserves are available for MPPT, such that this assumption leads to nonadmissible droop power for below-rated grid frequency. In this case, the droop power is saturated to zero, which reduces the VSM and power system damping, as explained in more detail later in Section III-F2 and Remark (R.6). Nonetheless, to achieve sufficient damping and to avoid power oscillations during RoCoF events, a VSM damping analogous to the SM damper windings is desirable [18], [19], [20]. Thus, in this article, the assumption $\Omega_\mathrm{g}=1$ is *dropped*. Instead, for the computation of the VSM slip $\dot{\delta}_\mathrm{v}/\omega_\mathrm{g,R}:=\Omega_\mathrm{m,v}-\Omega_\mathrm{g}$, the grid angular velocity Ω_g (in p.u.) for VSM damping is dynamically estimated by[9] [28]

$$\widehat{\Omega}_\mathrm{g}:=\Omega_\mathrm{m,v}-\frac{s}{1+sT_\mathrm{f,v}}\frac{\delta_\mathrm{v}}{\omega_\mathrm{g,R}},\quad \delta_\mathrm{v}:=\phi_\mathrm{e,v}-\phi_{u_\mathrm{s}}^{\alpha\beta} \tag{67}$$

with filter time constant $T_\mathrm{f,v}$ and measured stator voltage angle $\phi_{u_\mathrm{s}}^{\alpha\beta}$. Note that $T_\mathrm{f,v}$ is chosen significantly smaller than a realistic value, which would be necessary to emulate the SM magnetic flux dynamics [18]. However, choosing $T_\mathrm{f,v}$ negligibly small for the inertial response, as in this article, improves the VSM damping [18].

Remark (R.4): *The virtual turbine power is defined as*

$$P_\mathrm{t,v}:=\Omega_\mathrm{m,v}M_\mathrm{t,v}.$$

Analogous to SMs, neglecting any mechanical losses, the VSM mechanical power is defined based on the sum of the electromagnetical torques, i.e.,

$$P_\mathrm{m,v}:=\Omega_\mathrm{m,v}\left(M_\mathrm{m,v}+M_\mathrm{d,v}\right).$$

The VSM damping power $\Omega_\mathrm{m,v}M_\mathrm{d,v}$ only appears in the ("internal") VSM model, i.e., the VSM electrical power is defined as

$$P_\mathrm{el,v}:=\Omega_\mathrm{m,v}M_\mathrm{m,v}\approx\Omega_\mathrm{m,v}\left(M_\mathrm{m}-\overline{M}_\mathrm{m,ref}\right)$$

which is not identical to SMs, where the damping power of the ("external") real damper windings also appears in the electrical (stator) power. For further discussion about so-called internal versus external damping, see [18] and [28].

F. ACTIVE POWER CONTROL

The active power at the PCC $p_\mathrm{pcc}:=p_\mathrm{s}+p_\mathrm{g}\approx p_\mathrm{m}$ depends on the DFIM power $p_\mathrm{m}=\omega_\mathrm{m}m_\mathrm{m}\approx p_\mathrm{s}+p_\mathrm{r}$, i.e., the stator power p_s flows directly to the PCC, whereas the rotor power $p_\mathrm{r}\approx p_\mathrm{g}$ flows via the back-to-back inverter with $LC(L)$-filter to the PCC, see Fig. 1 and [15]. Thus, the active power control is based on controlling the DFIM torque m_m. The FTC and the active power droop control with its saturation for overload protection are discussed in the following.

[9] In addition to the filtering in (67), a rate limiter is implemented analogously to (32), which limits the magnitude of the estimated grid angular velocity time derivative $\max\{|\frac{\mathrm{d}}{\mathrm{d}t}\widehat{\Omega}_\mathrm{g}|\}$ to $\widehat{A}_\mathrm{g,max}:=2\frac{\%}{\mathrm{s}}$, see [2, Table X]. This limit corresponds to the maximum or worst-case RoCoF before facing a black-out due to disconnection of SMs [4], [10].

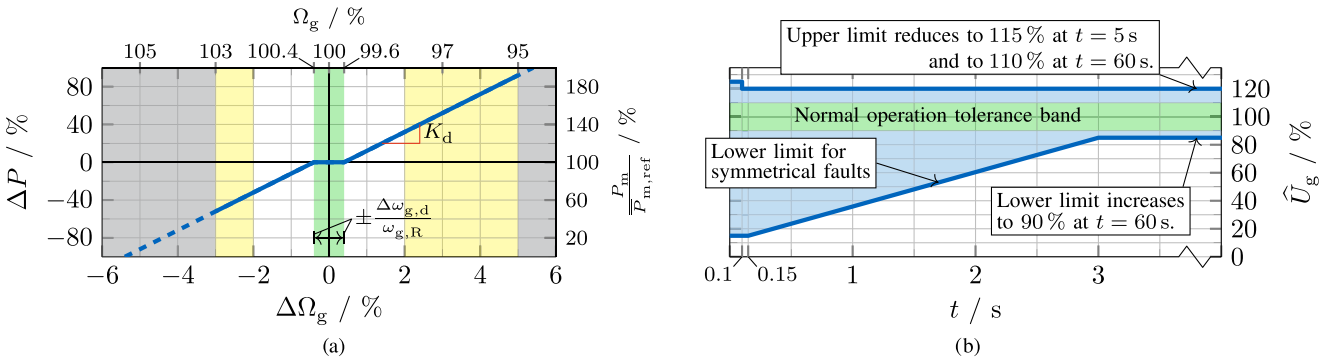

FIGURE 7. Illustration of German grid codes [36] with normal operation tolerance band [ ]. (a) Active power droop curve, as in (69), with extended admissible frequency range [ ], see also (R.5). (b) (Extended) Admissible voltage range [ ] with lower and upper fault-ride-through-curves [——], see also Remark (R.8).

1) FEEDFORWARD TORQUE CONTROL

Assuming a grid-voltage-aligned dq-reference frame, the DFIM torque only depends on the d-component of the DFIM rotor current, recall (14), i.e., the FTC is given by

$$\boldsymbol{u}_{\mathrm{s}}^{dq} = \begin{pmatrix} \widehat{u}_{\mathrm{s}} \\ 0 \end{pmatrix} = \begin{pmatrix} \widehat{u}_{\mathrm{g}} \\ 0 \end{pmatrix} \overset{(14)}{\Rightarrow} i_{\mathrm{r,ref}}^{d} := \frac{-X_{\mathrm{s}}}{\kappa_{\mathrm{p}} n_{\mathrm{p}} M_{\mathrm{s,r}} \widehat{u}_{\mathrm{s}}} \overline{m}_{\mathrm{m,ref}} \tag{68}$$

with saturated torque reference $\overline{m}_{\mathrm{m,ref}}$ from (40), see Fig. 4.

2) DROOP CONTROL

The strategy is to primarily use the WS kinetic energy for inertia emulation, whereas droop control is only activated if additional energy reserves are available due to RPPT (instead of MPPT). This improves the WS stability (less severe WT speed nadir in Fig. 13) without degrading the grid support, as shown in the results later in Section IV-E2. If wind power reserves are available, i.e., for $P_{\mathrm{m,ref,rel}} < 1$ in (34), the WS has to provide droop power outside the tolerance band $\omega_{\mathrm{g,R}} \pm \Delta\omega_{\mathrm{g,d}}$ with rated grid angular velocity $\omega_{\mathrm{g,R}}$ and tolerated grid angular velocity deviation $\pm\Delta\omega_{\mathrm{g,d}}$ [36]. In Fig. 7(a), with droop gain k_{d} (see [2, Table X]) or normalized droop gain $K_{\mathrm{d}} := k_{\mathrm{d}}\omega_{\mathrm{g,R}}$, the desired power change $\Delta P := (P_{\mathrm{m}} - \overline{P}_{\mathrm{m,ref}})/\overline{P}_{\mathrm{m,ref}}$, relative to the power at rated grid frequency $P_{\mathrm{m}}|_{\omega_{\mathrm{g}}=\omega_{\mathrm{g,R}}} = \overline{P}_{\mathrm{m,ref}}$ in (40), is given by [36]

$$\Delta P := \begin{cases} k_{\mathrm{d}} \left(\Delta\widehat{\omega}_{\mathrm{g}} \pm \Delta\omega_{\mathrm{g,d}}\right), & \text{for } \Delta\widehat{\omega}_{\mathrm{g}} \lessgtr \mp\Delta\omega_{\mathrm{g,d}}, \\ 0, & \text{otherwise}, \end{cases} \tag{69}$$

where the estimated grid angular velocity deviation $\Delta\widehat{\omega}_{\mathrm{g}}$ is based on the VSM angular velocity $\omega_{\mathrm{m,v}}$, i.e., $\Delta\widehat{\omega}_{\mathrm{g}} := \omega_{\mathrm{g,R}} - n_{\mathrm{p}}\omega_{\mathrm{m,v}} \approx \omega_{\mathrm{g,R}} - \omega_{\mathrm{g}}$. This is similar to the speed governor of real SMs [37, Sec. 2.3.3], see also (102).

Remark (R.5): *In [36], the power system state is defined as critical if the grid angular velocity leaves its tolerance band $\omega_{\mathrm{g,R}} \pm \Delta\omega_{\mathrm{g}}$ with $\omega_{\mathrm{g,R}} := 2\pi 50\ \frac{rad}{s}$ and $\Delta\omega_{\mathrm{g}} := 2\pi 0.2\ \frac{rad}{s}$, which corresponds to a relative tolerance of $\Delta\Omega_{\mathrm{g}} := \frac{\Delta\omega_{\mathrm{g}}}{\omega_{\mathrm{g,R}}} = 0.4\%$ (see tolerance band [ ] in Fig. 7(a) or in subplot 10 of Fig. 16). Outside the tolerance band, GUs have to support the grid frequency if feasible. Moreover, GUs have to stay grid-connected within the range $2\pi 49\frac{rad}{s} \le \omega_{\mathrm{g}} \le 2\pi 51\frac{rad}{s}$ or $98\% \le \Omega_{\mathrm{g}} \le 102\%$, and, for a limited time interval of up to 30 min, GUs have to stay grid-connected within the extended range $2\pi 47.5\frac{rad}{s} \le \omega_{\mathrm{g}} \le 2\pi 51.5\frac{rad}{s}$ or $95\% \le \Omega_{\mathrm{g}} \le 103\%$, see [ ] in Fig. 7(a).*[10]

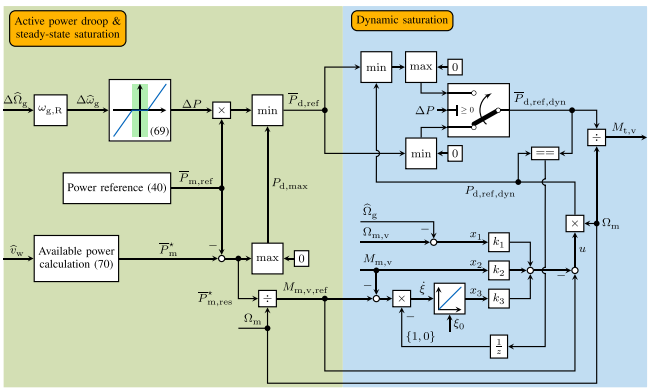

FIGURE 8. Active power droop control with overload protection.

In Fig. 8, the DFIM power reserve $\overline{P}^{\star}_{\mathrm{m,res}}$ is the difference between available $\overline{P}^{\star}_{\mathrm{m}}$ and reference $\overline{P}_{\mathrm{m,ref}}$ DFIM power, leading to the maximum droop power $P_{\mathrm{d,max}}$ as follows:

$$\overline{P}^{\star}_{\mathrm{m,res}} := \overline{P}^{\star}_{\mathrm{m}} - \overline{P}_{\mathrm{m,ref}} \overset{(35)}{\underset{(40)}{:=}} \mathrm{sat}_{0}^{P_{\mathrm{mppt}}(\Omega_{\mathrm{m}})} \overline{P}^{\star}_{\mathrm{t}}(\widehat{v}_{\mathrm{w}}) - \Omega_{\mathrm{m}}\overline{M}_{\mathrm{m,ref}}$$

$$\Rightarrow \quad P_{\mathrm{d,max}} := \max\left\{\overline{P}^{\star}_{\mathrm{m,res}}, 0\right\} \tag{70}$$

where the lower saturation ensures $P_{\mathrm{d,max}} \ge 0$, especially for $\Omega_{\mathrm{m},H0} > \Omega_{\mathrm{m}}$, since $\overline{M}_{\mathrm{m,ref}}$ depends on $\Omega_{\mathrm{m},H0}$, see (37). The steady-state droop power reference $\overline{P}_{\mathrm{d,ref}}$ is saturated by

[10] Besides, there are further requirements during transients, e.g., above the upper limit of 51.5 Hz, GUs have to be capable of staying grid-connected for at least further 5 s [36].

$P_{\mathrm{d,max}}$ to ensure steady-state overload protection, i.e.,

$$\overline{P}_{\mathrm{d,ref}} \overset{(69)}{\underset{(70)}{:=}} \min\left\{\overline{P}_{\mathrm{m,ref}}\Delta P,\, P_{\mathrm{d,max}}\right\}. \tag{71}$$

The droop power reference $\overline{P}_{\mathrm{d,ref}}$ in (71) adjusts the VSM turbine torque $M_{\mathrm{t,v}}$ (see Fig. 8 without dynamic saturation) like the speed governor of a real SM adjusts its turbine power. However, the real (steam) turbine dynamics introduce delays in the range of seconds [37, Sec. 2.3.3.7], as modeled later by T_{gov} in (103), such that the VSM droop control is significantly faster (in the range of milliseconds) than the SM droop control. The impact of the slow SM droop control on its fast inertial response is rather negligible. This is different for VSMs: For a negative RoCoF, in addition to the VSM inertial power response, the droop control may further increase the DFIM power P_{m}, which may then temporarily exceed the available active power, i.e., $P_{\mathrm{m}} > \overline{P}^{\star}_{\mathrm{m}}$, as shown in the results later in Section IV-E2. In the worst case, this leads to inadmissible power overshoots or WT deceleration. Thus, in addition to the *steady state saturation (ssDS) in (71)*, a *dynamic droop saturation* (dyDS) is proposed in the following.

3) DYNAMIC DROOP SATURATION

Taking power reference deviations $\overline{P}_{\mathrm{m,ref}} - P_{\mathrm{m}} \neq 0$ due to inertia emulation during RoCoF events into account, an additional control loop is required to limit the droop power to the available power reserve. A PI controller with anti-windup could be designed, similar to the overload mitigation controller for GFM inverters proposed in [21], but this article proposes state feedback control in the following.

Dividing the available DFIM power reserve at the MPP $\overline{P}^{\star}_{\mathrm{m,res}} := \overline{P}^{\star}_{\mathrm{m}} - \overline{P}_{\mathrm{m,ref}}$ by the DFIM angular velocity Ω_{m} yields the corresponding DFIM torque reserve or VSM torque reference $M_{\mathrm{m,v,ref}} := \overline{P}^{\star}_{\mathrm{m,res}}/\Omega_{\mathrm{m}}$, see Fig. 8. The (small-signal) response of the DFIM power P_{m} to changes in the (dynamic reference) droop power $\overline{P}_{\mathrm{d,ref,dyn}}$ is given by the (small-signal) response of the VSM torque $M_{\mathrm{m,v}}$ to changes in the virtual turbine torque $M_{\mathrm{t,v}}$, i.e.,

$$\frac{P_{\mathrm{m}}(s)}{\overline{P}_{\mathrm{d,ref,dyn}}(s)} = \frac{\Omega_{\mathrm{m}}\, M_{\mathrm{m,v}}(s)}{\Omega_{\mathrm{m}}\, M_{\mathrm{t,v}}(s)} = \frac{M_{\mathrm{m,v}}(s)}{M_{\mathrm{t,v}}(s)}. \tag{72}$$

which, in view of Fig. 6, can be derived as follows:

$$s\Delta\Omega_{\mathrm{m,v}} = \frac{1}{2H_{\mathrm{v}}}\left(M_{\mathrm{t,v}} - M_{\mathrm{m,v}} - D_{\mathrm{v}}\Delta\Omega_{\mathrm{m,v}}\right) \tag{73}$$

$$sM_{\mathrm{m,v}} = k_m\omega_{\mathrm{g,R}}\Delta\Omega_{\mathrm{m,v}} \tag{74}$$

$$\Rightarrow \frac{M_{\mathrm{m,v}}(s)}{M_{\mathrm{t,v}}(s)} = \frac{\omega_{\mathrm{v}}^2}{s^2 + 2\zeta_{\mathrm{v}}\omega_{\mathrm{v}}s + \omega_{\mathrm{v}}^2} \tag{75}$$

with $\Delta\Omega_{\mathrm{m,v}} := \Omega_{\mathrm{m,v}} - \Omega_{\mathrm{g}}$ and ζ_{v}, ω_{v} as in (64). With an additional integral state $\frac{\mathrm{d}}{\mathrm{d}t}\xi := M_{\mathrm{m,v}} - M_{\mathrm{m,v,ref}}$ to achieve steady-state accuracy, the controlled state-space dynamics are given by

$$\boldsymbol{x} := \begin{pmatrix}\Delta\Omega_{\mathrm{m,v}}\\ M_{\mathrm{m,v}}\\ \xi\end{pmatrix} \overset{(73)}{\underset{(74)}{\Rightarrow}} \dot{\boldsymbol{x}} = \boldsymbol{A}\boldsymbol{x} + \boldsymbol{b}u - \boldsymbol{v} \tag{76}$$

$$y := M_{\mathrm{m,v}} = \boldsymbol{c}^{\top}\boldsymbol{x} := \begin{pmatrix}0 & 1 & 0\end{pmatrix}\boldsymbol{x}, \quad y_{\mathrm{ref}} := M_{\mathrm{m,v,ref}} \tag{77}$$

$$\boldsymbol{A} := \begin{bmatrix}-\frac{D_{\mathrm{v}}}{2H_{\mathrm{v}}} & -\frac{1}{2H_{\mathrm{v}}} & 0\\ k_m\omega_{\mathrm{g,R}} & 0 & 0\\ 0 & 1 & 0\end{bmatrix}, \boldsymbol{b} := \begin{pmatrix}\frac{1}{2H_{\mathrm{v}}}\\ 0\\ 0\end{pmatrix}, \boldsymbol{v} := \begin{pmatrix}0\\ 0\\ y_{\mathrm{ref}}\end{pmatrix}$$

$$u := M_{\mathrm{t,v}} := y_{\mathrm{ref}} - \boldsymbol{k}^{\top}\boldsymbol{x} := y_{\mathrm{ref}} - \begin{pmatrix}k_1 & k_2 & k_3\end{pmatrix}\boldsymbol{x}$$

using the VSM slip approximation $\Delta\Omega_{\mathrm{m,v}} \approx \Omega_{\mathrm{m,v}} - \widehat{\Omega}_{\mathrm{g}}$ with $\widehat{\Omega}_{\mathrm{g}}$ in (67). Comparing the closed-loop characteristic polynomial $\det(\boldsymbol{A} - \boldsymbol{b}\boldsymbol{k}^{\top} - \lambda\boldsymbol{I})$ to the desired third-order polynomial (23) leads to the state feedback gain vector[11]

$$\boldsymbol{k} = \begin{pmatrix}k_1\\ k_2\\ k_3\end{pmatrix} = \begin{pmatrix}2H_{\mathrm{v}}\left(\frac{1}{T_{\mathrm{w}}} + 2\zeta\omega\right) - \zeta_{\mathrm{v}}\\ \frac{2H_{\mathrm{v}}}{k_m\omega_{\mathrm{g,R}}}\left(\omega^2 + \frac{2\zeta\omega}{T_{\mathrm{w}}}\right) - 1\\ \frac{2H_{\mathrm{v}}}{k_m\omega_{\mathrm{g,R}}}\frac{\omega^2}{T_{\mathrm{w}}}\end{pmatrix} \tag{78}$$

with tuning parameters ζ, ω, and T_{w}, see [2, Table X]. Reference tracking with steady-state accuracy is achieved, i.e.,

$$\dot{\boldsymbol{x}} = 0 \overset{(76)}{\Rightarrow} \begin{pmatrix}\Delta\Omega_{\mathrm{m,v}}\\ M_{\mathrm{m,v}}\\ \xi\end{pmatrix} = \begin{pmatrix}0\\ M_{\mathrm{m,v,ref}}\\ -\frac{k_2}{k_3}M_{\mathrm{m,v,ref}}\end{pmatrix} \overset{(77)}{\Rightarrow} y = y_{\mathrm{ref}}. \tag{79}$$

In the dynamic saturation part of Fig. 8, the first (upper) min-saturation block with input $\overline{P}_{\mathrm{d,ref}}$ ensures that the final (dynamically saturated) droop reference $\overline{P}_{\mathrm{d,ref,dyn}}$ equals the (steady-state saturated) droop reference $\overline{P}_{\mathrm{d,ref}}$ if enough power reserves are available. Moreover, the switching block in Fig. 8 and its neighboring min/max-saturation blocks ensure the correct sign of $\overline{P}_{\mathrm{d,ref,dyn}}$, e.g., to avoid that the droop control counteracts the inertia emulation. The integral state ξ is reset to its steady-state value in (79) if inertia emulation is inactive in (30). For details of the anti-windup strategy in Fig. 8, see [28, Sec. III-G3] and [1, Sec. 10.4.1].

Concluding, two droop saturation variants are considered, namely ssDS and ss/dyDS, i.e., the VSM turbine torque, equal to the droop reference, is given by[12]

$$M_{\mathrm{t,v}} := M_{\mathrm{d,ref}} = \begin{Bmatrix}:= \overline{P}_{\mathrm{d,ref}}/\Omega_{\mathrm{m}}, & \text{for ssDS,}\\ := \overline{P}_{\mathrm{d,ref,dyn}}/\Omega_{\mathrm{m}}, & \text{for ss/dyDS.}\end{Bmatrix} \tag{80}$$

Remark (R.6): *Active droop control with $M_{\mathrm{t,v}} \neq 0$ changes the equilibrium of the torque synchronization loop, see Fig. 4, such that the VSM is not freely spinning anymore as previously assumed in Section III-E and Figs. 3(a) and 6. The phasor*

[11] The states $\Delta\Omega_{\mathrm{m,v}}$ and $M_{\mathrm{m,v}}$ are filtered by first-order lag systems with time constants $T_{\mathrm{f},\Delta}$ and $T_{\mathrm{f,mv}}$ for the state feedback, see [2, Table X].

[12] Alternatively, the droop control may adjust $\overline{m}_{\mathrm{m,ref}}$ in (68) but this is avoided due to the FTC inaccuracy during RoCoF events, see Section IV.

diagram of the now nonfreely spinning VSM in Fig. 3(b) shows that the d-axis is not aligned with the grid (stator) voltage anymore. Moreover, in addition to the VSM damping loop with damping gain D_v, the active droop control loop with droop gain k_d dampens the VSM inertial response (see Fig. 4 and [20]). Thus, the assumption of inactive droop control leads to a worst-case analysis with minimal damping in Section III-E, i.e., the proposed damping gain adaption in (65) and (66) achieves at least a critically damped system, which is crucial and beneficial for grid stability (shown in the results later), see also [17], [18], [19], and [20]. However, choosing a high droop gain k_d increases the risk of load angle instability, i.e., the VSM or DFIM may loose synchronism during RoCoFs [20]. The proposed dyDS (see Fig. 8) helps to decrease this risk by reducing the droop power to the available power reserves. Besides, choosing a high VSM inertia constant H_v also increases the risk of load angle stability, but the protection method in [28] reduces H_v if necessary, and adapts D_v accordingly as in (65).

G. REACTIVE POWER CONTROL

The reactive power at the PCC $q_{pcc} := q_s + q_g$ depends on the reactive power of both, DFIM stator and grid-side filter, see Fig. 1. The grid voltage control is based on feedforward reactive power control of both, as discussed in the following.

1) FEEDFORWARD STATOR REACTIVE POWER CONTROL

With the DFIM stator reactive power given by

$$q_s = \kappa_p (\boldsymbol{u}_s^{dq})^\top \boldsymbol{J} \boldsymbol{i}_s^{dq} \overset{(12)}{=} \kappa_p \frac{(\widehat{u}_s)^2}{X_s} + \kappa_p \frac{X_{s,r}}{X_s} \widehat{u}_s i_r^q \tag{81}$$

$$= \kappa_p \frac{(\widehat{u}_s)^2}{X_s} - \kappa_p \frac{X_{s,r}}{X_s} \widehat{u}_s \widehat{\imath}_r \cos(\delta) \tag{82}$$

assuming $\boldsymbol{u}_s^{dq} = (\widehat{u}_s, 0)^\top$, the rotor q-current reference

$$\overset{(81)}{\Rightarrow} \quad i_{r,ref}^q := \frac{X_s}{\kappa_p X_{s,r} \widehat{u}_s} q_{s,ref} - \frac{\widehat{u}_s}{X_{s,r}} \tag{83}$$

$$\text{should fulfill } (i_{ref}^q)^2 \le \sqrt{(\widehat{\imath}_{r,R})^2 - (i_{r,ref}^d)^2} \tag{84}$$

with rotor current limit/rating $\widehat{\imath}_{r,R}$, assuming $|i_{r,ref}^d| \le \widehat{\imath}_{r,R}$. Moreover, with $X_s := \omega_p L_s$, $X_{s,r} := \omega_p M_{s,r}$ and

$$\boldsymbol{Y} \overset{(11)}{=} \begin{bmatrix} R_s & -X_s \\ X_s & R_s \end{bmatrix}^{-1} \Rightarrow \boldsymbol{Y}^\top \boldsymbol{Y} = \frac{1}{R_s^2 + X_s^2} \boldsymbol{I}_2 =: \frac{1}{Z_s^2} \boldsymbol{I}_2 \tag{85}$$

the admissible range for $i_{r,ref}^q$ induced by the stator current limit/rating $\widehat{\imath}_{s,R}$ is given by $(\widehat{\imath}_{s,R})^2 \ge (\boldsymbol{i}_s^{dq})^\top \boldsymbol{i}_s^{dq}$

$$\underset{(85)}{\overset{(11)}{\Rightarrow}} \quad (\widehat{\imath}_{s,R})^2 \ge \left(\boldsymbol{u}_s^{dq} - \boldsymbol{J} X_{s,r} \boldsymbol{i}_r^{dq}\right)^\top \left(\boldsymbol{u}_s^{dq} - \boldsymbol{J} X_{s,r} \boldsymbol{i}_r^{dq}\right) / Z_s^2$$

$$\Rightarrow \quad i_{r,ref}^q \lessgtr \frac{1}{X_{s,r}} \left(\pm \sqrt{Z_s^2 (\widehat{\imath}_{s,R})^2 - \left(X_{s,r} i_r^d\right)^2} - \widehat{u}_s \right) \tag{86}$$

with $i_r^d = i_{r,ref}^d$, assuming $\boldsymbol{u}_s^{dq} = (\widehat{u}_s, 0)^\top$.

2) FEEDFORWARD FILTER REACTIVE POWER CONTROL

In Fig. 1, for $\frac{d}{dt} \boldsymbol{u}_c^{dq} = \boldsymbol{0}_2$, the filter capacitor current is

$$\boldsymbol{i}_c^{dq} = (\boldsymbol{Z}_c^{dq})^{-1} \boldsymbol{u}_g^{dq}, \ \boldsymbol{Z}_c^{dq} := R_c \boldsymbol{I}_2 - \boldsymbol{J} X_c, \ X_c := \frac{1}{\omega_p C_c}. \tag{87}$$

The filter q-current reference $i_{f,ref}^q$ to track the grid-side filter reactive power reference $q_{g,ref}$ is given by

$$q_g = \kappa_p (\boldsymbol{u}_g^{dq})^\top \boldsymbol{J} \boldsymbol{i}_g^{dq} \overset{(87)}{=} -\kappa_p \widehat{u}_g i_f^q - \kappa_p \frac{X_c}{Z_c^2} (\widehat{u}_g)^2 \tag{88}$$

$$\Rightarrow \quad i_{f,ref}^q := -\frac{q_{g,ref}}{\kappa_p \widehat{u}_g} - \frac{X_c}{Z_c^2} \widehat{u}_g \tag{89}$$

using $\boldsymbol{i}_g^{dq} = \boldsymbol{i}_f^{dq} + \boldsymbol{i}_c^{dq}$ and assuming $\boldsymbol{u}_g^{dq} = (\widehat{u}_g, 0)^\top$.

3) GRID VOLTAGE CONTROL

a) Grid voltage control with FTC: The stator (or grid) voltage amplitude $\widehat{u}_s$ is controlled by

$$q_{pcc,ref} := q_{s,ref} + q_{g,ref} := k_p \left(\widehat{u}_{s,ref} - \widehat{u}_s\right) + k_i \overline{\xi} \tag{90}$$

with stator voltage amplitude reference/rating $\widehat{u}_{s,ref} := \widehat{u}_{s,R}$, PCC reactive power reference $q_{pcc,ref}$, PI gains k_p and k_i, and saturated integral state $\overline{\xi}$. Taking the WS reactive power limitations into account, the output saturation and the anti-windup for the PI control in (90) are given by[13]

$$\overline{q}_{pcc,ref} := \mathrm{sat}_{q_{pcc,min}}^{q_{pcc,max}} \left(q_{pcc,ref}\right)$$

$$\Rightarrow \ \frac{d}{dt} \xi := f_{aw}(q_{pcc,ref}, q_{pcc,min}, q_{pcc,max}) \left(\widehat{u}_{s,ref} - \widehat{u}_s\right)$$

$$f_{aw}(r, a, b) := \begin{cases} 0, & \text{if } r < a \vee r > b, \\ 1, & \text{otherwise.} \end{cases} \tag{91}$$

with the (unsaturated) integral state ξ and the anti-windup function f_{aw}, which stops the integration if necessary. Especially, due to the dependency of the dc-link voltage on the d-current or active power control, the latter is prioritized over the reactive power control. Thus, $q_{pcc,min}$ and $q_{pcc,max}$ depend on the d-current references, which vary over time. Extending the anti-windup strategy (91) accordingly, the saturated integral state in (90) is selected by[14]

$$\overline{\xi} := \begin{cases} \frac{1}{k_i} q_{pcc,min}, & \text{if } \ k_i \xi < q_{pcc,min}, \\ \frac{1}{k_i} q_{pcc,max}, & \text{if } k_i \xi > q_{pcc,max}, \\ \xi, \ \xi_0 = \overline{\xi}[k-1], & \text{otherwise, with } \frac{d}{dt} \xi \text{ in (91).} \end{cases} \tag{92}$$

There is a degree of freedom for choosing the reactive power share between the DFIM stator and grid-side filter in (90). The strategy, proposed in the following, maximizes the

[13] For inactive q-current saturation, the min./max. reactive power limit for anti-windup in (91)–(92) is set to $q_{pcc,min\,/\,max} := \mp\infty$. For active q-current saturation, i.e., for $i_{r,ref,sat}^q \ne i_{r,ref}^q$ in (94) and $i_{f,ref,sat}^q \ne i_{f,ref}^q$ in (99), the corresponding reactive power limit is adapted based on the saturated reactive power reference at the last sample step, i.e., $q_{pcc,min\,/\,max} := q_{s,ref,sat}[k-1] + q_{g,ref,sat}[k-1]$ given by (95) and (100).

[14] The initial value $\xi_0 = \overline{\xi}[k-1]$ after (re)activation is given by the saturation output $\overline{\xi}$ at the last sample step $k-1$, or by zero for $k = t = 0$.

rotor current amplitude or minimizes i_{r}^{q}, q_{s} in (81) for maximal VSM stability margin (max. overexcitation) [28], i.e.,

$$i_{\mathrm{f}}^{q} \stackrel{!}{=} i_{\mathrm{f,min}}^{q} := -\sqrt{(\widehat{\imath}_{\mathrm{f,max}})^2 - (i_{\mathrm{f,ref}}^{d})^2} \tag{93}$$

$$\stackrel{(88)}{\Rightarrow} \quad q_{\mathrm{g,ref}} := -\kappa_{\mathrm{p}} \widehat{u}_{\mathrm{s}} i_{\mathrm{f,min}}^{q} - \kappa_{\mathrm{p}} \frac{X_{\mathrm{c}}}{Z_{\mathrm{c}}^2} (\widehat{u}_{\mathrm{s}})^2$$

$$\stackrel{(90)}{\Rightarrow} \quad q_{\mathrm{s,ref}} := q_{\mathrm{pcc,ref}} - q_{\mathrm{g,ref}}$$

$$\stackrel{(83)}{\Rightarrow} \quad i_{\mathrm{r,ref}}^{q} := \frac{X_{\mathrm{s}}}{\kappa_{\mathrm{p}} X_{\mathrm{s,r}} \widehat{u}_{\mathrm{s}}} q_{\mathrm{s,ref}} - \frac{\widehat{u}_{\mathrm{s}}}{X_{\mathrm{s,r}}}$$

$$\Rightarrow \quad i_{\mathrm{r,ref,sat}}^{q} := \mathrm{sat}_{i_{\mathrm{r,min}}^{q}}^{i_{\mathrm{r,max}}^{q}} \left\{ i_{\mathrm{r,ref}}^{q} \right\} \tag{94}$$

$$\stackrel{(81)}{\Rightarrow} \quad q_{\mathrm{s,ref,sat}} := \kappa_{\mathrm{p}} \frac{(\widehat{u}_{\mathrm{s}})^2}{X_{\mathrm{s}}} + \kappa_{\mathrm{p}} \frac{X_{\mathrm{s,r}}}{X_{\mathrm{s}}} \widehat{u}_{\mathrm{s}} i_{\mathrm{r,ref,sat}}^{q} \tag{95}$$

with maximal GSI or filter current amplitude $\widehat{\imath}_{\mathrm{f,max}}$ and with

$$i_{\mathrm{r,min}}^{q} \stackrel{(84)}{\stackrel{:=}{(86)}} \max \left\{ \begin{array}{c} -\sqrt{(\widehat{\imath}_{\mathrm{r,R}})^2 - (i_{\mathrm{r}}^{d})^2}, \\ \frac{-1}{X_{\mathrm{s,r}}} \left(\sqrt{Z_{\mathrm{s}}^2 (\widehat{\imath}_{\mathrm{s,R}})^2 - \left(X_{\mathrm{s,r}} i_{\mathrm{r}}^{d} \right)^2} + \widehat{u}_{\mathrm{s}} \right), \end{array} \right\} \tag{96}$$

with $i_{\mathrm{r}}^{d} = i_{\mathrm{r,ref}}^{d}$. The lower/upper saturation limit $i_{\mathrm{r,min/max}}^{q}$ in (94) depends on $\widehat{\imath}_{\mathrm{r,R}}$ and $\widehat{\imath}_{\mathrm{s,R}}$, see (96), but $i_{\mathrm{r,max}}^{q}$ also depends on additional parameters to ensure load angle stability, see [2, Table X]: the minimum excitation level, specified by $\widehat{I}_{\mathrm{r,min}}$, and the maximum load angle $\delta_{\max}$, resulting in a lower limit for $\phi_{i_{\mathrm{r}}}^{dq}$ in (15). The details are out of scope of this article.

Clearly, the proposed strategy is based on the desired condition $i_{\mathrm{f}}^{q} = i_{\mathrm{f,min}}^{q}$ in (93). However, taking the saturation (94) and (95) into account, $q_{\mathrm{g,ref}}$ and $i_{\mathrm{f,ref}}^{q}$ have to be recalculated after this saturation to fulfill the overall WS reactive power demand $q_{\mathrm{pcc,ref}}$ in (90) if possible, i.e.,

$$\stackrel{(90)}{\stackrel{\Rightarrow}{(95)}} \quad q_{\mathrm{g,ref}} := q_{\mathrm{pcc,ref}} - q_{\mathrm{s,ref,sat}} \tag{97}$$

$$\stackrel{(89)}{\Rightarrow} \quad i_{\mathrm{f,ref}}^{q} := -\frac{q_{\mathrm{g,ref}}}{\kappa_{\mathrm{p}} \widehat{u}_{\mathrm{g}}} - \frac{X_{\mathrm{c}}}{Z_{\mathrm{c}}^2} \widehat{u}_{\mathrm{g}}. \tag{98}$$

Finally, the saturated references for the filter q-current and the grid-side filter reactive power are obtained as

$$\stackrel{(93)}{\stackrel{\Rightarrow}{(98)}} \quad i_{\mathrm{f,ref,sat}}^{q} := \mathrm{sat}_{i_{\mathrm{f,min}}^{q}}^{|i_{\mathrm{f,min}}^{q}|} \left(i_{\mathrm{f,ref}}^{q} \right) \tag{99}$$

$$\stackrel{(88)}{\Rightarrow} \quad q_{\mathrm{g,ref,sat}} := -\kappa_{\mathrm{p}} \widehat{u}_{\mathrm{s}} i_{\mathrm{f,ref,sat}}^{q} - \kappa_{\mathrm{p}} \frac{X_{\mathrm{c}}}{Z_{\mathrm{c}}^2} (\widehat{u}_{\mathrm{s}})^2. \tag{100}$$

Note that the WS reactive (inductive) power increases with i_{r}^{q} but decreases with i_{f}^{q}, see (81) and (88). It follows that, for $i_{\mathrm{r,ref}}^{q} > i_{\mathrm{r,max}}^{q}$ in (94), the WS cannot provide more reactive power, since the GSI is already at its limit $i_{\mathrm{f,ref}}^{q} = i_{\mathrm{f,min}}^{q}$, see (93); whereas, for $i_{\mathrm{r,ref}}^{q} < i_{\mathrm{r,min}}^{q}$ in (94), the grid voltage control decreases $q_{\mathrm{g,ref}}$ by increasing $i_{\mathrm{f,ref}}^{q}$ to fulfill the overall WS reactive power demand $q_{\mathrm{pcc,ref}}$, before reaching the upper limit $i_{\mathrm{f,ref}}^{q} = |i_{\mathrm{f,min}}^{q}|$, see (97)–(100).

Remark (R.7): *The saturation of the grid voltage control output $i_{\mathrm{f},ref}^{q}$ depends on the dc-link voltage control output $i_{\mathrm{f},ref}^{d}$, see (93), (99), or Fig. 4. Moreover, both components of $\boldsymbol{i}_{\mathrm{f},ref}^{dq}$ depend on $\widehat{u}_{\mathrm{g}} = \widehat{u}_{\mathrm{s}}$, see (58) and (90). Thus, active saturation may lead to undesired control interaction, e.g., u_{dc} changes may lead to changes of $i_{\mathrm{f},ref}^{d}$, $i_{\mathrm{f},ref}^{q}$ and finally of $\widehat{u}_{\mathrm{g}}$. To avoid a destabilizing feedback loop $\Delta u_{dc} \Rightarrow \Delta i_{\mathrm{f},ref}^{d} \Rightarrow \Delta i_{\mathrm{f},ref}^{q} \Rightarrow \Delta \widehat{u}_{\mathrm{g}} \Rightarrow \Delta u_{dc}$, the grid voltage control uses nonaggressively tuned PI gains in (90) as in [12] and input filters for $\widehat{u}_{\mathrm{s}}$, $i_{\mathrm{f},ref}^{d}$, and $i_{\mathrm{r},ref}^{d}$. For more details, see [2, (R.11)].*

b) Grid voltage control without FTC (for comparison): Existing VSM control methods without FTC are considered in the following, which change the rotor current (or magnetic flux) amplitude to control the grid voltage, see e.g., [16], [20], [27], and [29]. Clearly, for small load angles $\delta \approx 0$ in Fig. 3(a) or (82), the linear relation $i_{\mathrm{r}}^{q} \approx -\widehat{\imath}_{\mathrm{r}} \Rightarrow \Delta q_{\mathrm{s}} \propto -\Delta \widehat{\imath}_{\mathrm{r}}$ holds. However, for high δ, the function $i_{\mathrm{r}}^{q} = -\widehat{\imath}_{\mathrm{r}} \cos(\delta)$ is nonlinear. Thus, for a fair comparison between (i) VSM control with FTC and (ii) VSM control without FTC, the latter variant uses voltage control with the nonlinear compensation (101) as discussed in the following.[15]

Similar to the dq-reference frame, the dq'-reference frame for VSM control without FTC (denoted by primed quantities) is aligned with the VSM rotor position; but, choosing $\boldsymbol{i}_{\mathrm{r,ref}}^{dq'} := (\widehat{\imath}_{\mathrm{r,ref}},\ 0)^{\top}$ with rotor current amplitude reference $\widehat{\imath}_{\mathrm{r,ref}}$, the rotor current vector is always aligned with the VSM rotor position, i.e., $\phi_{\mathrm{p}}' := \phi_{\mathrm{e,v}}' = \phi_{i_{\mathrm{r}}}^{\alpha\beta}$ in Fig. 3(b). Defining the VSM load angle as $\delta_{\mathrm{v}}' := \phi_{\mathrm{e,v}}' + \frac{\pi}{2} - \phi_{\mathrm{g}} = \phi_{i_{\mathrm{r}}}^{dq'} + \frac{\pi}{2} - \phi_{u_{\mathrm{s}}}^{dq'}$ with $\phi_{i_{\mathrm{r}}}^{dq'} = 0$, the VSM and DFIM load angle are equal, i.e., $\delta_{\mathrm{v}}' = \delta$. Thus, without FTC, only the VSM torque synchronization loop controls the DFIM load angle $\delta = \delta_{\mathrm{v}}'$, whereas, with FTC, $\delta \neq \delta_{\mathrm{v}}$ holds in general.[16]

Again, the grid voltage PI control (90) is used, but with the following input/output modifications. (i) The FTC outputs' zero, i.e., $i_{\mathrm{r}}^{d} = i_{\mathrm{r,ref}}^{d} = 0$ is the input for the saturation of $i_{\mathrm{r,ref,sat}}^{q}$ in (94) and (96), and (ii) the voltage control output $i_{\mathrm{r,ref,sat}}^{q}$ is transformed into a rotor current vector $\boldsymbol{i}_{\mathrm{r}}^{dq}$ with equal q-component and aligned with the VSM rotor or d'-axis, i.e., the final rotor current reference vector in the dq'-reference frame is given by (see also Fig. 3)

$$\boldsymbol{i}_{\mathrm{r,ref}}^{dq'} := (\widehat{\imath}_{\mathrm{r,ref}},\ 0)^{\top} := \left(-\frac{i_{\mathrm{r,ref,sat}}^{q}}{\cos(\delta)},\ 0 \right)^{\top} \tag{101}$$

with measured or known load angle $\delta = \phi_{i_{\mathrm{r}}}^{dq} + \frac{\pi}{2} - \phi_{u_{\mathrm{s}}}^{dq}$, see (15), where δ is filtered with the same time constant T_{u} as the other voltage control inputs (see [2, Table X]).

[15] Besides, for VSM control without FTC, load angle instability occurred in some cases without compensation, i.e., assuming $\cos(\delta) = 1$ in (101).

[16] Also, the definitions of δ_{v}' and $\delta_{\mathrm{v}} := \phi_{\mathrm{e,v}} - \phi_{\mathrm{g}}$ differ, see Section III-E.

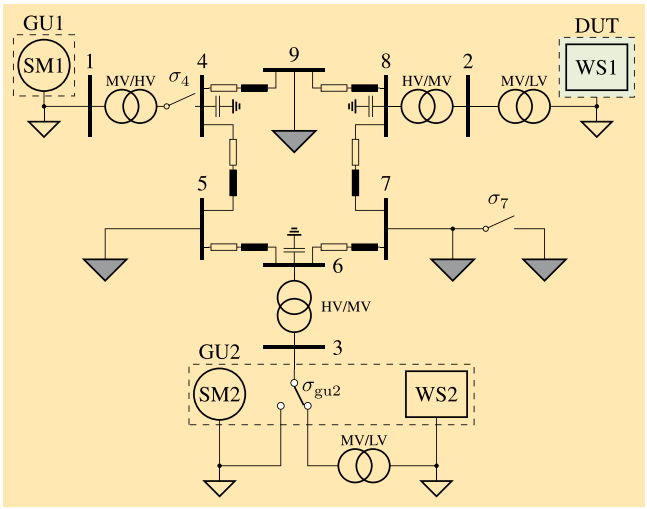

FIGURE 9. IEEE 9-bus test system [ ] for the DUT [ ] with DFIM-based WSs, main loads [▽], and (small) local loads [▽] (for parameters, see [2, Table XI]).

Note that the reference currents for the VSM control with FTC could also be adapted similarly to (101) based on the VSM load angle $\delta_v := \phi_{e,v} - \phi_g$, which corresponds to the grid-voltage-misalignment of the dq-reference frame. However, due to $\delta_v \approx 0$ during normal operation and neglecting temporarily misalignments during RoCoF events, this is not implemented for simplicity.

Remark (R.8): *In [36], GUs have to tolerate grid voltage deviations of up to* $\Delta\widehat{U}_g := \max|\widehat{u}_{g,R} - \widehat{u}_g|/\widehat{u}_{g,R} = 10\%$ *during normal operation [see tolerance band [ ] in Fig. 7(b)]. For a time interval of up to 60 s, GUs have to tolerate higher deviations of up to* $\Delta\widehat{U}_g = 15\%$. *After a fault, GUs have to tolerate even higher deviations and have to stay grid-connected, especially for low-voltage transients. The admissible transient voltage range [ ] is defined by so-called fault-ride-through-curves [36], see Fig. 7(b). For instance, considering the lower fault-ride-through-curve in Fig. 7(b), the lower voltage limit is* $\widehat{U}_g := \frac{\widehat{u}_g}{\widehat{u}_{g,R}} = 15\%$ *for* $0 \le t \le 150$ *ms after a symmetrical fault at* $t_0 = 0$, *before the lower limit linearly increases to* $\widehat{U}_g = 85\%$ *at* $t = 3$ *s.*

IV. SIMULATION RESULTS

The modeling and proposed control of the device under test (DUT), namely the DFIM-based WS, is implemented based on Fig. 4. The simulation scenarios in this section consider both, the normal operation and the response to grid faults.

A. IEEE 9-BUS TEST SYSTEM

This article adapts the IEEE 9-bus test system [12], [38], but the DFIM-based WSs (at bus 2 and 3) in Fig. 9 replace the inverters with simplified dc energy source models from [12]. Different grid configurations are defined in the following for switch σ_{gu2} in the left (SM2) or right (WS2) position (see Fig. 9):

TABLE 2. Simulation scenarios and respective sections of the corresponding simulation results, switches σ_4, σ_7, and σ_{gu2} in Fig. 9, WS scaling factor n_{wu}, and wind speed v_w changing from $9\frac{m}{s}$ *to* $13\frac{m}{s}$ within $\Delta t = 1$ s for Scenarios SN_1–SN_3, but with constant rated wind speed $v_w = v_{w,R} = 11.17\frac{m}{s}$ for Scenarios SF_1–SF_4.

Scenario	Section	σ_4	σ_7	σ_{gu2}	n_{wu}	$v_w/\frac{m}{s}$
SN_1	IV-D1	1	0	SM2	1	$9 \to 13$
SN_2	IV-D2	1	0	SM2	20	$9 \to 13$
SN_3	IV-D3	1	0	WS2	20	$9 \to 13$
SF_1	IV-E1	1	$0 \to 1$	WS2	20	11.17
SF_2	IV-E2	$1 \to 0$	0	SM2	20	11.17
SF_3	IV-E3	$1 \to 0$	0	WS2	20	11.17
SF_4	IV-E4	0	$0 \to 1$	WS2	40	11.17

1) SM-dominated power system—for $\sigma_{gu2} = $ SM2;
2) WS-dominated power system—for $\sigma_{gu2} = $ WS2.

Moreover, the renewable power penetration levels differ for different WS scaling factors n_{wu} in Table 2. Different grid faults are defined for switching σ_7, σ_4 (see Fig. 9):

1) load disturbance—for $\sigma_7 = 0 \to 1$ (closing);
2) loss of SM—for $\sigma_4 = 1 \to 0$ (opening).

The SM subsystems in Fig. 9 include an SM model with excitation (field) winding *and* three-phase damper winding in the rotor, an excitation system with built-in automatic voltage regulator and a corresponding power system stabilizer, as well as a (speed) governor and turbine dynamics. The latter are modeled by a proportional speed droop control and a first-order lag system, respectively, i.e.,

$$P_{sm,ref} := P_{sm,ref,0} + k_{d,sm}\left(\omega_{g,R} - n_{p,sm}\omega_{sm}\right) \tag{102}$$

$$\frac{d}{dt}P_{t,sm} = \frac{1}{T_{gov}}\left(P_{sm,ref} - P_{t,sm}\right) \tag{103}$$

with SM power reference $P_{sm,ref} := p_{sm,ref}/p_{sm,R}$ (in p.u.) or $p_{sm,ref}$ (in W), rated SM power $p_{sm,R} < 0$, initial SM power reference (at zero speed deviation) $P_{sm,ref,0}$, SM pole pair number $n_{p,sm}$, SM angular velocity ω_{sm}, rated SM electrical angular velocity or rated grid angular velocity $\omega_{g,R}$, SM droop gain $k_{d,sm}$, SM turbine power $P_{t,sm}$, and mechanical/thermal turbine or governor time constant T_{gov}. For further model descriptions, we refer to [12] and [38]. All grid model parameters are collected in [2, Table XI].

B. CONSIDERED SIMULATION SCENARIOS

Three scenarios consider normal operation (SN_i) and *four* scenarios consider the response to grid faults (SF_i). The seven scenarios for the DUT (WS1) are listed in Tables 2–4 and described in the following.

SN_1—MPPT in bulk power system: The wind speed changes for WS1, operating in *MPPT mode* and connected to an *SM-based power system with a single WU* ($n_{wu} = 1$).

SN_2—MPPT in SM-dominated power system: The wind speed changes for WS1 ($n_{wu} = 20$), operating in *MPPT mode* and connected to an *SM-dominated power system*.

SN_3—MPPT in WS-dominated power system: The wind speed changes for WS1 ($n_{wu} = 20$), operating in *MPPT mode* and connected to a *WS-dominated power system*.

TABLE 3. Rated machine power of each GU *i* in Fig. 9 and rated system power for all scenarios in Table 2 with corresponding figures of the simulation results.

Scenario	Fig.	$-\frac{p_{\mathrm{m,R},i}}{s_\mathrm{b}}$ SM1	SM2	WS1	WS2	$-\frac{p_{\mathrm{sys,R}}}{s_\mathrm{b}}$ System
SN_1	15	1	1	0.05	-	2.05
SN_2	16–18	1	1	1	-	3
SN_3	19	1	-	1	2	4
SF_1	20	1	-	1	2	4
SF_2	21–23	-	1	1	-	2
SF_3	24	-	-	1	2	3
SF_4	25	-	-	2	2	4

TABLE 4. (V)SM inertia of each GU *i* in Fig. 9 and power system inertia, see (6), for all scenarios in Table 2 with corresponding figures of the simulation results.

Scenario	Figure	$H_{(\mathrm{v}),i}$ / s SM1	SM2	WS1	WS2	H_sys / s System
SN_1	15	3.7	3.7	5	-	3.732
SN_2	16–17	3.7	3.7	5	-	4.133
	18	3.7	3.7	0	-	2.467
SN_3	19	3.7	-	5	5	4.675
SF_1	20, 12	3.7	-	5	5	4.675
	12	3.7	-	0.1	5	3.450
	12	3.7	-	25	5	9.675
SF_2	21–23	-	3.7	5	-	4.350
SF_3	24	-	-	5	5	5
SF_4	25	-	-	5	5	5

SF_1—Load disturbance in WS-dominated power system: The WS1 ($n_\mathrm{wu} = 20$) operates in MPPT mode, when a *load disturbance* occurs in the *WS-dominated power system*.

SF_2—Loss of SM in SM-dominated power system: The WS1 ($n_\mathrm{wu} = 20$) operates in RPPT mode, when a *loss of SM* occurs in the *SM-dominated power system*.

SF_3—Loss of SM in WS-dominanted power system: The WS1 ($n_\mathrm{wu} = 20$) operates in RPPT mode, when a *loss of SM* occurs in the *WS-dominated power system*.

SF_4—Load disturbance in WS-based power system: The WS1 ($n_\mathrm{wu} = 40$) operates in RPPT mode, when a *load disturbance* occurs in the *WS-based power system* (no SM).

Besides the scenario parameters in Table 2, the WS2 wind speed and scaling factor are always $v_\mathrm{w} = v_\mathrm{w,R}$ and $n_{\mathrm{wu},2} = 40$, respectively. The WS2 droop gain and grid frequency tolerance bandwidth always equal the corresponding SM parameters, i.e., $k_{\mathrm{d},2} = k_\mathrm{d,sm}$ and $\Delta\omega_{\mathrm{g,d},2} = \Delta\omega_\mathrm{g,d,sm}$ (see [2, Table XI]). Table 3 lists the rated machine power $-\frac{p_{\mathrm{m,R},i}}{s_\mathrm{b}}$ of each GU i (SM1/2, WS1/2) and the rated system power $-\frac{p_\mathrm{sys,R}}{s_\mathrm{b}}$ with $p_\mathrm{sys,R} := \sum p_{\mathrm{m,R},i}$ for all scenarios. With this and the (V)SM inertia constant $H_{(\mathrm{v}),i}$ of each GU i, the power system inertia H_sys in Table 4 is calculated based on (6) for all scenarios. Note that Tables 3 and 4 consider postfault conditions, see also Remark (R.1).

C. PRESENTATION OF THE SIMULATION RESULTS

For the following simulation results, if not stated otherwise, all quantities are normalized with respect to (w.r.t.) their rated values. For power quantities, such as P and Q, the default normalization is w.r.t. the rated active power $p_\mathrm{R} < 0$ of the GU, corresponding to the (negative) base (load) power $s_\mathrm{b} = 100$ MVA in most cases (see [2, Table XI]). The WU stator, rotor, and filter currents are normalized w.r.t. their rated values $\widehat{\imath}_\mathrm{s,R}$, $\widehat{\imath}_\mathrm{r,R}$, and $\widehat{\imath}_\mathrm{f,R}$, respectively. Note that the WU grid-side filter currents are also normalized w.r.t. $\widehat{\imath}_\mathrm{f,R}$, e.g., $I_\mathrm{g}^d := i_\mathrm{g}^d / \widehat{\imath}_\mathrm{f,R}$ (see the WU configuration in Fig. 1).

The figures listed in Table 3 present the simulation results of all scenarios (see Table 2) and follow the same structure of time series plots (subplots), which show the following quantities (see, e.g., Fig. 17):

1) machine and turbine power of WS1;
2) VSM load angle of WS1/2;
3) load angle of all GUs (DFIMs and SMs);
4) machine and turbine power of GU1/2;
5) VSM mechanical and turbine power of WS1/2;
6) reactive power of all GUs (at the PCC);
7) aggregated machine and turbine power, i.e., sums of corresponding GU power from 1) and 4);
8) power system machine and turbine power, i.e., sums of corresponding (V)SM power from 4) and 5), see (R.9);
9) aggregated reactive power, i.e., sum of GU reactive power from 6);
10) angular velocity of all (V)SMs and grid angular velocity at the DUT's PCC;
11) grid RoCoF at the DUT's PCC, and power system RoCoF, calculated with (6) and data from 8), see (R.9);
12) voltage amplitudes of all GUs (at their PCCs);
13) DUT actual and rated wind speed;
14) DUT actual and optimal (MPP) tip speed ratio;
15) DUT actual and reference blade pitch angle;
16) DUT MPPT compensated, see (29), and actual WT or DFIM angular velocity;
17) DUT actual and saturated reference DFIM torque;
18) DUT VSM, virtual damping, and virtual turbine torque;
19) DUT actual rotor, reference rotor, and stator currents;
20) DUT actual, reference, and grid-side filter currents;
21) DUT dc-link voltage;
22) DUT DFIM, PCC, stator, and available turbine power;
23) DUT grid-side filter and rotor power;
24) DUT stator, grid-side filter, PCC, and rotor reactive power.

Note that the background colors relate to Fig. 9, i.e., the subplots 1–12 relate to the power system [ ], whereas subplots 13–24 relate to the DUT [ ]. Moreover, for a simple and fair comparison of the results, an identical RoCoF tolerance for normal operation of $\pm 0.2\frac{\%}{\mathrm{s}}$ is assumed, see, e.g., the tolerance band [ ] in subplot 11 of Fig. 16, which is higher than the maximum RoCoF of $10\frac{\mathrm{mHz}}{\mathrm{s}}$ or $0.02\frac{\%}{\mathrm{s}}$ observed in the European grid during normal operation ("ordinary operation"

in [4]), but corresponds to 10% of the critical RoCoF of $1\frac{\text{Hz}}{\text{s}}$ or $2\frac{\%}{\text{s}}$ in [4]. The grid frequency and voltage tolerance bands for normal operation are visualized in green according to (R.5) and (R.8), see, e.g., [ ] in subplots 10 and 12 of Fig. 16, respectively. Finally, for grid faults, also the extended admissible ranges for grid frequency [ ] and voltage [ ] according to Fig. 7 are indicated (see, e.g., subplots 10 and 12 of Fig. 21, respectively).

Remark (R.9): *The power system RoCoF $\dot{\Omega}_{sys}$ calculation (6) should include all GUs, i.e., not only SMs but also IBRs or DFIM-based WSs with (i) GFL control or with (ii) GFM/VSM control. Only (V)SMs provide power system inertia, i.e., for GU i with GFL control, inserting $H_i = p_{\text{t},i} = p_{\text{m},i} = 0$ in (6), but, for GU i with GFM/VSM control, inserting the corresponding VSM quantities $H_{\text{v},i}$, $p_{\text{t,v},i}$, and $p_{\text{m,v},i}$, leads to the desired inclusion of IBRs in (6). The rated system power $p_{sys,\text{R}} := \sum p_{\text{m,R},i}$ includes all GUs. Thus, more GUs with GFL control lead to decreasing system inertia constant H_{sys} in (6) as $p_{sys,\text{R}}$ appears in the denominator. The parameters $p_{sys,\text{R}}$ and H_{sys} are constant for each simulation, see Tables 3 and 4;*[17] *whereas $P_{\text{m},sys}(t)$ and $P_{\text{t},sys}(t)$ depend on the dynamics of all grid-connected (V)SMs, e.g., aggregating subplots 4 and 5 leads to subplot 8 in Fig. 16, see also (R.1). Finally, using $P_{\text{m},sys}(t)$ and $P_{\text{t},sys}(t)$ as inputs for (6) leads to $\dot{\Omega}_{sys}$, see, e.g., subplot 11 in Fig. 16. Note that the system power $P_{\text{m},sys}$ is the sum of the mechanical power of all (V)SMs. For SMs, the mechanical and electrical power are approximately equal; but for VSMs, the mechanical power $P_{\text{m,v}}$ includes the internal damping power, whereas the electrical power $P_{el,\text{v}}$ does not include it, since no real damper windings exist, see Remark (R.4). Therefore, and since the VSM grid synchronization depends on the VSM mechanical dynamics, calculating $P_{\text{m},sys}$ based on $P_{el,\text{v}}$ (instead of based on $P_{\text{m,v}}$) would lead to wrong RoCoFs.*[18]

D. DISCUSSION: NORMAL OPERATION (SN_{1-3})

For scenarios SN_1–SN_3, normal operation without grid faults is considered. The wind speed changes within $\Delta t = 1$ s from $v_\text{w} = 9\frac{\text{m}}{\text{s}}$ at $t_0 = 4$ s to $v_\text{w} = 13\frac{\text{m}}{\text{s}}$ to evaluate the MPPT performance, see, e.g., subplot 13 of Fig. 15. Three different power system configurations are simulated and discussed in the following (see also Table 2):

(i) the bulk power system in Section IV-D1;
(ii) the SM-dominated system in Section IV-D2;
(iii) the WS-dominated system in Section IV-D3.

Moreover, the following three different control variants are compared:

(a) the proposed VSM control with FTC;
(b) the VSM control without FTC, see Section III-G3b;
(c) standard GFL control with PLL instead of VSM control, see also [6].

1) SN_1—MPPT IN BULK POWER SYSTEM

The WS consists of a single WU with $p_{\text{m,R}} = -5$ MW for the considered scenario, see Table 2 and [2, Table IX]. Moreover, two SMs, with $p_{\text{sm,R}} = -100$ MW each, are connected to the IEEE 9-bus (see ibid.). Neglecting any conversion or transmission losses and local voltage deviations, the rated total power demand is given by the sum of all rated (local and distant) load power, i.e., $p_{\text{load,R}} := 3p_{\text{loc,R}} + 3p_{\text{dist,R}} = 2.55 s_\text{b} = 255$ MW (see Fig. 9 and [2, Table XI]). The initial power references of both SMs are set to $P_{\text{sm,ref},0} := \frac{-p_{\text{load,R}}}{2p_{\text{sm,R}}} = 127.5\%$ in (102), to roughly fulfill the power demand. Note that $P_{\text{sm,ref},0}$ corresponds to the actual SM power at rated grid frequency (inactive droop). However, due to power demand underestimation, the grid frequency and the SM speed are slightly below rated values initially, i.e., $\Omega_\text{g}(0) \approx \Omega_{\text{sm}}(0) < 1$ in subplot 10 of Fig. 15. Consequently, the SM speed governor increases the SM power reference, i.e., $P_{\text{sm,ref}} = P_{\text{sm,ref},0} + K_{\text{d,sm}}(1 - \Omega_{\text{sm}})$ with p.u. droop gain $K_{\text{d,sm}} := k_{\text{d,sm}}\omega_{\text{g,R}}$ in (102). Thus, the SM power is greater than the initial SM power reference, i.e., $P_{\text{sm}} > 130\% > P_{\text{sm,ref},0}$ in subplot 4 of Fig. 15.[19]

The power of the considered WS (here a single WU) is rather negligible in comparison to the overall power demand, i.e., $|\frac{p_{\text{m,R}}}{p_{\text{load,R}}}| < 2\%$, which is also typical for WUs in large interconnected grids or so-called *bulk power systems*. In these systems, grid frequency and voltage are approximately constant for a power or wind change of a single WU (see subplots 10, 12, and 13 of Fig. 15). In this case, an infinite bus may be sufficient to model the grid connection.

With increasing wind speed, the WT speed Ω_m increases and the MPPT increases the DFIM torque reference $\overline{M}_{\text{m,ref}}$. When exceeding the rated speed $\Omega_\text{m} = 1$ at $t \approx 8.5$ s, the torque reference is saturated to $\overline{M}_{\text{m,ref}} = 1$ and the pitch control gets active, i.e., β increases, see subplots 15–17 of Fig. 15. Note the WT speed overshoot induced by the rather slow pitch control dynamics (compared with the FTC dynamics), i.e., Ω_m further increases to above 102.5% before decreasing to its reference $\Omega_{\text{m,ref}} = 100\%$. Thus, the DFIM power $P_\text{m} = \Omega_\text{m} M_\text{m}$ in subplot 22 of Fig. 15 also overshoots before reaching the saturated available power $\overline{P}_\text{t}^\star$ at steady state, i.e., $P_\text{m} = \overline{P}_\text{t}^\star = 1$ for $t \to \infty$.

The VSM quantities are shown in subplots 2 and 18 of Fig. 15. Due to the inactive droop control, i.e., $M_{\text{t,v}} = 0$, the VSM torque synchronization loop achieves grid voltage alignment, i.e., $\delta_\text{v} \approx 0$. The remaining deviation $\delta_\text{v} < 0$ in Fig. 15 is due to the inaccuracy of the FTC induced by assumption (A.1), i.e., taking the stator resistance into account could improve the FTC and alignment accuracy.

The simulation results for VSM control without FTC and for GFL control are shown in [2, Figs. 12 and 13] but not here due to nearly identical power system dynamics. However, Fig. 10 compares the simulation results for the three

[17] Here, the time-dependency of H_{sys} in (R.1) is dropped due to steady-state initialization (zero RoCoF), i.e., Table 4 considers postfault conditions.

[18] Significant RoCoF errors were observed in this case (not shown here).

[19] Neglecting any losses and electromagnetic transients, the SM electrical and mechanical power are assumed to be equal, i.e., $P_{\text{sm}} = P_{\text{m,sm}}$.

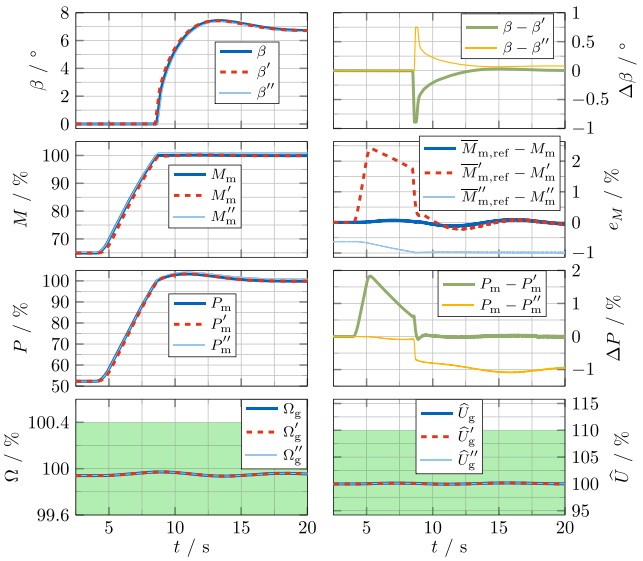

FIGURE 10. Simulation results of scenario SN$_1$: MPPT in bulk power system comparing different control variants (see Fig. 15, [2, Figs. 12 and 13]). The quantities with superscript •′ denote the VSM control without FTC. The quantities with superscript •″ denote the standard GFL control, using a PLL instead of a VSM for grid synchronization.

control variants. Without FTC, the VSM torque synchronization loop achieves torque reference tracking but with transient torque control errors $e'_M := \overline{M}'_{\mathrm{m,ref}} - M'_{\mathrm{m}}$ [- - -] exceeding 2% in Fig. 10. Thus, the FTC increases the DFIM power P_{m} by more than 1.75% for the considered wind speed change, see $\Delta P'_{\mathrm{m}} := P_{\mathrm{m}} - P'_{\mathrm{m}}$ [——]. Moreover, without the proposed FTC, the blade pitch controller has to compensate for the torque reference tracking delay to keep the WT speed within the admissible range, leading to faster activation of the blade pitch system, see β [- - -] and $\Delta\beta := \beta - \beta'$ [——] in Fig. 10. Taking the volatile nature of realistic wind profiles into account, this effect may lead to (even) higher pitch actuation, and thus, to (even) higher mechanical stress, which would require further investigations as it does not occur for standard GFL control, see also [22] and [27].

The GFL control exhibits a nonvanishing steady-state torque control error $e''_M := \overline{M}''_{\mathrm{m,ref}} - M''_{\mathrm{m}} < 0$ [——] in Fig. 10, since the FTC neglects the DFIM resistances in Assumption (A.1) and there is no torque feedback. In contrast to that, for the VSM control variants, the torque synchronization loop compensates for this error. Due to the higher torque magnitude, i.e., $M''_{\mathrm{m}} > M_{\mathrm{m}}$, induced by the torque control error e''_M, the GFL control seems to achieve higher DFIM power, i.e., $\Delta P''_{\mathrm{m}} := P_{\mathrm{m}} - P''_{\mathrm{m}} < 0$ [——], and slower activation of the blade pitch system, see β'' [——] and $\Delta\beta'' := \beta - \beta''$ [——]. However, the DFIM power actually exceeds its rated value by approximately $P''_{\mathrm{m}} - 1 = 1\%$ at steady state, which is not admissible (at least for a long period of time). Considering the transient response with inactive pitch control before reaching the rated speed, i.e., for 4 s $< t <$ 8.5 s, the performances of the GFL control and the VSM control with FTC are almost identical, i.e., $\Delta P''_{\mathrm{m}} := P_{\mathrm{m}} - P''_{\mathrm{m}} \approx 0$ [——] in Fig. 10.

In conclusion, the VSM control with FTC improves the MPPT performance and increases the wind energy yield compared with the VSM control without FTC. For the latter, the other GUs or SMs have to compensate for the reduced WS output power. This effect is undesired, especially for SMs connected to nonrenewable energy sources, such as coal-fired steam turbines. The transient response of the VSM control with FTC and the standard GFL control are comparable. Considering the steady-state torque control error, the torque synchronization loop of the VSM control compensates for any simplification error of the FTC, assuming an ideal DFIM torque estimation for the VSM torque feedback. In contrast to that, for GFL control, there is no torque feedback and any FTC simplification errors result in nonvanishing steady-state torque control errors.

2) SN$_2$—MPPT IN SM-DOMINATED POWER SYSTEM

The WS is scaled by the factor $n_{\mathrm{wu}} := \frac{p_{\mathrm{sm,R}}}{p_{\mathrm{m,R}}} = 20$ to the rated SM power $p_{\mathrm{sm,R}} = -100$ MW, i.e., the WS power rating $p_{\mathrm{ws,R}} = n_{\mathrm{wu}} p_{\mathrm{m,R}} = -100$ MW corresponds to the parallel connection of n_{wu} identical WUs with $p_{\mathrm{m,R}} = -5$ MW each (see the grid connection in Fig. 4, Table 2, [2, Table X]). With rated initial SM power references, i.e., $P_{\mathrm{sm,ref,0}} = 1$, the initial grid power demand exceeds the sum of the rated SM power generation plus the initial WS power at $v_{\mathrm{w}} = 9\frac{\mathrm{m}}{\mathrm{s}}$. Thus, the initial grid frequency is below and the initial power of the droop-controlled SMs is above its rating, see subplots 10 and 4 of Figs. 16, 17, and 18, respectively.

With increasing wind speed, the WT speed increases. Again, the MPPT increases the DFIM torque as in the previous scenario for the bulk power system; but, now with higher WS rating, this leads to nonnegligible interactions between the GUs. With increasing WS power $P_{\mathrm{m,ws1}}$ for 4 s $< t <$ 8.5 s in subplot 1 of Fig. 16, the grid frequency Ω_{g} increases noticeably in subplot 10, which decreases the SM power P_{sm} in subplot 4. In reality, the wind speed may not rapidly increase simultaneously for all $n_{\mathrm{wu}} = 20$ WTs, such that this scenario can be considered as extreme (worst-case) grid (frequency) event for normal operation.

For VSM control with and without FTC in Figs. 16 and 17, respectively, the grid voltage amplitude deviations are rather small, i.e., $|\widehat{U}_{\mathrm{g}} - 1| < 3\%$ in subplots 12, compared with the normal tolerance of $\pm 10\%$, see (R.8). Instead, the grid frequency leaves the normal operation range [■] in subplots 10 for a few seconds, but Ω_{g} does not exceed 100.6%, i.e., the deviation is critical but within the admissable range according to the grid codes (R.5), and the grid frequency oscillations vanish shortly afterward. In contrast to that, the standard GFL control in Fig. 18 leads to higher grid frequency oscillations for $t <$ 30 s, i.e., the first peak of Ω_{g} exceeds 100.6%. In other words, the VSM control improves the grid frequency oscillation damping compared with GFL control. Moreover, for GFL control, the destabilizing effect of the PLL [5] leads to high oscillations or even instability for $t >$ 30 s in Fig. 18.

The turbine power $P_{\mathrm{t,ws1}}$ of the DUT (WS1) and thus also the aggregated turbine power $P_{\mathrm{t,agg}}$ increase with increasing

wind speed as visualized in subplots 1, 7, and 13 of Fig. 16. After the wind speed change, i.e., for $t > 5$ s, the turbine power $P_{\mathrm{t,ws1}}$ further increases for a short period due to the increasing tip speed ratio λ in subplot 14, before $P_{\mathrm{t,ws1}}$ decreases again due to the increasing blade pitch angle β in subplot 15. Finally, at the new steady-state operating point, $P_{\mathrm{t,ws1}}$ reaches its rated value of 100%.

The area between $P_{\mathrm{t,ws1}}$ and $P_{\mathrm{m,ws1}}$ in subplot 1 of Fig. 16 corresponds to the energy needed to accelerate the WS to rated speed. Similarly, the area between $P_{\mathrm{t,agg}}$ and $P_{\mathrm{m,agg}}$ in subplot 7 corresponds to the energy needed to accelerate all (real) rotating masses of the power system to the new steady-state operating point. However, since the SM speed changes (see Ω_{sm1}, Ω_{sm2} in subplot 10) are rather negligible in comparison to the WS speed changes (see Ω_{m} in subplot 16), the area between $P_{\mathrm{t,agg}}$ and $P_{\mathrm{m,agg}}$ mainly corresponds to the energy needed to accelerate the WS.[20] Clearly, $P_{\mathrm{t,agg}}$ and $P_{\mathrm{m,agg}}$ cannot be used for the RoCoF calculation in (6), as $P_{\mathrm{t,agg}}$ includes the asynchronously rotating WT. Instead, the system turbine and machine power $P_{\mathrm{t,sys}}$ and $P_{\mathrm{m,sys}}$ in (6) have to be calculated based on all synchronously rotating (V)SMs, i.e., the time series in subplot 8 in Fig. 16 are obtained based on the aggregation of subplots 4 and 5, see Remark (R.9). Finally, with the system acceleration proportional to the system power imbalance, i.e., $\dot{\Omega}_{\mathrm{sys}} \propto \Delta P_{\mathrm{sys}} := P_{\mathrm{t,sys}} - P_{\mathrm{m,sys}}$ in (6), the RoCoF is approximated, see $\dot{\Omega}_{\mathrm{sys}} \approx \dot{\Omega}_{\mathrm{g}}$ in subplot 11 of Fig. 16.

The (V)SM power system dynamics can be interpreted as follows. The power generation consists of two real (loaded) SMs, namely SM1/2, and one freely spinning VSM, realized by WS(1). The WS reference power $\overline{P}_{\mathrm{m,ref}}$ is not considered as power generation but as (negative) power demand (load), such that, at the initial steady state, only the SMs generate the system machine power (see subplots 4 and 8 in Fig. 16)

$$\overset{t=0}{\Rightarrow} P_{\mathrm{m,sys}} = -\frac{s_{\mathrm{b}}}{p_{\mathrm{sys,R}}}\left(P_{\mathrm{m,sm1}} + P_{\mathrm{m,sm2}}\right) \approx \frac{2 \cdot 110}{300} \approx 73.3\%.$$

The wind speed change at $t_0 = 4$ s increases the WS reference power $\overline{P}_{\mathrm{m,ref}}$, interpreted as decreasing power demand, such that Ω_{g} increases and the inertial response of all (V)SMs decreases $P_{\mathrm{m,sys}}$, see subplots 10 and 8 in Fig. 16, respectively. At the same time, the SM droop control reduces $P_{\mathrm{t,sys}}$ accordingly (see subplot 8). With vanishing RoCoFs, the VSM inertial power decreases to zero (see subplot 5). Again, at the new steady state, only the two SMs generate the system machine power (see subplots 4 and 8 in Fig. 16)

$$\overset{t\to\infty}{\Rightarrow} P_{\mathrm{m,sys}} = -\frac{s_{\mathrm{b}}}{p_{\mathrm{sys,R}}}\left(P_{\mathrm{m,sm1}} + P_{\mathrm{m,sm2}}\right) \approx \frac{2 \cdot 86}{300} \approx 57.3\%.$$

The VSM quantities for the VSM control with/without FTC are shown in subplots 2 and 18 of Figs. 16 and 17. In contrast to $\delta_{\mathrm{v}} \approx 0$ for VSM control with FTC, the VSM control without FTC does not achieve grid voltage alignment at steady state, i.e., $\delta_{\mathrm{v}} \neq 0$ (superscript $\bullet'$ dropped for better readability), see subplot 2. With FTC, the VSM torque synchronization loop only needs to compensate for FTC errors; whereas, without FTC, the VSM fully controls the DFIM torque. In the latter case, the torque reference tracking depends on the VSM synchronization delay, resulting in higher torque control errors, see Fig. 11, as already observed in the previous scenario SN_1, see Fig. 10. However, in this scenario SN_2, even with FTC, the oscillations of the torque control error or VSM torque $M_{\mathrm{m,v}} \approx M_{\mathrm{m}} - \overline{M}_{\mathrm{m,ref}}$ (see Fig. 4) are not negligible any more (although smaller than without FTC), see subplot 18 in Fig. 16. Note that the droop control decreases $M_{\mathrm{t,v}}$ (subplot 18) to counteract the grid frequency deviation, when Ω_{g} (subplot 10) exceeds its upper normal tolerance limit of 104% at $t \approx 7.5$ s. Thus, the droop control counteracts the FTC, which should track the increasing torque reference $\overline{M}_{\mathrm{m,ref}}$ (subplot 17), and further increases the torque control error $e_M := \overline{M}_{\mathrm{m,ref}} - M_{\mathrm{m}}$ [—] for 7.5 s $< t <$ 10 s in Fig. 11. However, even for the other time intervals with $M_{\mathrm{t,v}} = 0$, the oscillations of $M_{\mathrm{m,v}}$ or e_M are higher than for the previously considered bulk power system. This is due to the interacting inertial responses of the (V)SMs as explained in the following.

Neglecting droop control, a power imbalance ΔP_{sys} is distributed to all rotating masses of the (V)SMs, i.e.,

$$\overset{(6)}{\Rightarrow} \quad \Delta P_{\mathrm{sys}} = 2H_{\mathrm{sys}}\dot{\Omega}_{\mathrm{sys}} = 2\frac{\sum E_{\mathrm{kin},i}}{-p_{\mathrm{sys,R}}}\dot{\Omega}_{\mathrm{sys}}. \tag{104}$$

Note that, for the VSM-controlled WS, instead of the physical inertia constant H, the VSM inertia constant H_{v} has to be inserted for H_i in (104), see Remark (R.9). According to (104), the inertial power share of the ith (V)SM equals its share of kinetic energy. For the previously considered scenario SN_1, the WS power change, induced by the wind speed change, and also its VSM kinetic energy were negligible, i.e.,

$$\Delta P_{\mathrm{m}} := \frac{p_{\mathrm{m}}|_{v_{\mathrm{w}}=9\frac{\mathrm{m}}{\mathrm{s}}} - p_{\mathrm{m}}|_{v_{\mathrm{w}}=13\frac{\mathrm{m}}{\mathrm{s}}}}{p_{\mathrm{load,R}}} \approx \frac{2.5\ \mathrm{MW}}{255\ \mathrm{MW}} \approx 1\%$$

$$\frac{E_{\mathrm{kin,v}}}{E_{\mathrm{kin,sys}}} = \frac{H_{\mathrm{v}}p_{\mathrm{m,R}}}{H_{\mathrm{v}}p_{\mathrm{m,R}} + n_{\mathrm{sm}}H_{\mathrm{sm}}p_{\mathrm{sm,R}}} = \frac{5\ \mathrm{s} \cdot 5\ \mathrm{MW}}{5\ \mathrm{s} \cdot 5\ \mathrm{MW} + 2 \cdot 3.7\ \mathrm{s} \cdot 100\ \mathrm{MW}} \approx 3.3\%.$$

using $H_{\mathrm{v}} = 5$ s for the VSM and $H = 3.7$ s for the $n_{\mathrm{sm}} = 2$ SMs, see Table 4 and [2, Tables X and XI]. For this scenario SN_2

$$\Delta P_{\mathrm{m}} := \frac{p_{\mathrm{m}}|_{v_{\mathrm{w}}=9\frac{\mathrm{m}}{\mathrm{s}}} - p_{\mathrm{m}}|_{v_{\mathrm{w}}=13\frac{\mathrm{m}}{\mathrm{s}}}}{p_{\mathrm{load,R}}} \approx \frac{50\ \mathrm{MW}}{255\ \mathrm{MW}} \approx 20\%$$

$$\frac{E_{\mathrm{kin,v}}}{E_{\mathrm{kin,sys}}} = \frac{5\ \mathrm{s} \cdot 100\ \mathrm{MW}}{5\ \mathrm{s} \cdot 100\ \mathrm{MW} + 2 \cdot 3.7\ \mathrm{s} \cdot 100\ \mathrm{MW}} \approx 40\%$$

the VSM inertial response is *not* negligible in (104). The VSM inertial response counteracts the FTC or MPPT, as shown in Fig. 16, i.e., the increasing torque reference $\overline{M}_{\mathrm{m,ref}}$ (subplot 17) increases the WS power P_{m} (subplot 22), which increases

[20] Actually, not only the speed but also the inertia constant values are relevant for the kinetic energy consideration, but the (physical) inertia constant $H = 7.816$ s of the WS [2, Table IX] is higher than the inertia constant $H = 3.7$ s of the SMs [2, Table XI], i.e., the area between $P_{\mathrm{t,agg}}$ and $P_{\mathrm{m,agg}}$ still mainly corresponds to the WS's kinetic energy change.

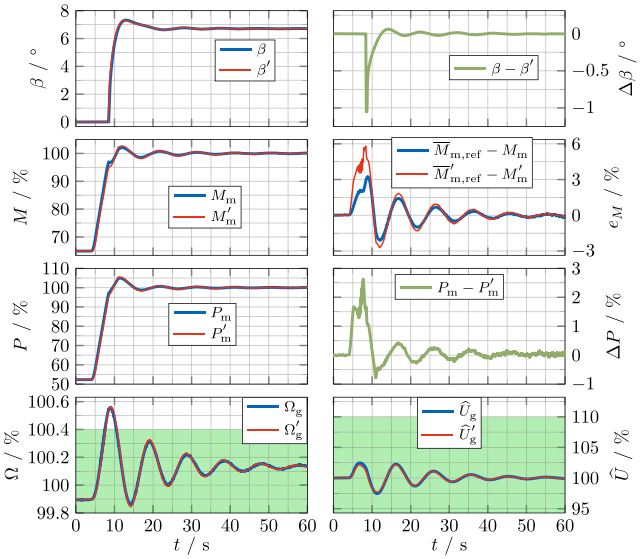

FIGURE 11. Simulation results of scenario SN_2: MPPT in SM-dominated power system comparing VSM control with and without FTC (see Figs. 16 and 17). The quantities with superscript $\bullet'$ denote the VSM control without FTC.

the grid frequency (subplot 10). Consequently, the VSM load angle δ_v (subplot 2) decreases, which decreases the actual DFIM torque M_m or $M_{m,v}$ (subplots 17 and 18). Finally, this is the main reason for higher torque control errors than in the previous scenario, cf. Figs. 10 and 11.

In Fig. 11, considering the comparison of the VSM control with and without FTC in detail, the FTC achieves less severe power or torque oscillations, i.e., the torque control error $e_M := \overline{M}_{m,ref} - M_m$ with FTC [——] is smaller than $e'_M := \overline{M}'_{m,ref} - M'_m$ without FTC [——]. The FTC triggers the power response of the SMs via the grid frequency without additional delay, which is introduced by the VSM inertia for VSM control without FTC. Thus, the FTC reduces the communication delay between the WS and its power-sharing partners (SMs), resulting in (slightly) reduced grid frequency oscillations, compare Ω_g [——] and Ω'_g [——]. With FTC, the grid voltage amplitude oscillations are (slightly) higher but by far not critical, see also (R.8).[21] Finally, the FTC increases the (transient) wind energy yield, with the additionally generated energy corresponding to the area below $\Delta P := P_m - P'_m$ [——] in Fig. 11, which means less energy must be provided by the SMs at the same time. Thus, the FTC increases the share of renewable energy.

3) SN_3—MPPT IN WS-DOMINATED POWER SYSTEM

In scenario SN_3, SM2 is replaced by WS2 with rated power $p_{ws2,R} = n_{wu,2} p_{m,R} = -200$ MW (see Tables 2 and 3), resulting in a WS-dominated power system. Assuming rated wind speed for WS2, i.e., $v_{w,2} = v_{w,R}$, and choosing its relative power reference $P_{m,ref,rel,2} = 50\%$, the WS2 power is equal to the SM power at rated grid frequency, i.e., $p_{ws2,R} P_{m,ref,rel,2} = p_{sm,R}$. WS2 always uses the proposed VSM control with FTC and its VSM is denoted by VSM2, whereas WS(1) with VSM(1) is still the DUT, see also Fig. 9. With the WS2 power reserves, the VSM2 enables droop control similar to the SM(1). For easier comparison, the VSM2 droop gain and grid frequency tolerance bandwidth are identical to the corresponding SM parameters, i.e., $k_{d,2} = k_{d,sm}$ and $\Delta\omega_{g,d,2} = \Delta\omega_{g,d,sm} = 0$ (see [2, Table XI]). Note that the WS2 power quantities are normalized w.r.t. rated SM power or negative base power $p_{sm,R} = -s_b$ (and not w.r.t. $p_{ws2,R}$) for easier comparison between WSs and SMs, see, e.g., subplot 4 in Fig. 19.

The (V)SM power system dynamics, shown in subplots 8 and 11 of Fig. 19, can be interpreted like in the previous scenario, but, instead of two SMs and one VSM, the system now consists of one SM and two VSMs. Again, VSM1 is freely spinning but VSM2 would only freely spin at rated grid frequency as its droop control frequency tolerance is set to zero, i.e., $\Delta\omega_{g,d,2} = 0$. Actually, the grid frequency at the start/end is below/above rated frequency, such that VSM2 provides positive/negative droop power, see Ω_g and $P_{t,v,ws2}$ in subplots 10 and 5 of Fig. 19, respectively. The WS2 power change, see $P_{m,ws2}$ in subplot 4, is approximately proportional to the (negative) grid frequency change, see Ω_g in subplot 10. In contrast, the governor time delay T_{gov} in (103) leads to a significantly slower SM1 droop response, see $P_{m,sm1}$ in subplot 4. The faster droop response of WS2, compared with SM2 in the previous scenario (recall Figs. 16, 17 and 18), is one reason for the improved system damping (see also [17]), as further explained later for grid fault scenarios, e.g., in Section IV-E2.

Since the grid frequency reaches its new steady state faster than for the previously considered SM-dominated system, the VSM torque synchronization loop is only active for a few seconds, see subplots 10 and 18 in Fig. 19. Moreover, $M_{m,v}$ (subplot 18) is smaller than previously due to (i) smaller RoCoF $\dot{\Omega}_g$ (subplot 11), and due to (ii) inactive droop control, i.e., $M_{t,v} = 0$ (subplot 18) as Ω_g (subplot 10) stays within its normal tolerance band of $\pm 0.4\%$ [——].

The results for VSM control without FTC and for GFL control, as well as a comparison to VSM control with FTC (similar to Fig. 8) are shown in [2, Figs. 21–23] but not here due the qualitatively similar conclusions as previously in Section IV-D2, summarized in the following. The FTC leads to (i) lower torque deviations or power oscillations and (ii) higher wind energy yield during transients, compared with VSM control without FTC [2, Fig. 23]. The GFL control leads to high oscillations or even instability in the long run [2, Fig. 22].

E. DISCUSSION: RESPONSE TO GRID FAULTS (SF_{1-4})

Due to the focus on the response to grid faults, all following scenarios assume rated wind conditions, i.e., $v_w = v_{w,R}$.

[21] If smaller grid voltage deviations for VSM control with FTC are desired, (i) more aggressive tuning, or (ii) nonlinear compensation, see also (101), may be considered for voltage control, but this is out of scope of this article due to acceptable control performance in all considered scenarios.

Firstly, Section IV-E1 (SF_1) considers a load disturbance with additional power demand $p_{\mathrm{dist,R}} = 0.75 s_\mathrm{b}$ at bus 7, see Fig. 9 and Table 2. Then, Sections IV-E2 (SF_2) and IV-E3 (SF_3) consider a loss of power generation by disconnection of SM1 for different renewable power penetration. Finally, after the disconnection of SM1, no SM stays grid-connected, i.e., Section IV-E4 (SF_4) considers the load disturbance again, but for WS power generation only. All WSs operate based on the proposed VSM control with FTC (see Fig. 4).

Remark (R.10): *The initial RoCoF determines the time available to respond to power imbalances induced by faults [3], [10]. In the following, a time window with length* $T = 200$ *ms after the fault is considered for the initial RoCoF* $\dot{\Omega}_{\mathrm{g},0}$*, which is in line with values suggested for protection schemes (see, e.g., [39]). Note that the initial RoCoF* $\dot{\Omega}_{\mathrm{g},0}$ *after the fault at* $t_0 = 4$ *s is manually computed over the time window* $[t_0, t_0 + T]$*. However, the RoCoF time series are calculated over a centered time window, i.e.,* $\dot{\Omega}_\mathrm{g}(t) = \frac{\Omega_\mathrm{g}\left(t+\frac{T}{2}\right)-\Omega_\mathrm{g}\left(t-\frac{T}{2}\right)}{T}$ *with filtered* $\Omega_\mathrm{g}(t)$*. Thus,* $\dot{\Omega}_\mathrm{g}(t)$ *may already change just before* t_0*, see, e.g., subplot 11 of Fig. 20, and* $\dot{\Omega}_\mathrm{g}(t_0)$ *may (slightly) differ from* $\dot{\Omega}_{\mathrm{g},0}$*.*

1) SF_1—LOAD DISTURBANCE IN WS-DOMINATED POWER SYSTEM

The configuration equals the one in the previously considered scenario SN_3 (see Section IV-D3), except that a) rated wind speed conditions are assumed for both WSs (WS1/2) and b) a sudden load step occurs at $t_0 = 4$ s (see also Table 2). The initial power of WS1 (DUT) equals its rated power due to MPPT, but the initial power of WS2 is below its rated value due to RPPT with $P_{\mathrm{m,ref,rel,2}} = 50\%$. Moreover, since the sum of all power generation references exceeds the power demand, i.e., $|p_{\mathrm{sm,R}} + p_{\mathrm{ws1,R}} + p_{\mathrm{ws2,R}} P_{\mathrm{m,ref,rel,2}}| = 3 s_\mathrm{b} > p_{\mathrm{load,R}} = 2.55 s_\mathrm{b}$ (see Table 2 and [2, Table XI]), the initial grid frequency is higher than its rated value, see Ω_g in subplot 10 of Fig. 20. Hence, the droop controllers of SM1 and WS2 reduce the power generation to fulfill the power demand, i.e., $P_{\mathrm{m,sm1}}, P_{\mathrm{m,ws2}} < 1$ at $t = 0$, see subplot 4 of Fig. 20.

In Fig. 20, the load disturbance leads to temporary grid voltage misalignment of the VSM, i.e., $\delta_\mathrm{v} = \phi_\mathrm{p} - \phi_\mathrm{g} \neq 0$ in subplot 2. This disturbs the FTC in (68), i.e., the DFIM torque M_m deviates from its reference $M_{\mathrm{m,ref}}$ in subplot 17 of Fig. 20. However, this is the desired inertia emulation for grid frequency support, i.e., the torque deviation or power pulse counteracts the RoCoF by reducing the power imbalance, see also (6). Note that the temporary misalignment also disturbs the grid voltage control, which, however, yields an acceptable performance, see (R.8), since $|\widehat{U}_\mathrm{g} - 1| > 10\%$ only occurs for less than 1 s in subplot 12 of Fig. 20.

For different chosen inertia constants, Fig. 12 and Table 5 give the inertial response and corresponding initial RoCoFs, respectively. Note that the initial RoCoFs are significantly higher than some average RoCoF (secant) over a longer time window of, e.g., $T = 1$ s after the disturbance. This may also

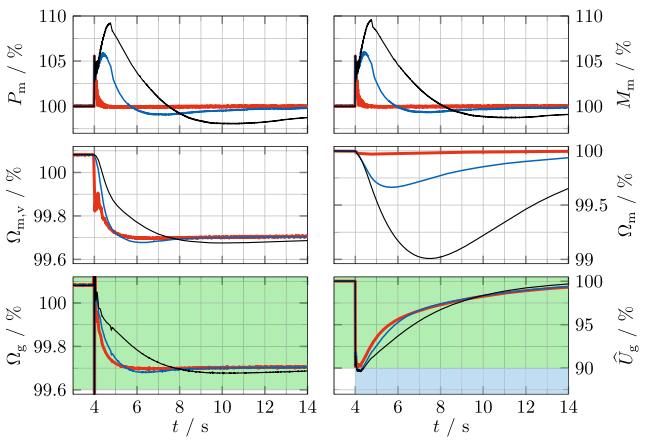

FIGURE 12. Simulation results of scenario SF_1: Load disturbance in WS-dominated power system (see also Table 2 and Fig. 20) with comparison of the inertial response for different VSM/system inertia constants (cf. Table 4): $H_\mathrm{v}/H_\mathrm{sys}$ = 0.1 s/3.45 s [——], 5 s/4.675 s [——], and 25 s/9.675 s [——].

TABLE 5. Simulation results of Scenario SF_1: Comparison of the inertial response to the load disturbance, cf. Table 2, for different VSM/system inertia constants $H_\mathrm{v}/H_\mathrm{sys}$, cf. Fig. 12, with metrics: Initial RoCoF $\dot{\Omega}_{\mathrm{g},0}$, see Remark (R.10), grid frequency deviation nadir $\Delta\Omega_{\mathrm{g,min}} := 1 - \min\{\Omega_\mathrm{g}(t)\}$, WT or DFIM rotor speed deviation nadir $\Delta\Omega_{\mathrm{m,min}} := 1 - \min\{\Omega_\mathrm{m}(t)\}$.

H_v / s	H_sys / s	$\lvert\dot{\Omega}_{\mathrm{g},0}\rvert$ / $\frac{\%}{\mathrm{s}}$	$\Delta\Omega_{\mathrm{g,min}}$ / %	$\Delta\Omega_{\mathrm{m,min}}$ / %
0.1	3.450	0.972 2	0.303 3	0.030 6
5	4.675	0.651 1	0.319 4	0.336 3
25	9.675	0.521 0	0.323 3	0.992 4

be the case in the bulk power system, because local phenomena can be more severe than the global RoCoF [3]. For $H_\mathrm{v} = 25$ s [——] in Fig. 12, a small dip of Ω_g at $t \approx 4.8$ s is visible due to MPPT compensation reset. More precisely, $\Omega_{\mathrm{m},H0}$ is reset to Ω_m at this moment, see also (30)–(32), such that the MPPT rapidly reduces the torque reference $M_{\mathrm{m,ref}}$, similar as in subplots 16 and 17 of Fig. 20 for $H_\mathrm{v} = 5$ s. The resulting abrupt power reduction is notable shortly after the peak of P_m for $H_\mathrm{v} = 25$ s [——] in Fig. 12, which leads to the aforementioned dip of Ω_g. For the smaller VSM inertia constants $H_\mathrm{v} = 5$ s [——] and $H_\mathrm{v} = 0.1$ s [——], this dip is smaller or not visible, since the WT speed deviation is smaller (see Ω_m), and thus, also the effect of the MPPT compensation reset is smaller.

In Table 5, increasing inertia constants lead to less severe RoCoFs but slightly more severe frequency nadir, see $|\dot{\Omega}_{\mathrm{g},0}|$ and $\Delta\Omega_{\mathrm{g,min}}$. The latter is due to more severe MPP deviation, quantified by WT speed deviation, see $\Delta\Omega_{\mathrm{m,min}}$, resulting in reduced power output when the RoCoF vanishes to recover the initial WT speed, see P_m-nadirs in Fig. 12. However, the delay until reaching the grid frequency nadir significantly increases with higher H_v, see Ω_g in Fig. 12, giving grid operators or protection schemes more time to react. Consequently, lower RoCoFs also decrease the requirements for protection

schemes [3], [10], [39]. In conclusion, with higher VSM inertia, the power system inertia increases, which supports the grid frequency due to lower RoCoFs. Nevertheless, H_v should not be chosen too high to avoid high WT speed deviations (see Ω_m in Fig. 12). Note that severe WT speed nadirs imply high MPP deviations (at least for initial MPPT operation), which may also lead to secondary grid frequency drops in the worst case [32], [33].

Finally, the power overload for negative RoCoFs increases with higher H_v (see P_m in Fig. 12), which may be inadmissible. This is less relevant for higher power reserves in RPPT mode, considered in the following scenarios.

2) SF_2—LOSS OF SM IN SM-DOMINATED POWER SYSTEM

In general, like the previously considered load disturbance, the now considered loss of SM1 leads also to a (significant) power imbalance and thus, to a RoCoF. Note that this scenario SF_2 considers the SM-dominated power system like scenario SN_2 (see Table 2). With $P_\mathrm{m,ref,rel} = 95\%$, the RPPT enables droop control for WS1 with power reserves of 5%. Since the WS(1) droop control is only activated outside the normal grid frequency tolerance band, see also (69), an initial grid frequency near its lower band limit is assumed to analyze the WS droop control. Thus, after the loss of SM1, the grid frequency decreases below its lower limit, which activates the WS droop control, see Ω_g and P_m in Fig. 14. The power generation of all GUs (SM1/2+WS1) should equal the total power demand at the desired initial grid frequency deviation $\Delta\Omega_\mathrm{g,0} := 1 - \Omega_\mathrm{g}(0) = 0.4\%$, cf. Remark (R.5). Thus, assuming equal power of both ($n_\mathrm{sm} = 2$) SMs and due to $p_\mathrm{sm,R} = p_\mathrm{ws,R} = -s_\mathrm{b}$, the initial SM power reference is

$$\overbrace{\frac{p_\mathrm{load,R}}{s_\mathrm{b}} + P_\mathrm{b}}^{\text{demand}} \overset{!}{=} \overbrace{n_\mathrm{sm}\left(P_\mathrm{sm,ref,0} + K_\mathrm{d,sm}\Delta\Omega_\mathrm{g,0}\right) + P_\mathrm{m,ref,rel}}^{\text{generation of SMs+WS}}$$
$$\Rightarrow\ P_\mathrm{sm,ref,0} = 50\% \tag{105}$$

with estimated power buffer $P_\mathrm{b} = 20\% = 7.84\%\frac{p_\mathrm{load,R}}{s_\mathrm{b}}$. This buffer is added to the demand side to compensate (or slightly overcompensate) for (i) conversion and transmission losses, and for (ii) deviations between actual p_load and rated load power $p_\mathrm{load,R}$ due to (local) deviations from the rated grid voltage but constant load impedances (see also [2, Table XI]). The initial SM power (see subplot 4 of Figs. 21, 22, and 23)

$$\underset{(106)}{\overset{(102)}{\Rightarrow}} P_\mathrm{sm} = P_\mathrm{sm,ref,0} + K_\mathrm{d,sm}\Delta\Omega_\mathrm{g,0} \approx 90\% \approx 35\%\frac{-p_\mathrm{load,R}}{p_\mathrm{sm,R}}$$

equals the power imbalance induced by the loss of SM1.[22]

After the loss of SM1 at $t_0 = 4$ s, only SM2 stays grid-connected besides the WS. The SM(2) droop response delay depends on the governor time constant T_gov, see (103). Clearly, decreasing T_gov from its default value 5 s in Fig. 21 to 0.5 s in Fig. 22 reduces the system oscillations (as further discussed later in Section IV-E3, see Fig. 14). Moreover, Fig. 23 shows the simulation results for WS control with ssDS (variant ssDS) only, i.e., without additionally proposed dyDS (variant ss/dyDS), see (80). Finally, Fig. 13 and Table 6 compare the droop saturation variants ssDs and ss/dyDS in detail.

In view of Remark (R.1), after the loss of SM1, i.e., for $t \geq t_0$, the SM1 turbine, machine, and reactive power $P_\mathrm{t,sm1}$, $P_\mathrm{m,sm1}$, and Q_sm1 are set to zero for calculating the power sums in subplots 7–9 of Figs. 21, 22, and 23. In other words, SM1 is excluded from the power system consideration, see also Remark (R.1), which is especially relevant for the system RoCoF, see $\dot{\Omega}_\mathrm{sys}$ in subplot 11, calculated based on (6) with the data from subplot 8. Actually, after its disconnection, SM1 continues to generate power for its local load (see, e.g., $P_\mathrm{m,sm1} > 0$ for $t > t_0$ in subplot 4 of Fig. 22), but the islanded operation of SM1 is not relevant for the remaining power system.

In Figs. 22 and 23, due to the high negative RoCoF after the loss of SM1 (subplot 11), the VSM inertial response increases the DFIM torque above its rating, i.e., $\max M_\mathrm{m} > 1$ (subplot 17) for both the droop saturation variants but the dynamics differ as follows. For variant ss/dyDS in Fig. 22, the droop control stays inactive at least for 1 s after the disconnection of SM1, i.e., the ss/dyDS sets $M_\mathrm{t,v} = 0$ (subplot 18), since the WS power P_m (subplot 22) is already above its rating, i.e., no power reserves remain. Afterward, with vanishing RoCoF (subplot 11), the VSM torque $M_\mathrm{m,v}$ decreases while the droop torque $M_\mathrm{t,v}$ increases at $t = 5.3$ s (subplot 18) to keep the DFIM torque M_m (subplot 17) close to its rating. Actually, M_m slightly decreases below its rating to recover rated WT speed, i.e., $M_\mathrm{t,v}$ is saturated to 3.7% at $t = 5.3$ s, before Ω_m (subplot 16) increases to its rated value again and the droop torque approaches its steady-state saturation limit of $M_\mathrm{t,v} = 5\%$ (subplot 18). For variant ssDS (without dyDS) in Fig. 23, the droop control does not take the inertial response into account, i.e., $M_\mathrm{t,v}$ (subplot 18) already increases shortly after the loss of SM1, leading to higher DFIM torques with $\max M_\mathrm{m} = 108.34\%$ (subplot 17 in Fig. 23), instead of $\max M_\mathrm{m} = 107.36\%$ (subplot 17 of Fig. 22). Consequently, the power overloading differs, see P_m-peaks in Fig. 13.

Considering Fig. 13 and Table 6, ss/dyDS slightly increases the initial RoCoF magnitude by 1.25% but slightly decreases the grid frequency deviation nadir by 0.09% compared with ssDS. However, the ss/dyDS significantly improves the WT speed deviation nadir by 27.80%. Thus, the proposed ss/dyDS leads to less severe WS reference operating point deviations while providing similar grid support.

3) SF_3—LOSS OF SM IN WS-DOMINANTED POWER SYSTEM

This scenario considers the same loss of SM1 and the same WS(1) configuration as the previous scenario SF_2, but SM2 is now replaced by WS2 (see also Table 2) with WS2 configuration as in scenario SN_3. The WS2 power reference to reach the desired initial grid frequency deviation $\Delta\Omega_\mathrm{g,0} = 0.4\%$ is

[22]The actual power imbalance is slightly smaller, since the local load of SM1 is also disconnected from the grid after opening switch σ_4 in Fig. 9.

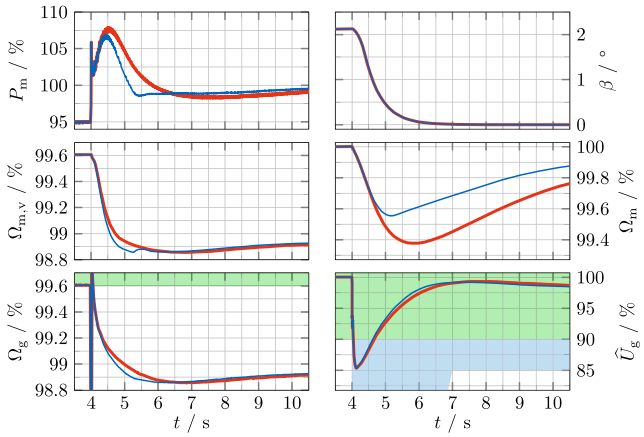

FIGURE 13. Simulation results of scenario SF_2: Loss of SM in SM-dominated power system comparing VSM control with and without dynamic droop saturation (see also Figs. 22 and 23), i.e., for ss/dyDS [——] and ssDS [——] in (80).

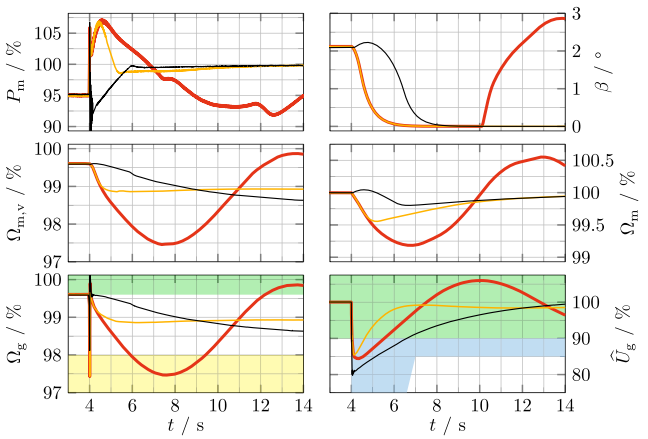

FIGURE 14. Simulation results of scenarios SF_2 and SF_3: Loss of SM with comparison of the inertial response for SM-dominated power system (GU2=SM2) with $T_{gov} = 5$ s [——] (see also Fig. 21) or $T_{gov} = 0.5$ s [——] (see also Fig. 22) and WS-dominated power system (GU2=WS2) [——] (see also Fig. 24).

TABLE 6. Grid frequency response to the loss of SM1 for the different droop saturation variants in (80), see also Fig. 13: Comparison of the initial RoCoF $\dot{\Omega}_{g,0}$, see also (R.10), the grid frequency deviation nadir $\Delta\Omega_{g,min} := 1 - \min\{\Omega_g(t)\}$, and the WT or DFIM rotor speed deviation nadir $\Delta\Omega_{m,min} := 1 - \min\{\Omega_m(t)\}$.

Variant	$\lvert\dot{\Omega}_{g,0}\rvert$ / $\frac{\%}{s}$	$\Delta\Omega_{g,min}$ / %	$\Delta\Omega_{m,min}$ / %
DS	1.578 1	1.142 4	0.622 4
ss/dyDS	1.597 8	1.141 4	0.449 4

chosen analogously to (105), but WS2 replaces SM2, i.e.,

$$\overbrace{\frac{p_{\text{load,R}}}{s_b} + P_b}^{\text{demand}} \overset{!}{=} \overbrace{P_{\text{sm,ref},0} + K_{\text{d,sm}}\Delta\Omega_{g,0} + P_{\text{m,ref,rel}}}^{\text{generation of SM1+WS1}} + \underbrace{P_{\text{m,ref,rel},2}\left(1 + K_{\text{d},2}\Delta\Omega_{g,0}\right)\frac{p_{\text{ws2,R}}}{-s_b}}_{\text{generation of WS2}}$$

$$\Rightarrow P_{\text{m,ref,rel},2} = 34.65\% = 69.31\%\frac{-s_b}{p_{\text{ws2,R}}} \tag{106}$$

with $P_{\text{sm,ref},0} = 50\%$ for SM1 as in (105) and buffer power $P_b = 27\% = 10.6\%\frac{p_{\text{load,R}}}{s_b}$.[23] In (106), the WS2 droop gain equals the one of SM1, i.e., $K_{\text{d},2} := k_{\text{d},2}\omega_{g,R} = K_{\text{d,sm}}$, and the factor $\frac{p_{\text{ws2,R}}}{-s_b} = 2$ is required for correct WS2 scaling, since the WS2 power rating is twice the power rating of the other GUs SM1 and WS1. Note that the SM(1) and WS2 droop control differ regarding their power references. The SM droop power $K_{\text{d,sm}}\Delta\Omega_{g,0}$ refers to its rated power $\frac{p_{\text{sm,R}}}{-s_b} = 1$, whereas the WS2 droop power refers to its relative power reference $P_{\text{m,ref,rel},2} < 1$, see (102) and (69). Thus, the final grid frequency nadir for the WS-dominated power system in subplot 10 of Fig. 24 is lower than for the SM-dominated power system in subplot 10 of Fig. 22. Clearly, more aggressive tuning, i.e., increasing $K_{\text{d},2}$, would increase the grid frequency nadir. Alternatively, the droop control definition may be unified. However, this difference is not relevant for the following qualitative comparison of the transient behavior during the inertial response.

Fig. 14 compares the response to the loss of SM for different configurations. The SM-dominated power system (scenario SF_2) with default governor time delay $T_{gov} = 5$ s [——] leads to significantly higher deviations in grid frequency Ω_g and WT speed Ω_m than for the WS-dominated power system [——]. Although $T_{gov} = 0.5$ s [——] shows significantly improved performance compared with $T_{gov} = 5$ s, reducing T_{gov} may be impossible in reality due to slow SM turbine dynamics. Instead, for the WS-dominated power system, the inverters do not induce any significant droop control delay such that no grid frequency oscillations occur (see subplot 10 of Fig. 24). The RoCoF (subplot 11 of Fig. 24) is significantly smaller for the WS-dominated power system, even compared with the SM-dominated power system with $T_{gov} = 0.5$ s (see subplot 11 of Fig. 22). This is due to (i) a higher system inertia $H_{sys} = 5$ s of the WS-dominated or VSM-dominated power system compared with $H_{sys} = 4.35$ s of the SM-dominated power system (see Table 4) and due to (ii) a much higher system damping induced by the VSMs with a higher damping and a faster droop control compared with the SMs.

The RoCoF is so small for the WS-dominated power system, that, except for the transients in the first 100 ms after the loss of SM1 at $t_0 = 4$ s, there are no power overshoots above the power rating, see P_m [——] in Fig. 14. Consequently, the WT speed nadir (see Ω_m [——] in Fig. 14) is less severe compared with the SM-dominated power system [——] and [——]. The grid voltage recovery process is slower for the WS-dominated power system than for the

[23] The buffer power P_b increased compared with (105) to compensate for higher losses, e.g., since WS2 requires additional LV/MV transformers.

SM-dominated power system (see $\widehat{U}_g$ in Fig. 14), but the voltage control performance is acceptable, since $\widehat{U}_g$ [——] stays within the admissible range [ ] and returns to the normal operation range [ ] within less than 3 s, see also Remark (R.8).

4) SF_4—LOAD DISTURBANCE IN WS-BASED POWER SYSTEM

After the loss of SM in the previous scenario SF_3, no SM stays grid-connected. This scenario SF_4 considers the same load step as in scenario SF_1 but for 100% renewable power generation by WSs (WS1/2) only. A higher WS scaling factor of $n_{wu} = 40$ (instead of $n_{wu} = 20$ previously) compensates for the missing SM power generation and provides sufficient power reserves for the load disturbance, see also Table 2. The relative power reference for WS1 and WS2 are set to $P_{m,ref,rel} = 77.5\%$ and $P_{m,ref,rel,2} = 50\%$, respectively, which leads to a below rated initial grid frequency, see subplot 10 in Fig. 25. This is desirable for the following discussion, since the DUT/WS1 droop control is only activated outside the grid frequency tolerance band, see also (69), i.e., the initial grid frequency deviation leads to faster droop control activation after the load disturbance.

Again, the DUT/WS1 quantities, as shown in subplots 13–24 [ ] of Fig. 25, are normalized w.r.t. rated values, e.g., the initial machine power is $P_m = 77.5\%$ in subplot 22 w.r.t. the rated WS power $p_{ws,R}$. Note that $p_{ws,R} = n_{wu} p_{m,R} = -2 s_b$ changed by the factor two compared with the previous scenarios. This factor has to be taken into account when considering the power system subplots 1–12 [ ] of Fig. 25, as the WS power quantities are normalized w.r.t. $-s_b$. For instance, the sum of the initial WS1/2 machine power (subplots 1 and 4) equals the initial aggregated machine power (subplot 7), i.e., $P_{m,agg} = P_{m,ws1} + P_{m,ws2} = 2 \cdot (77.5\% + 60\%) = 155\% + 120\% = 275\%$.

In Fig. 25, after the load step at $t_0 = 4$ s, the RoCoF is only limited by the inertial response and droop control response of the VSMs. Before $\Omega_{m,v,ws1}$ decreases below the tolerance band [ ] at $t \approx 5.7$ s in subplot 10, only the WS2 droop control is active, i.e., $M_{t,v} = 0$ for the VSM of WS1, see subplot 18. Afterward, the active WS1 droop control increases $M_{t,v}$, and, with vanishing RoCoFs, the VSM torque $M_{m,v}$ converges to $M_{t,v}$ (subplot 18). Clearly, the WSs are capable of compensating for the load disturbance and the power system reaches a new equilibrium point for $t \geq 24$ s. Thus, the proposed VSM control enables stable islanded operation if the available wind power reserves are high enough. If not, the power demand may be reduced (e.g., by load shedding) to avoid a total blackout [4].

Note that for the SM-dominated power system (scenario SF_1), the RoCoF magnitude was maximal immediately after the load disturbance at $t_0 = 4$ s (see subplots 10 and 11 in Fig. 20). The corresponding initial RoCoF was $\dot{\Omega}_{g,0} = -0.651 \frac{\%}{s}$, recall also (R.10). For the (purely) WS-based power system (scenario SF_4), the initial RoCoF for the same load disturbance is (slightly) positive, i.e., $\dot{\Omega}_{g,0} = 0.148 \frac{\%}{s}$, before $\dot{\Omega}_g$ rapidly decreases below zero such that Ω_g begins to decrease (see subplots 10 and 11 in Fig. 25). The minimal RoCoF of $\min \dot{\Omega}_g = -0.155 \frac{\%}{s}$ for scenario SF_4 is reached $t \approx 5.5$ s, i.e., approximately 1.5 s after the disturbance (see subplot 11 in Fig. 25). Besides, for scenario SF_1, the SM droop control delay led to a negative overshoot of Ω_g (see subplot 10 in Fig. 20), which does not occur for the highly damped WS-based power system in this scenario SF_4 (see subplot 10 in Fig. 25). In conclusion, the WS-based power system (SF_4) leads to less severe RoCoFs compared with the SM-dominated power system (SF_1) due to (i) higher system inertia (see Table 4) and due to (ii) higher system damping. This is achieved by the following improvements of VSMs compared with SMs: (i) higher (virtual) inertia constants are possible (see Table 4) and (ii) higher damping ratios can be realized by internal damping, see (65), and by fast droop control, see Remark (R.6).

V. CONCLUSION

For the bulk power system with centralized generation and negligible penetration of IBRs, the grid connection of an IBR (here of the considered WS) can be approximated by an infinite bus. However, for the future power system with distributed generation, the interactions with the (micro)grid and its GUs (here WSs and SMs) have to be taken into account. For instance, in contrast to the proposed VSM (GFM) control, the standard GFL control tends to instability with increasing WS power penetration.

The proposed VSM control with FTC achieves nearly the same MPPT performance as standard GFL control, and the torque synchronization loop of the proposed freely spinning VSM compensates for possible FTC simplification errors during normal operation; whereas, for VSM control without FTC, the torque is fully controlled by the VSM, i.e., fast synchronization with low VSM inertia could achieve fast MPPT but reduces the grid frequency support. Thus, a compromise between WS efficiency and grid stability has to be found for existing VSM control without FTC.

A power imbalance, e.g., induced by a wind change or grid fault, is distributed to all (virtual) rotating masses of the (V)SMs in the power system, before the droop controllers activate power reserves and set the new steady-state power share. With the proposed FTC, the power sharing dynamics are significantly faster than without FTC. In other words, the FTC leads to a faster communication of power reference changes to other power-sharing partners via the grid frequency. For instance, for a wind speed change, the proposed FTC leads to faster MPPT and thus, higher renewable energy yield. Besides, this results in decreased power or torque oscillations and less pitch actuation in WSs. Moreover, for a grid fault, the proposed MPPT compensation achieves accurate inertia

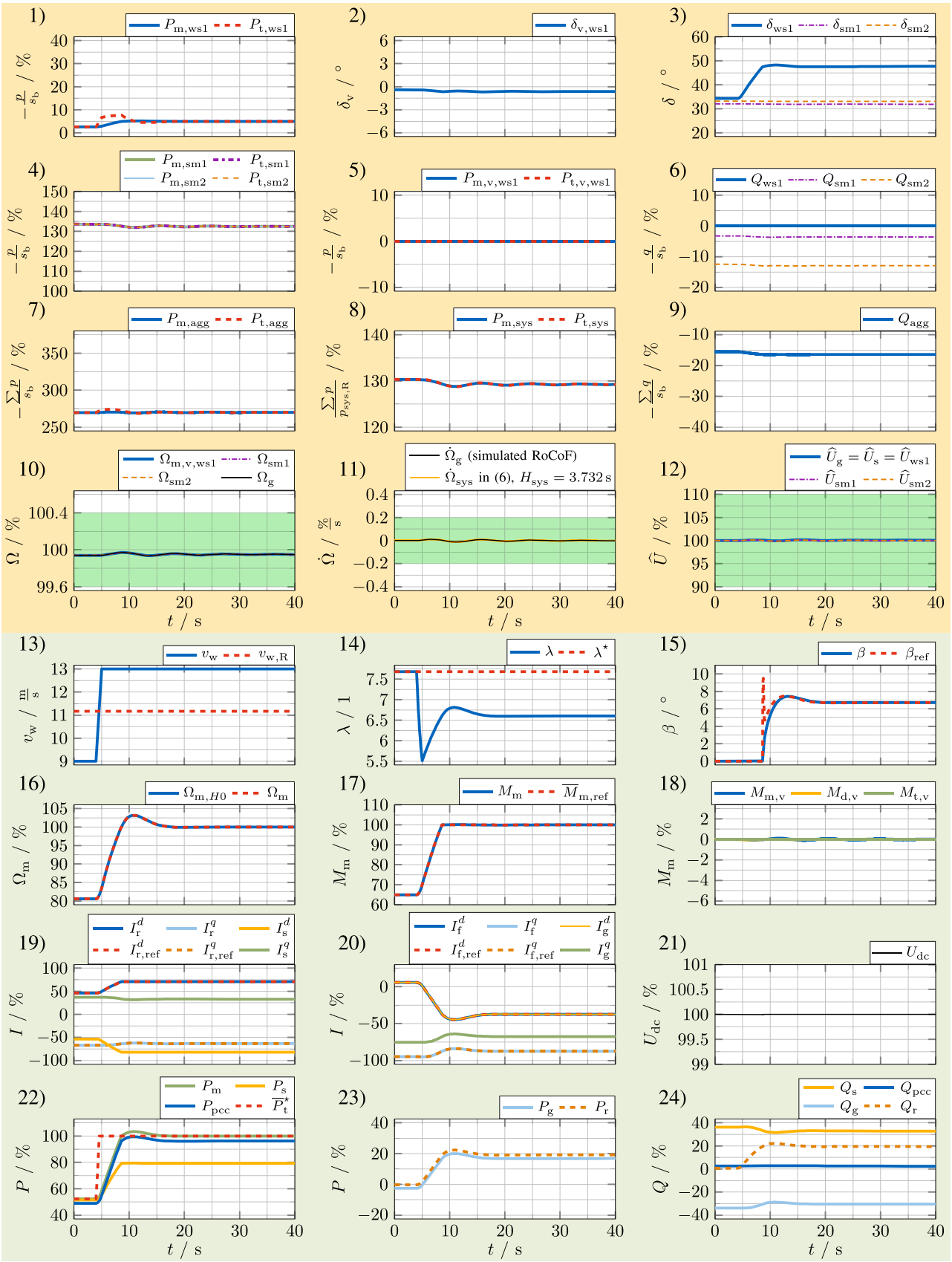

FIGURE 15. Simulation results of scenario SN_1: MPPT in bulk power system with FTC (Power system [ ] and DUT/WS1 [ ]).

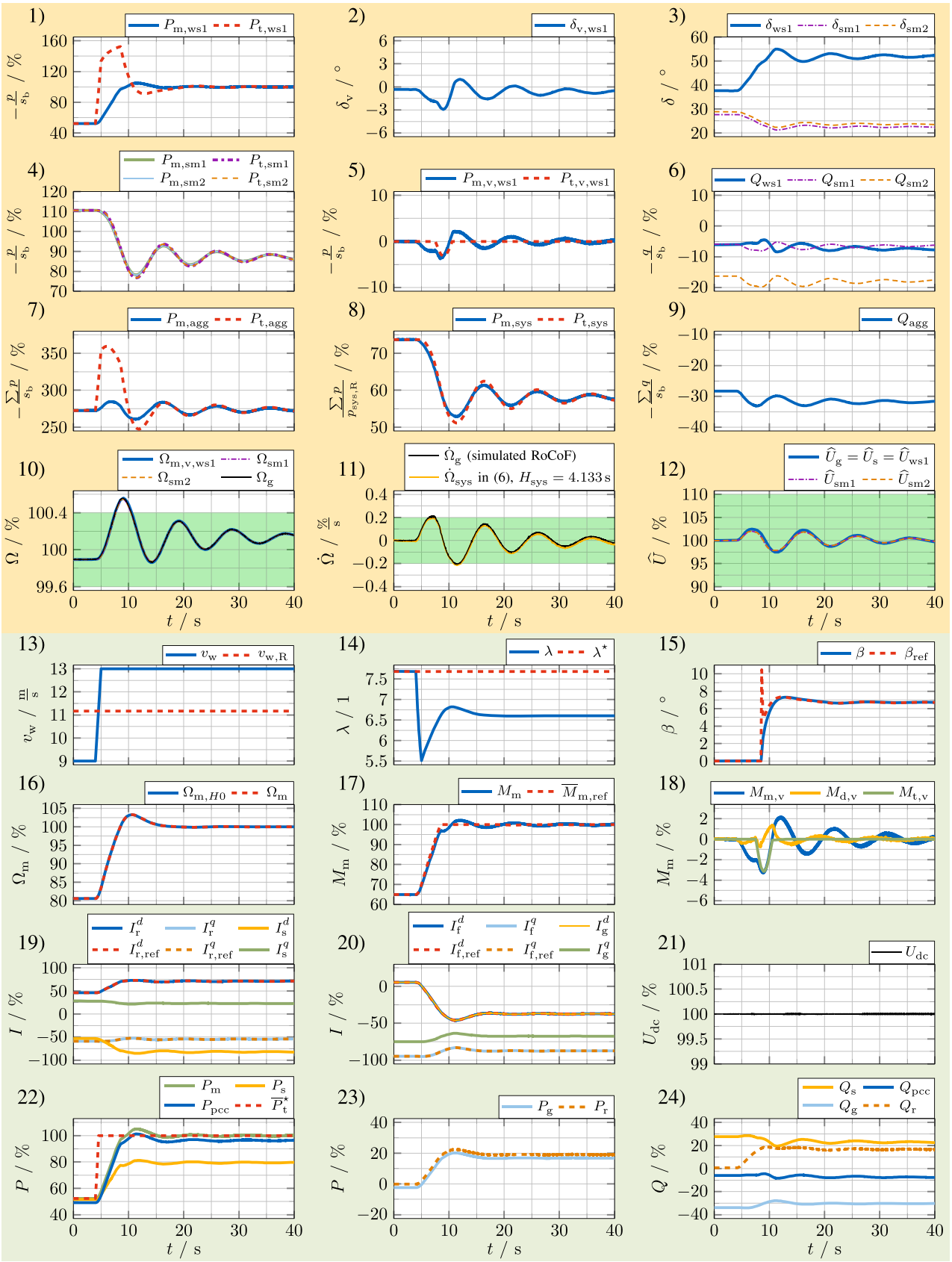

FIGURE 16. Simulation results of Scenario SN_2: MPPT in SM-dominated power system with FTC (Power system [ ] and DUT/WS1 [ ]).

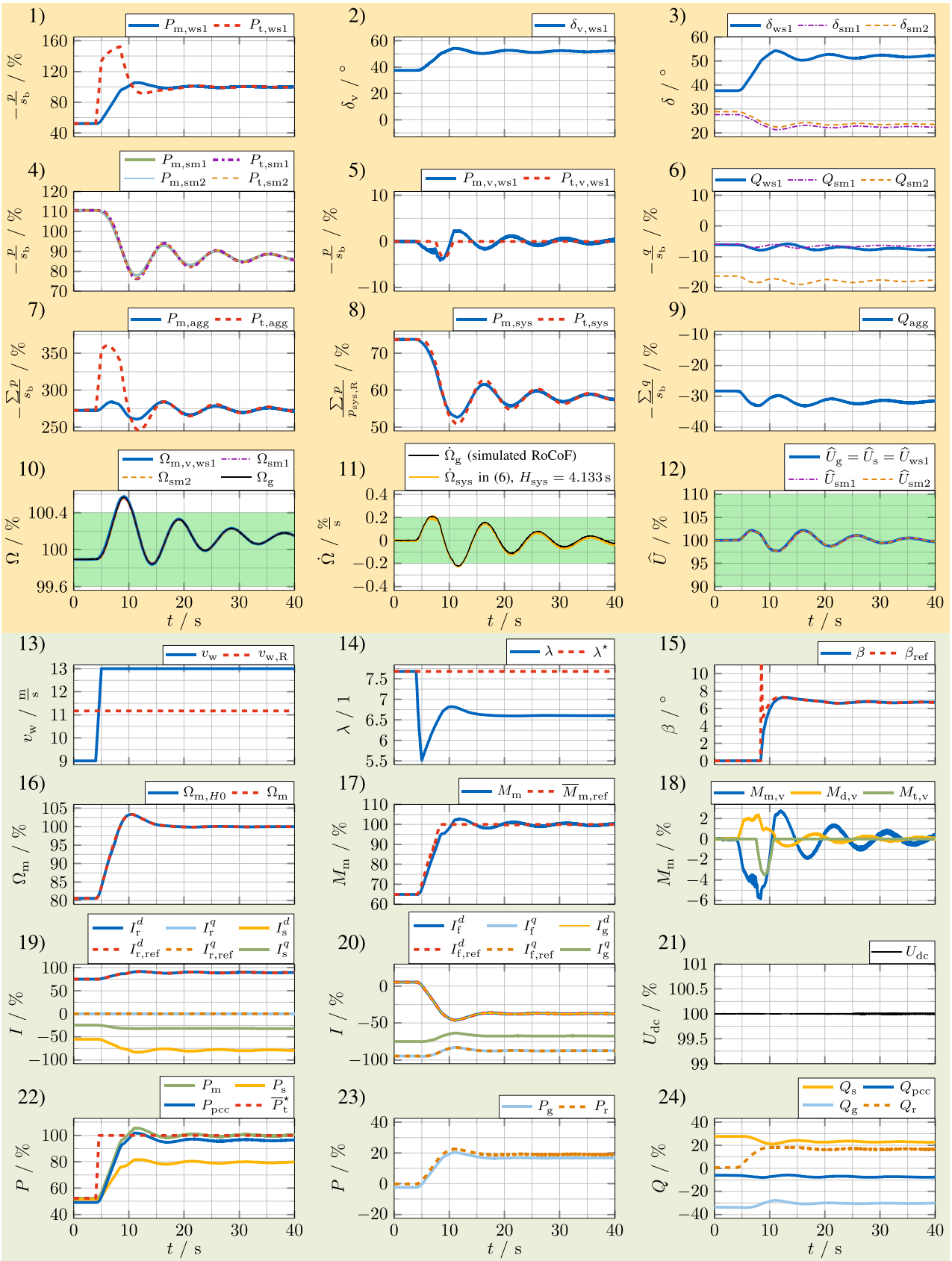

FIGURE 17. Simulation results of scenario SN_2: MPPT in SM-dominated power system without FTC (Power system [ ] and DUT/WS1 [ ]).

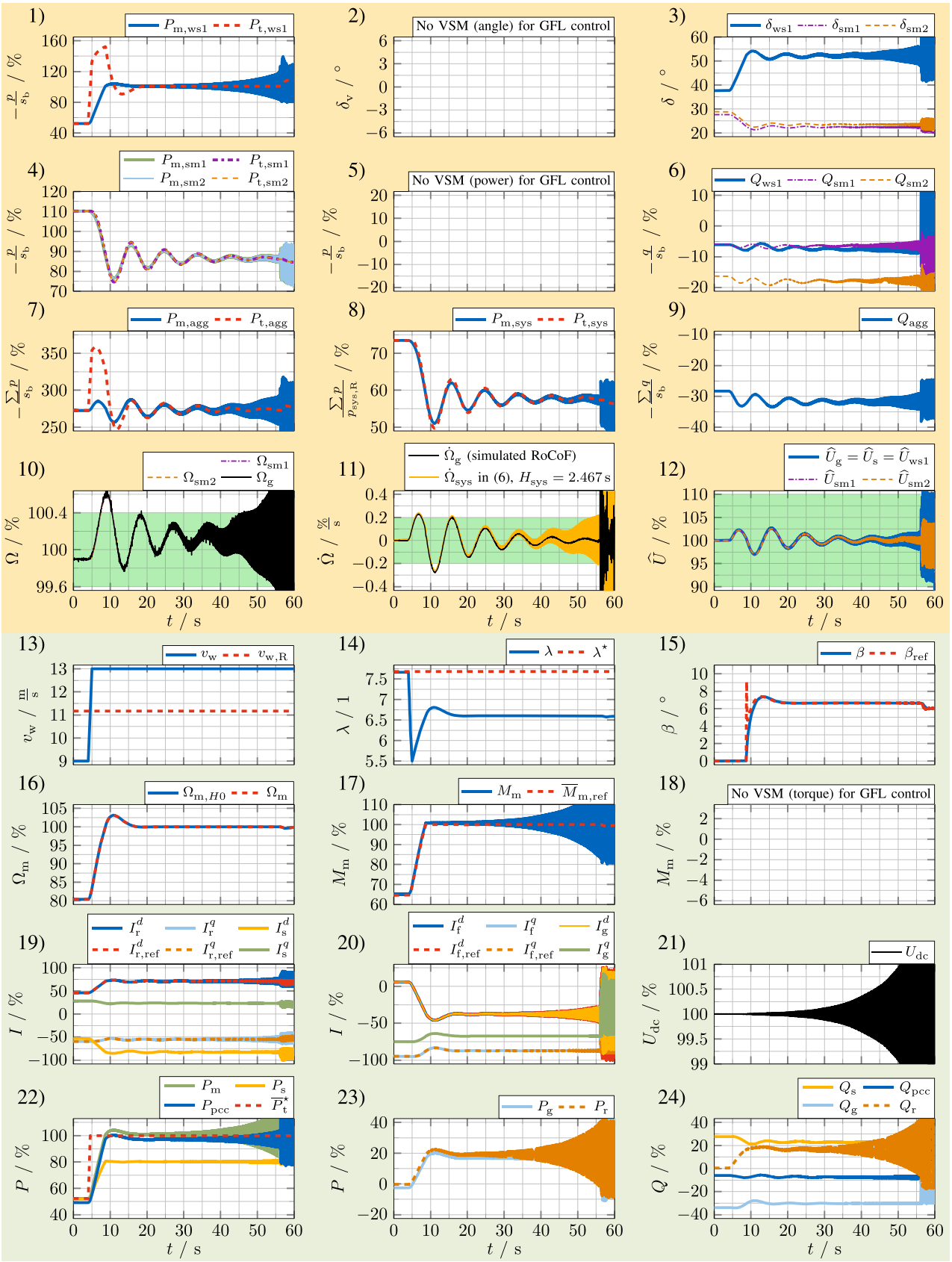

FIGURE 18. Simulation results of scenario SN_2: MPPT in SM-dominated power system with GFL control (Power system [ ] and DUT/WS1 [ ]).

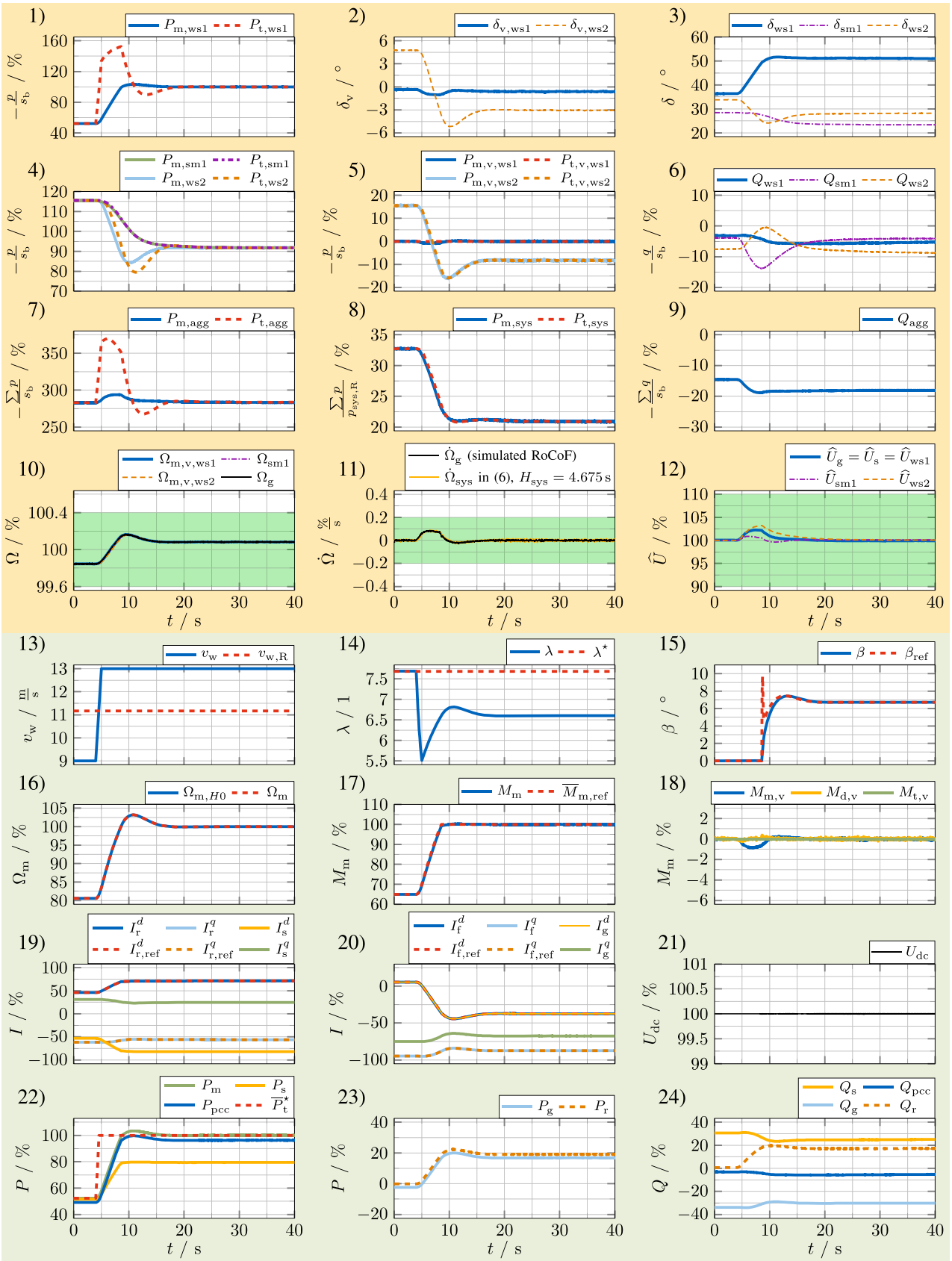

FIGURE 19. Simulation results of scenario SN_3: MPPT in WS-dominated power system with FTC (Power system [ ] and DUT/WS1 [ ]).

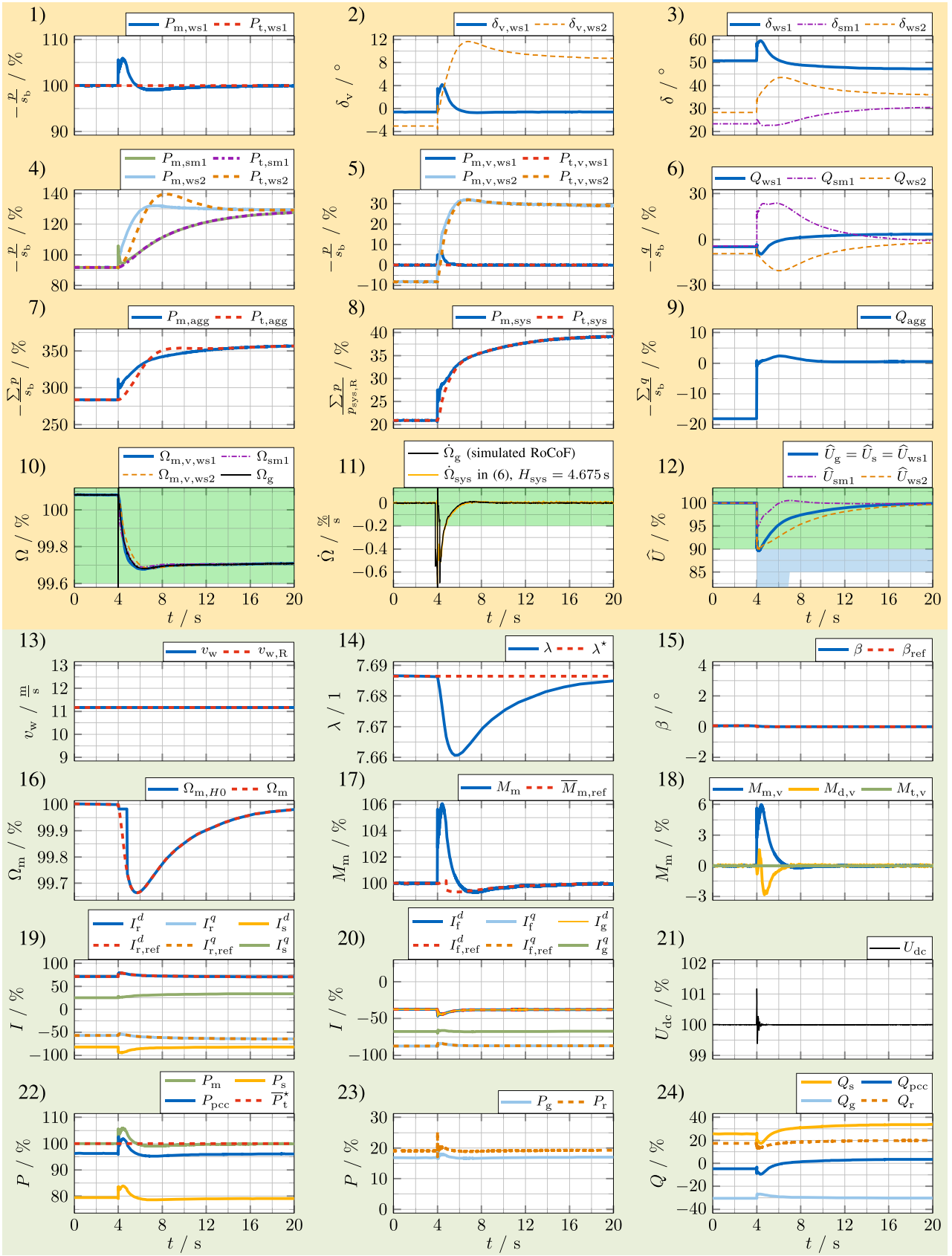

FIGURE 20. Simulation results of scenario SF_1: Load disturbance in WS-dominated power system (Power system [ ] and DUT/WS1 [ ]).

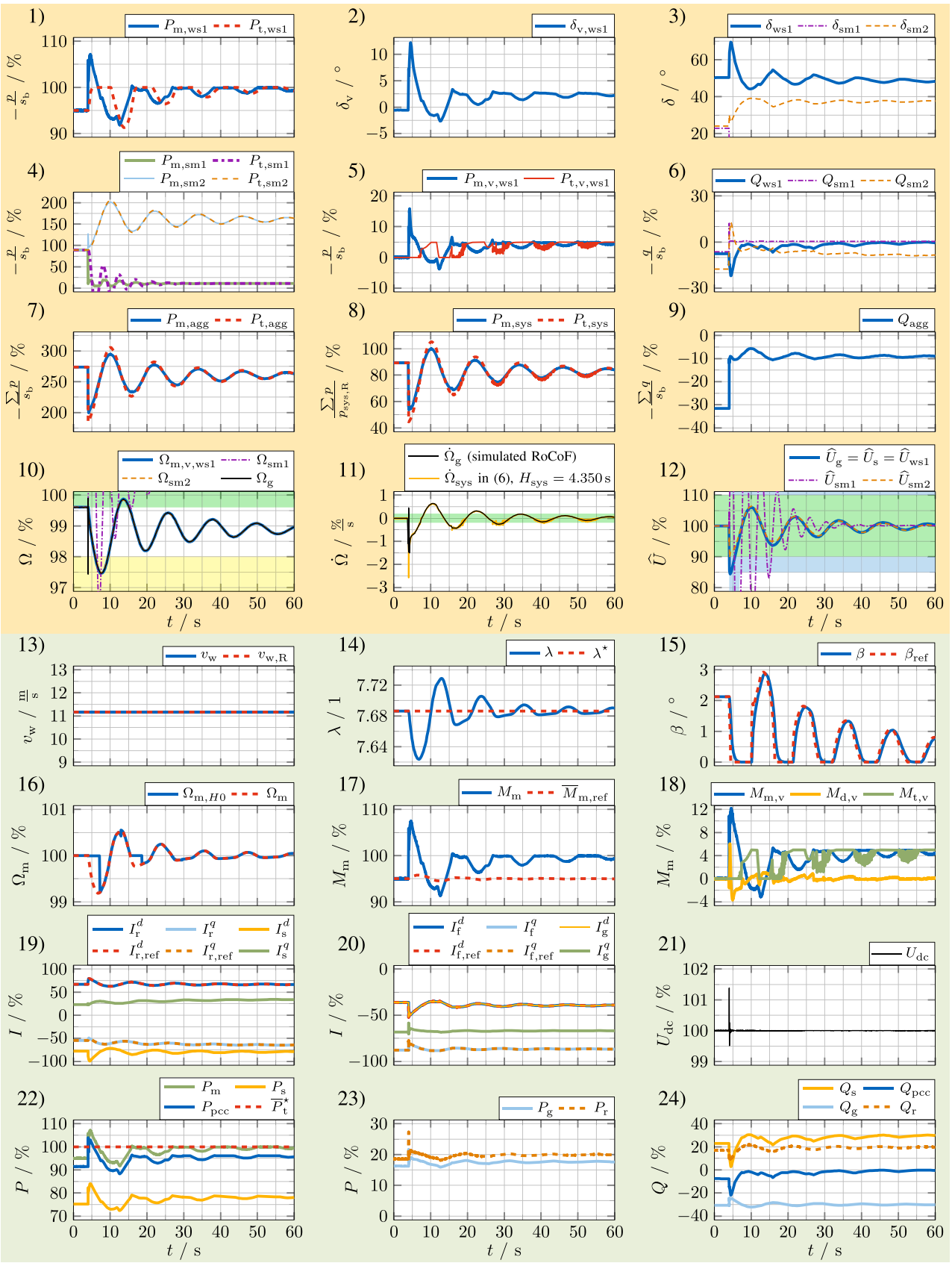

FIGURE 21. Simulation results of scenario SF_2: Loss of SM in SM-dominated power system with $T_{gov} = 5s$ (Power system [ ] and DUT/WS1 [ ]).

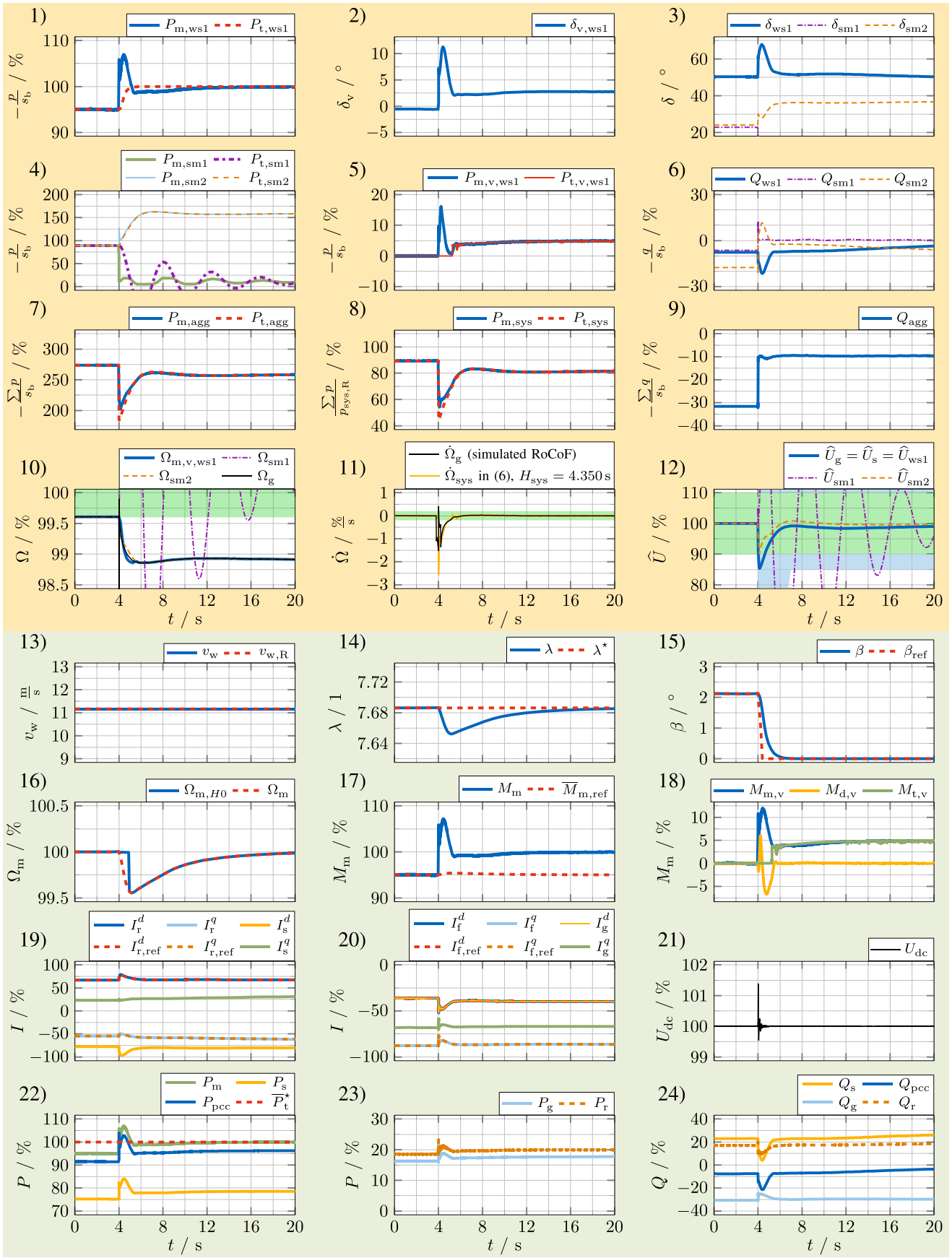

FIGURE 22. Simulation results of scenario SF_2: Loss of SM in SM-dominated power system with $T_{gov} = 0.5s$ (Power system [ ] and DUT/WS1 [ ]).

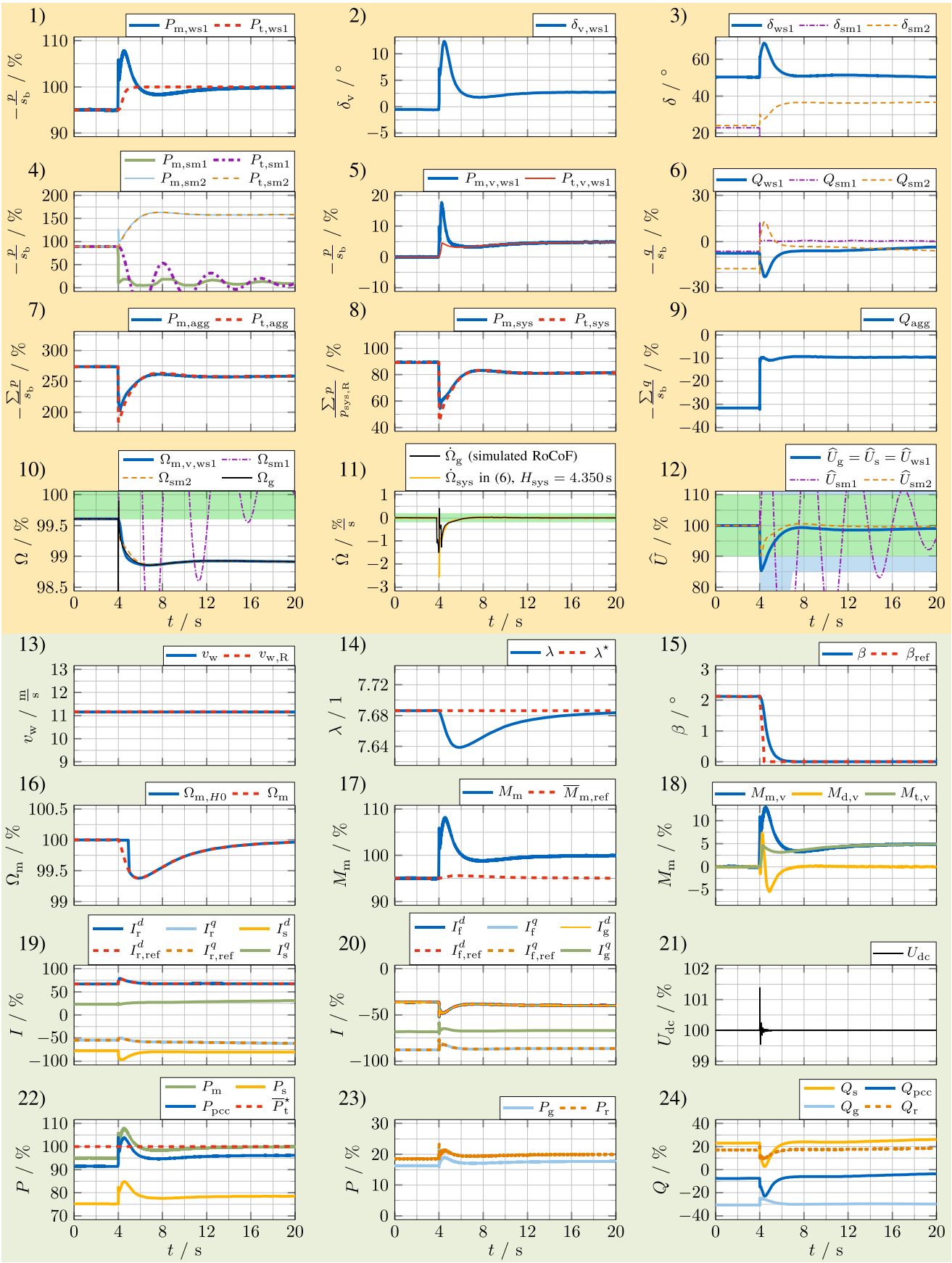

FIGURE 23. Simulation results of scenario SF_2: Loss of SM in SM-dominated power system as in Fig. 22 but without dynamic droop saturation, i.e., for ssDS in (80).

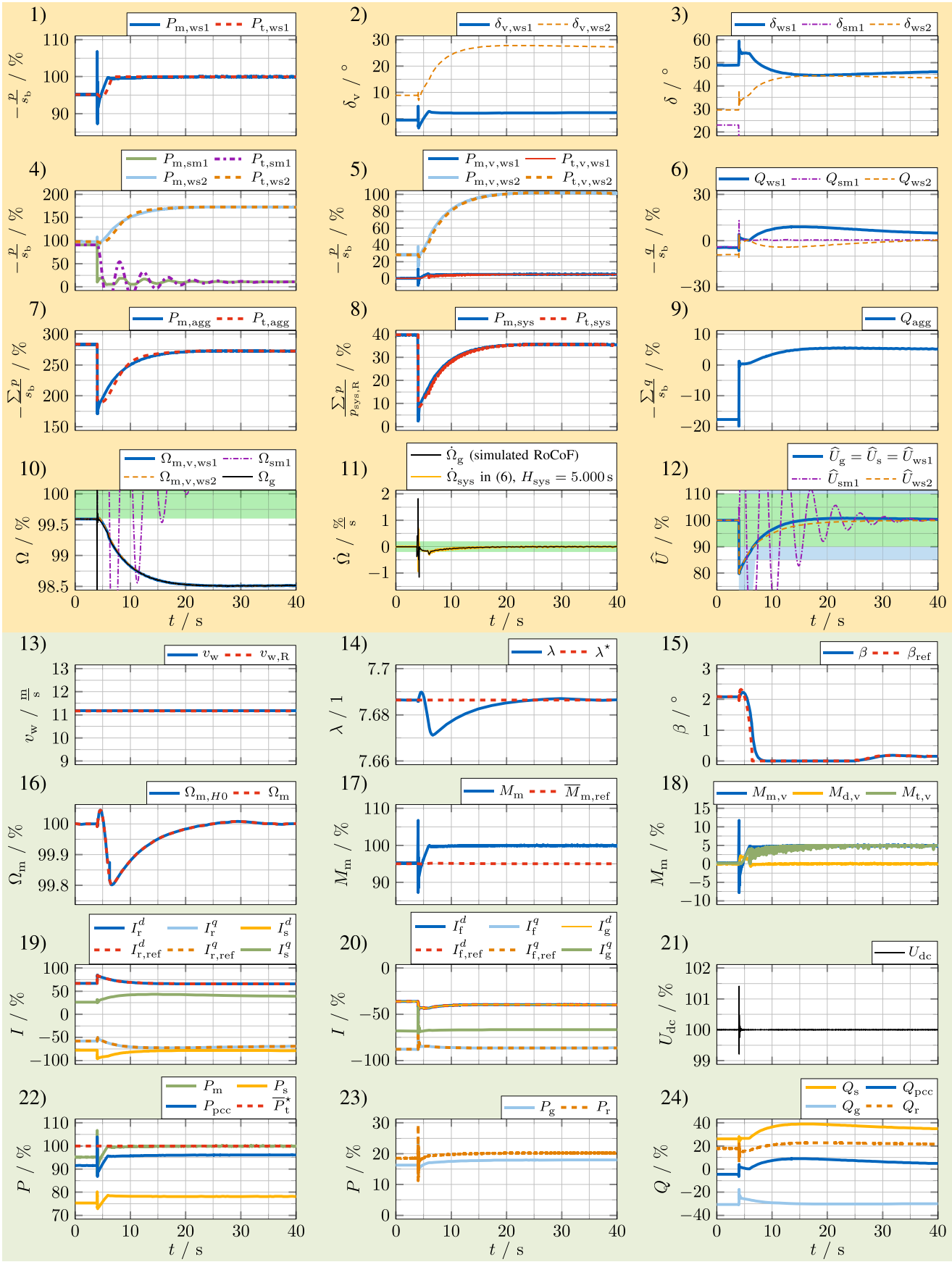

FIGURE 24. Simulation results of scenario SF_3: Loss of SM in WS-dominanted power system (Power system [ ] and DUT/WS1 [ ]).

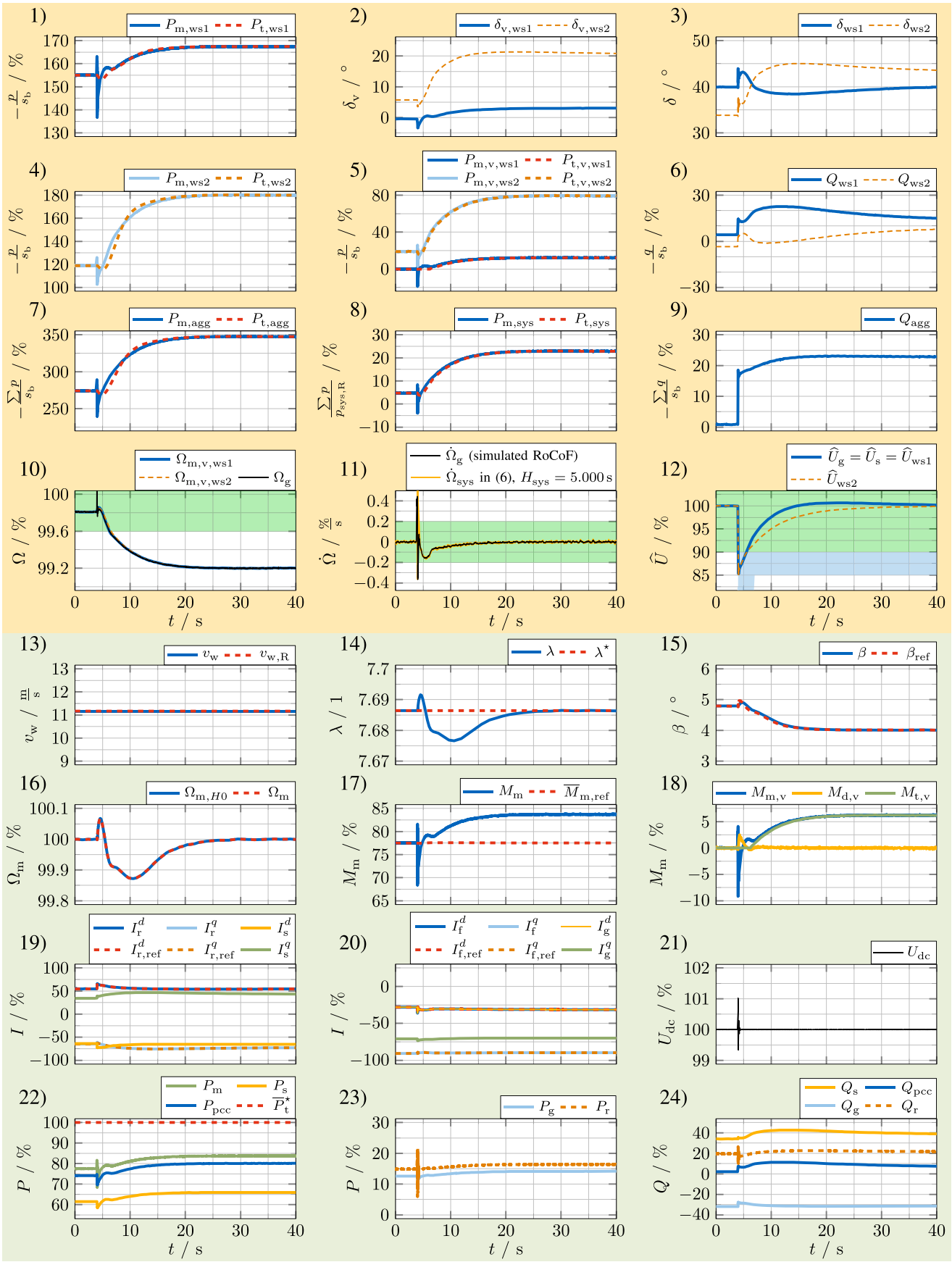

FIGURE 25. Simulation results of scenario SF_4: Load disturbance in WS-based power system (Power system [ ] and DUT/WS1 [ ]).

emulation such that the WS provides the expected VSM inertial power share.

Increasing the VSM inertia supports the grid frequency stability due to lower RoCoFs. Nevertheless, for WSs, the VSM inertia should not be chosen too high to avoid severe power overshoots and WT speed deviations. The only way to increase the output power of a real, directly grid-connected SM is to increase the mechanical power of its turbine, i.e., the SM active droop power response depends on the turbine dynamics. In contrast to that, the VSM control can increase the power of its virtual turbine without mechanical delay, such that the VSM active droop power response is significantly faster than for real SMs. Actually, the fast VSM droop response superposes the VSM inertial response almost instantaneously, which may lead to high power or torque overshoots and thus, severe WT speed deviations for existing VSM control methods in literature. However, the proposed overload protection ss/dyDS limits the droop power to the physically available power reserves during the inertial response. Thus, the proposed control avoids undesired superpositions of inertial and droop responses, while providing similar grid frequency support.

The simulation results show that DFIM-based WSs can achieve 100% renewable power generation with the proposed VSM control. The proposed VSM damping gain adaption achieves critical damping ($\zeta_v = 1$) for the inertial response to RoCoFs, or even higher damping ($\zeta_v > 1$) for active droop control, see Remark (R.6). In contrast to that, the inertial response of a real SM with damper windings depends on the machine design and the operating point, but usually cannot achieve critical damping, i.e., $\zeta_v < 1$ [18]. Consequently, the proposed VSM provides higher power system damping than a real SM. Actually, with VSMs only, i.e., without SMs, the power system damping is sufficiently high to avoid any power or grid frequency overshoots and oscillations (neglecting the transients in the first few 10 ms after a fault). Thus, the overload capability requirements for IBRs with GFM control may even be weakened for future power systems without any directly grid-connected SMs.

Future work will also consider the transients in the first few 10 ms after a fault in detail. Future simulations will include other types of faults, such as asymmetrical faults, and will include the response of protection devices. Moreover, future work will validate methods for protection of VSM-controlled WSs, such as WT speed protection and overload protection. For instance, the VSM overload protection proposed in [28] ensures grid synchronization for ideal RoCoF events, but future work must also take grid interactions into account. For WS power overload protection, the proposed ss/dyDS control may be extended, e.g., by allowing this control to counteract not only the droop but also the inertial response when reaching the power limit. Finally, a thorough analysis of the GFM capability of WSs is desirable, which additionally considers operating limits, such as power, torque, and WT speed limits, in order to ease monitoring and forecasting grid stability of future power systems.

ACKNOWLEDGMENT

The authors would like to thank Abhinav Anand (Chair of Wind Energy, TUM School of Engineering and Design, Technical University of Munich) for simulating and providing the WS aerodynamics to obtain the data for Fig. 2.

REFERENCES

[1] C. M. Hackl, *Non-Identifier Based Adaptive Control in Mechatronics: Theory and Application.*, Berlin, Germany: Springer International Publishing, 2017. [Online]. Available: http://www.springer.com/de/book/9783319550343

[2] A. Thommessen and C. Hackl, "Virtual synchronous machine control for doubly-fed induction machine based wind energy conversion systems [long version]," *IEEE TechRxiv*, 2023. [Online]. Available: https://www.techrxiv.org/articles/preprint/Virtual_synchronous_machine_control_for_doubly-fed_induction_machine_based_wind_energy_conversion_systems_long_version_/24418215

[3] *ENTSO-E Project Inertia Team*, "Frequency stability in long-term scenarios and relevant requirements," 2021. [Online]. Available: https://eepublicdownloads.azureedge.net/clean-documents/Publications/ENTSO-Egeneralpublications/211203_Long_term_frequency_stability_scenarios_for_publication.pdf

[4] ENTSO-E RG-CE System Protection & Dynamics Sub Group, "Frequency stability evaluation criteria for the synchronous zone of continental Europe," 2016. [Online]. Available: https://docs.entsoe.eu/tl/dataset/inertia-report-continental-europe/resource/148d6b97-4fb9-4eaa-8977-124e581ddd1c

[5] X. Wang, M. G. Taul, H. Wu, Y. Liao, F. Blaabjerg, and L. Harnefors, "Grid-synchronization stability of converter-based resources—An overview," *IEEE Open J. Ind. Appl.*, vol. 1, pp. 115–134, 2020, doi: 10.1109/ojia.2020.3020392.

[6] C. Hackl, C. Dirscherl, and K. Schechner, "Modellierung und Regelung von Windkraftanlagen (see URL below for the English translation)," in *Elektrische Antriebe – Regelung von Antriebssystemen*, Berlin, Germany: Springer-Verlag, 2020, ch. 10.3, pp. 1504–1585. [Online]. Available: https://arxiv.org/abs/1703.08661

[7] C. M. Hackl and M. Landerer, "Modified second-order generalized integrators with modified frequency locked loop for fast harmonics estimation of distorted single-phase signals," *IEEE Trans. Power Electron.*, vol. 35, no. 3, pp. 3298–3309, Mar. 2020, doi: 10.1109/TPEL.2019.2932790.

[8] C. M. Hackl and M. Landerer, "A unified method for generic signal parameter estimation of arbitrarily distorted single-phase grids with dc-offset," *IEEE Open J. Ind. Electon. Soc.*, vol. 1, pp. 235–246, 2020, doi: 10.1109/OJIES.2020.3017379.

[9] ESIG high share of inverter-based generation task force, "Grid-forming technology in energy systems integration," Mar. 2022. [Online]. Available: https://www.esig.energy/wp-content/uploads/2022/03/ESIG-GFM-report-2022.pdf

[10] Australian Energy Market Commission, "Final report - system security market frameworks review," 2017. [Online]. Available: https://www.aemc.gov.au/sites/default/files/content/f510069a-791b-4e4d-8bc0-9e6a216be7a2/System-Security-Market-Frameworks-Review-Final-Report.pdf

[11] E. Bossanyi, S. D'Arco, L. Lu, A. Madariaga, W. de Bour, and W. Schoot, "Control algorithms for primary frequency and voltage support (D4.1)," in *TotalControl - Adv. integr. supervisory and wind turbine control for optimal operation of large Wind Power Plants*, 2020. [Online]. Available: https://www.totalcontrolproject.eu/dissemination-activities/public-deliverables

[12] A. Tayyebi, D. Gross, A. Anta, F. Kupzog, and F. Dorfler, "Frequency stability of synchronous machines and grid-forming power converters," *IEEE Trans. Emerg. Sel. Topics Power Electron.*, vol. 8, no. 2, pp. 1004–1018, Jun. 2020, doi: 10.1109/jestpe.2020.2966524.

[13] J. Polleflet, "15 - Applications of power electronics," in *Power Electron.*, Cambridge, MA, USA: Academic Press, 2018, pp. 15.1–15.44. [Online]. Available: https://www.sciencedirect.com/science/article/pii/B9780128146439500155

[14] C. M. Hackl, P. Jané-Soneira, M. Pfeifer, K. Schechner, and S. Hohmann, "Full- and reduced-order state-space modeling of wind turbine systems with permanent magnet synchronous generator," *Energies*, vol. 11, no. 7, 2018, Art. no. 1809. [Online]. Available:, http://www.mdpi.com/1996-1073/11/7/1809
[15] C. Dirscherl and C. M. Hackl, "Dynamic power flow in wind turbine systems with doubly-fed induction generator," in *Proc. IEEE Int. Energy Conf.*, Leuven, Beglium, 2016, pp. 1–6, doi: 10.1109/ENERGYCON.2016.7514104.
[16] J. L. Rodriguez-Amenedo, S. A. Gomez, J. C. Martinez, and J. Alonso-Martinez, "Black-start capability of DFIG wind turbines through a grid-forming control based on the rotor flux orientation," *IEEE Access*, vol. 9, pp. 142910–142924, 2021, doi: 10.1109/access.2021.3120478.
[17] R. H. Lasseter, Z. Chen, and D. Pattabiraman, "Grid-forming inverters: A critical asset for the power grid," *IEEE Trans. Emerg. Sel. Topics Power Electron.*, vol. 8, no. 2, pp. 925–935, Jun. 2020, doi: 10.1109/JESTPE.2019.2959271.
[18] A. Roscoe et al., "Response of a grid forming wind farm to system events, and the impact of external and internal damping," *IET Renew. Power Gener.*, vol. 14, no. 19, pp. 3908–3917, Dec. 2020, doi: 10.1049/iet-rpg.2020.0638.
[19] Z. Shuai, C. Shen, X. Liu, Z. Li, and Z. J. Shen, "Transient angle stability of virtual synchronous generators using Lyapunov's direct method," *IEEE Trans. Smart Grid*, vol. 10, no. 4, pp. 4648–4661, Jul. 2019, doi: 10.1109/tsg.2018.2866122.
[20] L. Huang, H. Xin, L. Zhang, Z. Wang, K. Wu, and H. Wang, "Synchronization and frequency regulation of DFIG-based wind turbine generators with synchronized control," *IEEE Trans. Energy Convers.*, vol. 32, no. 3, pp. 1251–1262, Sep. 2017, doi: 10.1109/tec.2017.2675480.
[21] W. Du and R. H. Lasseter, "Overload mitigation control of droop-controlled grid-forming sources in a microgrid," in *Proc. IEEE Power Energy Soc. Gen. Meeting*, 2017, pp. 1–5, doi: 10.1109/pesgm.2017.8274300.
[22] T.-T. Nguyen, T. Vu, S. Paudyal, F. Blaabjerg, and T. L. Vu, "Grid-forming inverter-based wind turbine generators: Comprehensive review, comparative analysis, and recommendations," 2022. [Online]. Available: https://arxiv.org/abs/2203.02105
[23] A. Meseguer Urban, M. de Battista, H. G. Svendsen, S. D'Arco, and S. Sanchez, "Controller adaptation for varying conditions and ancillary services (D3.2)," in *TotalControl - Adv. integr. supervisory and wind turbine control for optimal operation of large Wind Power Plants*, 2019. [Online]. Available: https://www.totalcontrolproject.eu/dissemination-activities/public-deliverables
[24] S. Wang, J. Hu, X. Yuan, and L. Sun, "On inertial dynamics of virtual-synchronous-controlled DFIG-based wind turbines," *IEEE Trans. Energy Convers.*, vol. 30, no. 4, pp. 1691–1702, Dec. 2015, doi: 10.1109/tec.2015.2460262.
[25] S. Wang, J. Hu, and X. Yuan, "Virtual synchronous control for grid-connected DFIG-based wind turbines," *IEEE Trans. Emerg. Sel. Topics Power Electron.*, vol. 3, no. 4, pp. 932–944, Dec. 2015.
[26] Y. Jiao, H. Nian, and G. He, "Control strategy based on virtual synchronous generator of DFIG-based wind turbine under unbalanced grid voltage," in *Proc. 20th Int. Conf. Electr. Machines Syst.*, 2017, pp. 1–6, doi: 10.1109/icems.2017.8056475.
[27] S. Shah and V. Gevorgian, "Control, operation, and stability characteristics of grid-forming type 3 wind turbines," in *Proc. 19th Wind Integr. Workshop*, 2020. [Online]. Available: https://www.nrel.gov/docs/fy21osti/78158.pdf
[28] A. Thommessen and C. M. Hackl, "Combining virtual synchronous machine and feedforward torque control for doubly-fed induction machine based wind energy conversion systems," in *Proc. IEEE 32nd Int. Symp. Ind. Electron.*, 2023, pp. 1–8, doi: 10.1109/isie51358.2023.10228015.
[29] N. Klaes, F. Pöschke, and H. Schulte, "Grid forming stator flux control of doubly-fed induction generator," *Energies*, vol. 14, no. 20, Oct. 2021, Art. no.. 6766, doi: 10.3390/en14206766.
[30] ENTSO-E SPD - Inertia TF, "Inertia and rate of change of frequency," 2020. [Online]. Available: https://eepublicdownloads.azureedge.net/clean-documents/SOCdocuments/InertiaandRoCoF_v17_clean.pdf
[31] J. Jonkman, S. Butterfield, W. Musial, and G. Scott, "Definition of a 5-MW reference wind turbine for offshore system development," Feb. 2009. [Online]. Available: https://www.nrel.gov/docs/fy09osti/38060.pdf
[32] D. Duckwitz, "Power system inertia – derivation of requirements and comparison of inertia emulation methods for converter-based power plants," Ph.D. dissertation, Universität Kassel, Kassel, Germany, 2019, doi: 10.17170/kobra-20190510451.
[33] W. B. W. Bao, L. D. L. Ding, S. Y. S. Yin, K. W. K. Wang, and V. Terzija, "Active rotor speed protection for DFIG synthetic inertia control," in *Proc. Mediterranean Conf. Power Gener. Transmiss. Distrib. Energy Convers.*, 2016, pp. 1–5, doi: 10.1049/cp.2016.1074.
[34] D. Schröder and J. Böcker, Eds., *Elektrische Antriebe Regelung Von Antriebssystemen.*, Berlin, Germany: Springer, 2020.
[35] S.-W. Su, H. Börngen, C. M. Hackl, and R. Kennel, "Nonlinear current control of reluctance synchronous machines with analytical flux linkage prototype functions," *IEEE Open J. Ind. Electon. Soc.*, vol. 3, pp. 582–593, 2022, doi: 10.1109/OJIES.2022.3208329.
[36] VDE, "VDE-AR-N 4110 application guide: Technical requirements for the connection and operation of customer installations to the medium voltage network (TAR medium voltage)," 2018. [Online]. Available: https://www.vde.com/en/fnn/topics/technical-connection-rules/tcr-for-medium-voltage
[37] J. Machowski, Z. Lubosny, J. W. Bialek, and J. R. Bumby, *Power System Dynamics: Stability and Control.*, Hoboken, NJ, USA: Wiley, 2020.
[38] A. Tayyebi, D. Groß, and A. Anta, "GridFormingConverters: Implementation of grid-forming control techniques in IEEE 9-bus system," *Git repository*, 2019. [Online]. Available: https://github.com/ATayebi/GridFormingConverters
[39] ENTSO-E RG-CE System Protection & Dynamics Sub Group, "Frequency measurement requirements and usage," 2016. [Online]. Available: https://docstore.entsoe.eu/Documents/SOCdocuments/Regional_Groups_Continental_Europe/2018/TF_Freq_Meas_v7.pdf

ANDRE THOMMESSEN (Member, IEEE) was born in Düren, Germany, in 1995. He received the B.Eng. degree in electrical engineering from the FH Aachen University of Applied Sciences, Campus Jülich, Germany, in 2017, and the M.Sc. degree in electrical engineering in 2019 from the Technical University of Munich (TUM), Munich, Germany, where he is currently working toward the Ph.D. degree in electrical engineering.

Since 2020, he has been a Research Assistant with the "Laboratory for Mechatronic and Renewable Energy Systems," Hochschule München University of Applied Sciences, Munich, Germany. His research interests include control of electrical drives and renewable energy conversion systems.

CHRISTOPH MICHAEL HACKL (Senior Member, IEEE) was born in Mannheim, Germany, in 1997. He studied electrical engineering (with focus on mechatronics and systems and control) from the Technical University of Munich (TUM), Munich, Germany and University of Wisconsin-Madison, Wisconsin, USA, and received the B.Sc., Dipl.-Ing., and Dr.-Ing. (Ph.D.) degrees in electrical engineering and the Habilitation in "mechatronics and renewal energy systems" from TUM, in 2003, 2004, 2012, and 2019, respectively.

Since 2004, he has been teaching electrical drives, power electronics, and mechatronic and renewable energy systems. Since 2014, he has been the head of the research group "Control of Renewable Energy Systems" with TUM. In 2018, he became a Professor of electrical machines and drives and the head of the "Laboratory for Mechatronic and Renewable Energy Systems" with the Hochschule München (HM) University of Applied Sciences, Munich. He co-founded the research Institute for Sustainable Energy Systems with HM, which he co-heads since then. His research interests include nonlinear, adaptive and optimal control and design of electrical drives, and mechatronic and renewable energy systems.